AGU ADVANCING EARTH AND SPACE SCIENCES

JGR Planets

RESEARCH ARTICLE

10.1029/2026JE009724

Reconstructing Europa's Atmosphere From H_2^+ Pickup Ions Detected During the Juno PJ45 Flyby

Shane R. Carberry Mogan[1], Andrew R. Poppe[2], Lucas Liuzzo[2], Jamey R. Szalay[3], Sean P. Ellis[3], Robert E. Johnson[4,5], and Lorenz Roth[1]

[1]KTH Royal Institute of Technology, Stockholm, Sweden, [2]Space Sciences Laboratory, University of California, Berkeley, Berkeley, CA, USA, [3]Princeton University, Princeton, NJ, USA, [4]University of Virginia, Charlottesville, VA, USA, [5]New York University, New York, NY, USA

Key Points:

- H_2^+ pickup ions measured during the *Juno* flyby of Europa are reproduced to within 5% across both the inbound and outbound legs
- Agreement with the *Juno* flyby data requires a background H_2^+ component consistent with Europa's local H_2^+ torus
- Re-analysis of this data set demonstrates that Europa's H_2 atmosphere is predominantly thermal, rather than nonthermal as initially inferred

Correspondence to:

S. R. Carberry Mogan,
shanecm@kth.se

Citation:

Carberry Mogan, S. R., Poppe, A. R., Liuzzo, L., Szalay, J. R., Ellis, S. P., Johnson, R. E., & Roth, L. (2026). Reconstructing Europa's atmosphere from H_2^+ pickup ions detected during the Juno PJ45 flyby. *Journal of Geophysical Research: Planets*, *131*, e2026JE009724. https://doi.org/10.1029/2026JE009724

Received 13 FEB 2026
Accepted 2 JUL 2026

Abstract We use a suite of single-species (H_2) and multispecies ($H_2 + O_2 + H + O$) Direct Simulation Monte Carlo models of Europa's atmosphere to interpret the H_2^+ pickup ions detected by *Juno* at distances beyond 2 Europa radii (R_E) during the Perijove 45 flyby. The observations require contributions from both Europa's H_2 atmosphere and a background H_2^+ torus; the latter has local densities ranging from ~ 1.1 cm^{-3} on the inbound leg (anti-Jovian hemisphere) to ~ 0.9 cm^{-3} on the outbound leg (sub-Jovian hemisphere)—an asymmetry in the H_2^+ torus consistent with recent plasma-advection modeling. We show that the magnitude and spatial structure of the observed H_2^+ signatures are reproduced to within ±5% over $\sim 4R_E$ along both legs of the flyby by a purely thermal H_2 atmosphere embedded within the H_2^+ torus. Best-fit H_2 source rates of $\sim(3–4) \times 10^{26}$ s^{-1} yield surface densities of $\sim(6–8) \times 10^5$ cm^{-3}, radial column densities of $\sim(2–3) \times 10^{13}$ cm^{-2}, and line-of-sight column densities at the limb of $\sim 10^{14}$ cm^{-2}. Assuming a 2:1 stoichiometric ratio, the implied O_2 source rates produce O_2 column densities of $\sim 10^{14}$ cm^{-2}, slightly less than inferred from remote-sensing observations. Contrary to initial interpretations, a nonthermal H_2 component is not required to reproduce the data. Even when one is included, the atmosphere becomes predominantly thermal through recycling of non-condensing H_2 at the surface—an effect amplified when collisions with the denser O_2 population redirect otherwise escaping molecules back to the ice, where they thermalize. Atmospheric escape from Europa supplies Jupiter's magnetosphere with neutral hydrogen and oxygen at roughly equal mass loss rates of ~ 1 kg s^{-1}.

Plain Language Summary During *Juno*'s close flyby of Europa on 29 September 2022, the spacecraft detected H_2^+ "pickup ions," which form when neutral hydrogen molecules (H_2) in Europa's atmosphere and its surrounding torus become ionized and then swept up by Jupiter's rapidly rotating magnetosphere. Using detailed numerical simulations of Europa's atmosphere, we track H_2, molecular oxygen (O_2), and their dissociation products (H and O) as they move, collide, escape to space, return to the surface, or become ionized. When H_2 becomes ionized, the newly created H_2^+ ions are tracked along their paths as they are carried by Jupiter's circulating plasma toward *Juno*, allowing direct comparison between simulated and measured ion densities. Our results show that Europa's H_2 atmosphere is dominated by particles whose energies are set by repeated interactions with the icy surface. We also find that Europa is surrounded by a cloud of H_2^+ continually supplied by H_2 that escapes the atmosphere, forms a neutral torus, and later becomes ionized. Together, ionization of the local H_2 atmosphere and this background H_2^+ torus reproduce the *Juno* measurements with remarkable accuracy across more than 12,000 km. Finally, by comparing how much hydrogen escapes or becomes ionized with how much returns to the surface, we estimate the net loss of water-equivalent material to be roughly 10 kg per second.

1. Introduction

Although the Juno mission was originally designed to explore Jupiter (Bolton et al., 2017), it has enhanced our understanding of the Galilean moons. In particular, *Juno*'s Jovian Auroral Distributions Experiment (JADE; McComas et al., 2017) observed H_2^+ between $\sim$13–18 Jupiter radii originating from Europa's neutral H_2 torus (Szalay et al., 2022), confirming earlier in-situ measurements (Kollmann et al., 2016; Lagg et al., 2003; Mauk et al., 2003; Nénon & André, 2019) and complementary numerical models (Smith et al., 2019; Smyth & Marconi, 2006). More recently, during the Perijove 45 (PJ45) close flyby of Europa on 29 September 2022, *Juno*/JADE detected H_2^+ sourced by the moon's neutral atmosphere, from which properties such as H_2 and O_2 production rates were inferred (Szalay et al., 2024).

In this study, we revisit the PJ45 data set with numerical models of Europa's neutral atmosphere and the ensuing dynamics of H_2^+ ions picked up by Jupiter's co-rotating magnetosphere. First, we apply a direct simulation Monte Carlo (DSMC) model to the atmosphere, self-consistently simulating H_2 and O_2 produced via radiolysis, as well as H and O generated via magnetospheric electron-impact dissociation and dissociative ionization of their parent molecules, such that these sources and sinks, along with transport, interspecies collisions, and escape are treated simultaneously within a single framework. Next, we use a guiding-center model to track H_2^+—produced by electron-impact ionization and charge-exchange with ambient H^+, O^+, S^{++}—transported along plasma streamlines toward *Juno* to predict the resulting H_2^+ densities along the spacecraft's flyby trajectory. We then compare these simulated H_2^+ densities directly to *Juno*/JADE measurements, assessing how variations in plasma speeds and ionization rates, as well as the relative contributions of thermal versus nonthermal H_2 components, influence the interpretation. From this analysis, we refine constraints on Europa's tenuous atmosphere, such as sources and sinks and the resulting structure.

The remainder of this paper is organized as follows. Section 2 summarizes the current understanding of Europa's atmosphere and the observational and modeling context relevant to this study. Section 3 describes the *Juno*/JADE PJ45 data set and the modeling framework, including DSMC simulations of Europa's atmosphere and a guiding-center model that converts H_2^+ production to densities along the flyby trajectory. Section 4 presents constraints on Europa's atmosphere, assesses the roles of thermal versus nonthermal H_2 components and the influence of interspecies collisions, and examines the implications for atmospheric escape—such as the contributions to Jupiter's magnetosphere and associated surface erosion—while also identifying directions for future work. Finally, Section 5 concludes the study.

2. Background

Bombardment of Europa's icy surface by Jupiter's rapidly rotating magnetospheric plasma drives processes that produce and deplete a tenuous, primarily water-product atmosphere (Johnson et al., 2009). Impinging ions and electrons strike Europa's surface ice, breaking molecular bonds and ejecting intact and fragmented H_2O into the atmosphere—a process known as sputtering (Johnson, 1990). Plasma particles penetrating deeper into the ice induce radiolysis, dissociating and ionizing H_2O and other surface constituents to produce reactive radicals, ions, and electrons that can recombine into new—and in some cases volatile—molecular species, which may diffuse through the porous icy regolith and release into the atmosphere via thermal desorption or subsequent sputtering (Johnson & Quickenden, 1997).

At Europa's surface temperatures, radiolytically produced molecular oxygen (O_2) and hydrogen (H_2) are volatile and therefore accumulate in the atmosphere as follows. After being released into the atmosphere, both species may escape or undergo reactions predominantly driven by the ambient plasma and, to a lesser extent, solar ultraviolet (UV) photons, but most eventually fall back to the surface. Upon return, however, they do not adsorb efficiently (e.g., Acharyya, 2014; Johnson, 1990; Sandford & Allamandola, 1993) and instead permeate the porous, ice-rich regolith (e.g., Johnson et al., 2019), where they remain largely inert, although “condensed” O_2 bands have been observed (Spencer & Calvin, 2002). Through successive collisions with grains in the porous ice, O_2 and H_2 molecules thermalize to the local surface temperature and subsequently desorb back into the atmosphere, where this cycle repeats. Thus, the atmosphere that develops is predominantly thermal and maintained by a balance between this continual recycling and losses from escape and reactions, with any nonthermal populations discernible only at extended altitudes, if at all.

While aloft in the atmosphere, neutral particles can interact with the Jovian magnetospheric plasma and solar UV radiation, leading to dissociation and/or ionization. Ionized neutrals—whether by charge exchange, electron impacts, or solar UV photons—can contribute to Europa's ionosphere or be picked up and accelerated by the corotating Jovian magnetic field. Magnetospheric electrons and solar UV photons can also dissociate atmospheric molecules—either via non-ionizing dissociation or dissociative ionization—producing nonthermal fragments whose initial speeds often exceed that required to remain gravitationally bound to Europa. These dissociation products can therefore escape, supplying the Jovian magnetosphere with neutrals, or, if directed downward, re-impact the icy surface. While traversing the atmosphere, they may also collide with other neutrals, redistributing energy and contributing to additional escape pathways (e.g., Carberry Mogan et al., 2024).

This understanding of Europa's atmosphere is built on more than four decades of laboratory experiments and numerical modeling (e.g., Carberry Mogan et al., 2024; Johnson, 1990; Smyth & Marconi, 2006; Teolis et al., 2017), and is supported by a range of observational constraints. However, the initial interpretation of *Juno*'s close flyby of Europa on 29 September 2022 suggested a markedly different atmospheric structure, challenging the predominantly thermal framework established by prior studies. During this encounter, *Juno*/JADE provided direct in-situ measurements of pickup ions (PUIs) from Europa, offering a unique window into its neutral atmosphere and forming the core data set analyzed in this study. Mass-resolved measurements during PJ45 clearly identified H_2^+ originating from H_2 in Europa's atmosphere (Szalay et al., 2024), complementing *Juno*/JADE observations of H_2^+ associated with the moon's co-rotating neutral H_2 torus (Szalay et al., 2022).

To analyze the PJ45 data set, Szalay et al. (2024) applied a PUI advection model in which local H_2^+ production—calculated from the ionization of atmospheric H_2—was propagated along guiding-center streamlines and then integrated downstream toward the spacecraft, yielding simulated H_2^+ densities for direct comparison with those measured by JADE. Two prior numerical models of Europa's atmosphere—Smyth and Marconi (2006), "S&M06," and Vorburger and Wurz (2018), "V&W18"—provided H_2 density profiles for the PUI advection model. S&M06 employed a 2D DSMC model—including interspecies collisions—that assumed the H_2 component thermally desorbed from the surface, but subsequently collided with ambient plasma and dissociation products, generating a pronounced nonthermal tail in its velocity distribution (e.g., Figure 3 therein). In contrast, V&W18 implemented a 1D collisionless Monte Carlo model, prescribing a nonthermal sputtering source for H_2 at the surface. Despite these differences, both models converge on a common endpoint: H_2 molecules returning to the surface fully thermalize with the ice and re-emit thermally into the atmosphere. Consequently, although each simulation included a nonthermal H_2 component—sourced by different mechanisms—the thermal population remained predominant. However, Szalay et al. (2024) showed that neither model could reproduce the H_2^+ densities measured by JADE without significant rescaling of their neutral H_2 density profiles: S&M06 by 0.15× and V&W18 by 8.1 ×. Even after these ad-hoc adjustments, both models still did not capture the inferred slope of the H_2^+ density profile (see Figure 3 in Szalay et al., 2024).

To provide a sufficient fit to the JADE data, Szalay et al. (2024) instead adopted the following formula for the H_2 density profile, from which H_2^+ production rates were derived:

$$n(r) = n_0\left(\frac{r}{r_0}\right)^{-2}\exp\left(\frac{-(r-r_0)}{D}\right), \tag{1}$$

where $n(r)$ is the number density at radial distance r, n_0 is the number density at a prescribed lower boundary r_0, and D is the depletion length scale—defined as a species' radial outflow speed u divided by its total loss rate κ. Equation 1 is a rearrangement of the continuity equation; Summers et al. (1989) showed that when D exceeds a species' atmospheric scale height H, the number density falloff is governed by escape, whereas for $D \lesssim H$ losses by reactions dominate the radial decay of the density. Using Equation 1, Szalay et al. (2024) found that an H_2 density profile with $n_0 = (1.8 \pm 0.05) \times 10^5\ \mathrm{cm}^{-3}$ and $D = 6090 \pm 890$ km provided the best fit to the JADE data. When H_2 thermally equilibrates to Europa's surface temperatures, $T_0 \sim 80$–140K, the corresponding atmospheric scale heights are $H = \frac{kT_0 r_0^2}{GM_E m_{H_2}} \sim 250$–440km, where k and G are the Boltzmann and gravitational constants; $r_0 = R_E = 1560.8$ km and $M_E = 4.8 \times 10^{22}$ kg are Europa's radius and mass; and $m_{H_2} = 2.02$ AMU is the mass of an H_2 molecule. Because the best-fit D far exceeds this range of thermal scale heights, Szalay et al. (2024) concluded that Europa's atmosphere must contain a substantial nonthermal H_2 component with an effective scale height comparable to D to sustain the inferred density profile. Moreover, by combining the loss rate $\kappa = (4.3$–$13) \times 10^6\ \mathrm{s}^{-1}$ derived from electron fluxes also measured by JADE with the fitted D, they estimated $u = 58 \pm 34$ m/s. From this radial outflow speed, Szalay et al. (2024) then derived the H_2 source rate, $\Phi_0 = 4\pi r_0^2 n_0 u \sim (4.5 \pm 3.3) \times 10^{26}\ \mathrm{s}^{-1}$ ($\sim 1.5 \pm 1.1$ kg/s), which—assuming a 2:1 stoichiometry of H_2 to O_2 radiolytic production—yielded an O_2 source rate of $\Phi_0 \sim (2.2 \pm 1.6) \times 10^{26}\ \mathrm{s}^{-1}$ ($\sim 12 \pm 8.8$ kg/s).

While Szalay et al. (2024) extracted a wealth of information about Europa's neutral atmosphere from these PUI measurements, their interpretation of the JADE data hinges on key assumptions in the formula adapted from Summers et al. (1989), which we reassess here. In particular, solving for D requires treating u as a constant. This is not strictly valid because the mean radial outflow speed—the net balance of upward versus downward

Table 1
Average Magnetospheric Electron-Impact Reaction Rates for H_2 and O_2 Derived From JADE-E Electron Flux Measurements During the Europa PJ45 Flyby

		Rate[a] [($\times 10^{-6}$) s^{-1}]		
Reactants	Products	Inbound	Outbound	Branching ratio (%)
$H_2 + e^-$	$H_2^+ + 2e^-$	1.70	1.75	65
	$H + H + e^-$	0.845	0.880	32
	$H^+ + H + 2e^-$	0.0811	0.0860	3
Total		**2.62**	**2.72**	**100**
$O_2 + e^-$	$O_2^+ + 2e^-$	2.91	3.05	60
	$O + O + e^-$	1.05	1.07	22
	$O^+ + O + 2e^-$	0.869	0.933	18
Total		**4.84**	**5.07**	**100**

[a]Rates are averaged separately over the inbound ($-5R_E \leq Y_{EphiO} \leq -2R_E$) and outbound ($-2R_E \leq Y_{EphiO} \leq -5R_E$) legs of the flyby (see Figure B1 in Appendix B).

motions—increases with altitude: only H_2 molecules in the high-velocity tail of the distribution have sufficient energy to populate the upper atmosphere and/or escape, skewing the local population toward higher speeds and raising $u(r)$. However, describing a radially varying u requires simultaneously solving Equation 1 and the momentum equation, effectively treating Europa's atmosphere as a fluid. Although numerical models show that collisions occur near the surface, with the exobase lying above this boundary (e.g., Shematovich & Johnson, 2001; Shematovich et al., 2005; Shematovich, 2006, S&M06, Carberry Mogan et al., 2024), these collisions are too infrequent for a fluid description to be valid. Instead, determining $u(r)$, and by extension $n(r)$, in a rarefied gas that transitions from collisional to collisionless requires a molecular kinetics model, such as the DSMC method (Bird, 1994). Indeed, Appendix A shows that applying Equation 1 with a constant outflow speed yields H_2 density profiles inconsistent with those obtained from DSMC simulations, underscoring the limitations of this approximation for Europa's tenuous atmosphere.

3. Methods

3.1. Jovian Auroral Distributions Experiment (JADE) Data

During the PJ45 flyby of Europa, the electron sensors onboard *Juno*/JADE (JADE-E) measured electron intensities over an energy range of approximately 0.03–30keV. Ellis et al. (2026) converted these measurements into differential intensity (directional) and omnidirectional flux distributions, where the latter are obtained by integrating the former over solid angle. These flux distributions were then used to compute electron-impact reaction rates for H_2 and O_2 by convolving them with the corresponding energy-dependent cross sections. Although instantaneous electron-impact reaction rates were derived along the *Juno* trajectory (Figure B1 in Appendix B), we adopt representative inbound- and outbound-averaged values in the DSMC and guiding-center models (Sections 3.2–3.3), as these provide a more appropriate characterization of the mean electron conditions. Table 1 summarizes the resulting averaged reaction rates for H_2 and O_2 used in this study. In Section 4.1.1 (Table 2), we quantify how variations in ionization rates affect the derived H_2 source rates and show that, for a given plasma speed, the resulting differences are limited to within a factor of ~2.

Also during the PJ45 flyby, the ion sensor onboard *Juno*/JADE (JADE-I) measured ions with mass-per-charge ratios spanning 1–50AMU/Q and energies between 0.01 and 46 keV. JADE-I employs a time-of-flight (TOF) section that enables separation of ion species by AMU/Q across its energy range, allowing the plasma composition to be resolved as a function of energy (e.g., Figure 2 of Szalay et al., 2024). Measured ion count rates are converted into differential intensities and subsequently transformed into phase-space densities by accounting for particle velocities; integration over the measured energy and pitch-angle range yields ion (e.g., H_2^+) number densities along *Juno*'s PJ45 trajectory, following established techniques (e.g., Szalay et al., 2022). Raw JADE-I measurements are smoothed using a spin-phase-aligned filter to suppress spacecraft-spin-induced fluctuations while preserving the broader pickup-ion signature associated with the flyby. Figure 1 compares the raw and reconstructed H_2^+ number densities measured along the PJ45 trajectory.

At detected energies below a few keV/Q, H^+ and H_2^+ overlap in JADE's TOF×E space—an instrumental effect that has been well documented in the literature (Kim et al., 2020; McComas et al., 2017; Szalay et al., 2022). As a result, isolating the H_2^+ signal from the total TOF×E count space becomes more challenging when H_2^+ is below a few keV and has comparable densities to H^+. We therefore restrict our analysis to $|Y_{EPhiO}| \lesssim 5R_E$ to ensure our capability to successfully quantify the total H_2^+ abundance. Figure 1 also includes insets showing JADE TOF count rates in AMU/Q by energy space for light ions with AMU/Q $\lesssim 3$. The low time-of-flight tails from heavier ions have been removed, and the H_2^+ spectra are isolated following the methodology of Szalay et al. (2022). In the examples shown at $|Y_{EPhiO}| \sim 4R_E$, H_2^+ can be clearly identified. At much larger distances, however, the H_2^+ signal becomes increasingly difficult to extract within the H^+ "fork," owing to the instrumental response associated with hydrogen charge-state changes in the carbon foil of the JADE TOF subsystem (McComas et al., 2017; Szalay et al., 2022). Nevertheless, at distances beyond $|Y_{EPhiO}| \sim 3R_E$, the H_2^+ densities do not decay to zero but instead

Table 2
Best-Fit H_2 Source Rates for Simulations of Purely Thermal, Collisionless H_2 Atmospheres as a Function of Varying Electron-Impact Ionization Rates (e.g., Table 1 and Figure B1 in Appendix B) and Magnetospheric Plasma Flow Speeds (e.g., Figure 3; Ebert et al., 2025, Table 1 Therein) for the Inbound (Top; Best-Fit H_2^+ Background Density = 1.09 cm^{-3}) and Outbound (Bottom; Best-Fit H_2^+ Background Density = 0.91 cm^{-3}) Legs of the PJ45 Flyby

Inbound					
		Electron-impact ionization rate[a]			
H_2 source rate [$(\times 10^{26})$ s^{-1}]		Minimum	Mean	Maximum	Maximum + CX
Magnetospheric plasma speed[b]	Minimum	4.70	3.22	2.24	1.61
	Mean	5.33	3.63	2.55	1.84
	Maximum	6.00	4.08	2.87	2.06

Outbound					
		Electron-impact ionization rate[a]			
H_2 source rate [$(\times 10^{26})$ s^{-1}]		Minimum	Mean	Maximum	Maximum + CX
Magnetospheric plasma speed[b]	Minimum	5.64	4.34	3.63	2.46
	Mean	6.41	4.93	4.08	2.78
	Maximum	7.17	5.51	4.57	3.14

[a]The (minimum, mean, maximum) electron-impact ionization rates are $(1.16, 1.70, 2.41) \times 10^{-6}$ s^{-1} and $(1.35, 1.75, 2.11) \times 10^{-6}$ s^{-1} for the inbound and outbound legs of the PJ45 flyby, respectively. The "Maximum + CX" value is the maximum electron-impact ionization rate + the total charge-exchange ("CX") rate calculated between H_2 and H^+, O^+, and S^{++} in Jupiter's magnetosphere: 9.9×10^{-7} s^{-1} (see Table D2 in Appendix D). [b]The (minimum, mean, maximum) magnetospheric plasma speeds are (84, 96, 108) km/s and (88, 100, 112) km/s for the inbound and outbound legs of the PJ45 flyby, respectively. For reference, the rigid corotation speed of the Jovian magnetosphere at Europa's orbit is 104 km/s.

asymptote to a finite value of ~ 1 cm^{-3} (Figure 1), indicating the presence of an extended background component; this feature is revisited in Section 4.

3.2. Atmosphere Model

We model Europa's tenuous atmosphere using the DSMC method (Bird, 1994), in which macroscopic atmospheric dynamics emerge from probabilistic simulations of microscopic particle ensembles. In this work, we use

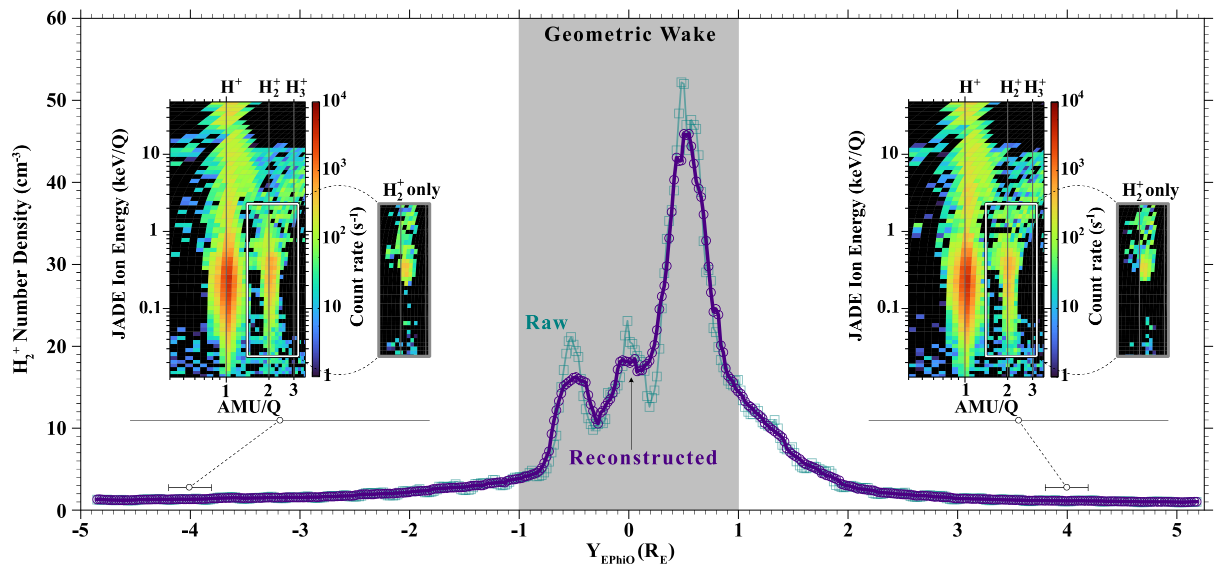

Figure 1. H_2^+ number densities measured by *Juno*/JADE-I during the PJ45 flyby of Europa. The teal line and squares show the raw measurements, while the indigo line and circles show the reconstructed, spin-phase–smoothed values. Insets show JADE time-of-flight (TOF) count rates in AMU/Q by energy space for the light ions with AMU/Q $\lesssim 3$.

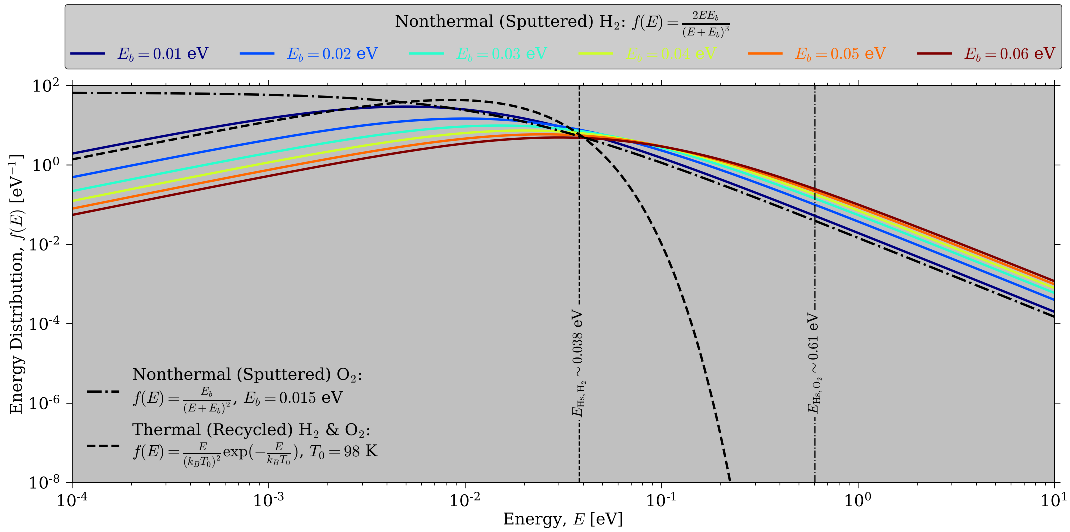

Figure 2. Energy distributions $f(E)$ for nonthermal (sputtered) H_2 (colored lines) and O_2 (dash-dotted black line)—each parameterized by its prescribed fit parameters (Equation 3) and effective binding energy E_b—plotted alongside the Maxwellian-flux distribution for the thermal (recycled) H_2 and O_2 components (dashed black line, Equation 2). Vertical black lines mark the energies required to reach Europa's Hill sphere, E_{Hs}: $\sim$0.038 eV for H_2 (dashed) and $\sim$0.61 eV for O_2 (dash-dotted).

Harrah, a molecular-kinetics model originally developed for the icy Galilean satellites' atmospheres (Carberry Mogan et al., 2020, 2022, 2024, 2025; Carberry Mogan, Tucker, & Johnson, 2021; Carberry Mogan, Tucker, Johnson, Vorburger, et al., 2021) and recently extended to study multispecies exoplanetary atmospheric escape (Evans et al., 2025) and gravity waves at Mars (Chavez et al., 2026). *Harrah* is configured to simulate thermal and nonthermal sources, transport, and losses of radiolytically produced H_2 and O_2, as well as the H and O generated by magnetospheric electron-impact dissociation and dissociative ionization of their parent molecules, while accounting for interspecies collisions.

3.2.1. Energy Distributions

As illustrated in Figure 2, for H_2 particles initially released from Europa's icy surface, we consider two energy distributions, $f(E)$, representing thermal and nonthermal sources. The thermal source—desorption—is described with a Maxwellian-flux distribution:

$$f_{\mathrm{M}}(E) = \frac{E}{(kT_0)^2}\exp\left(-\frac{E}{kT_0}\right), \tag{2}$$

where $T_0 = 98$ K is the globally averaged surface temperature, computed by area-weighting local outputs from the thermophysical model of Spencer et al. (1989) over latitude and longitude at each orbital position and then averaging those global means over Europa's entire orbit (Figure C1 in Appendix C). Since H_2 lifetimes ($\sim 3.7 \times 10^5$ s, Table 1) and Europa's orbital period ($\sim 3.1 \times 10^5$ s) are both much longer than the characteristic H_2 atmospheric residence time ($\sim 10^4$ s; e.g., Smyth & Marconi, 2006), individual molecules will return to and thermalize at the surface many times per lifetime or orbit, justifying the use of a single global-and-orbital-averaged T_0. This assumption, however, neglects diurnal variations in surface temperature and their influence on atmospheric distributions. For example, with subsolar temperatures of $\sim$140 K at the orbital phase corresponding to the *Juno* flyby (Figure C1 in Appendix C), a sublimated H_2O component could become significant (e.g., Roth, 2021). Capturing such effects require a multidimensional model (e.g., Carberry Mogan, Tucker, Johnson, et al., 2021; Carberry Mogan et al., 2022), which is beyond the scope of this study. Nevertheless, neglecting this variability does not affect the principal outcomes, as the H_2 and H_2^+ populations are governed by global production and loss rather than local conditions.

The nonthermal source—sputtering—is described with the Sigmund–Thompson formula:

$$f_{\mathrm{ST}}(E) = \frac{c_i E^{q_i} E_{b,i}}{(E + E_{b,i})^{2+q_i}}. \tag{3}$$

where c_i and q_i are fit parameters and $E_{b,i}$ is an effective binding energy for species i. Equation 3 has often been applied in models of Europa's atmosphere to describe sputtered H_2O and radiolytically produced O_2, typically using $(c, q, E_b)_{\mathrm{H_2O}} = (2, 1, 0.055\ \mathrm{eV})$ and $(c, q, E_b)_{\mathrm{O_2}} = (1, 0, 0.015\ \mathrm{eV})$ (e.g., Johnson et al., 2009 and references therein). In this study, we adopt the latter values for O_2 particles initially released from the surface (Figure 2). We do not, however, include sputtered H_2O as an atmospheric constituent, as it does not affect the principal conclusions of this study. Any contribution of H_2O (whether sputtered or sublimated) to the H_2 or H_2^+ populations is negligible compared to the H_2 produced by radiolysis and the H_2^+ generated via electron-impact ionization of that radiolytic product (e.g., Ellis et al., 2026). For the nonthermal H_2 component, analogous to H_2O, we set $c_{\mathrm{H_2}} = 2$ and $q_{\mathrm{H_2}} = 1$ in Equation 3, but treat $E_{b,\mathrm{H_2}}$ as a free parameter varying from 0.01−0.06 eV in increments of 0.01 eV across six simulations to span the values used for O_2 and H_2O.

The parameters for H_2O and O_2 derive from laboratory experiments in which time-of-flight techniques measured energy spectra of D_2O (an analog for H_2O) and O_2 molecules ejected from a D_2O ice target by incident ions (Johnson et al., 1983). An immediate D_2O signal was detected upon beam onset—indicative of direct sputtering—whereas the O_2 signal rose more gradually to a steady state, implying radiolytic production at depth followed by diffusion to the surface and ejection by subsequent ion impacts (Boring et al., 1983; Reimann et al., 1984). Although the energy spectrum D_2 (the analog of H_2) was not recorded, its signal exhibited the same immediate spike as D_2O followed by a gradual rise to steady state characteristic of O_2. This dual-mode behavior indicates that D_2 (and by analogy H_2) can be liberated from ice nonthermally—for example, when an H_2O molecule is simultaneously sputtered and dissociated into H_2 and O—and also by a slower, thermal mechanism. Whereas the nonthermal source has a pronounced nonthermal tail (e.g., Equation 3), radiolytically produced H_2 diffuses to the surface and—due to its low mass and high volatility—readily thermally desorbs, although subsequent ion impacts can still sputter H_2.

Given the ambiguity in laboratory results, there is no consensus on how to treat H_2 particles released from Europa's surface: some models assume a purely thermal source by using Equation 2 (e.g., Smyth & Marconi, 2006), while others include a nonthermal source by solving Equation 3 (e.g., Oza et al., 2019) or some iteration of the Sigmund-Thompson formula (e.g., Vorburger & Wurz, 2018). As discussed in Section 2, the original PJ45 flyby analysis by Szalay et al. (2024) suggested that a nonthermal H_2 component was necessary to reproduce the JADE measurements. Here, we test this hypothesis by simulating thermal versus nonthermal H_2 sources in Europa's atmosphere. In both cases, we assume any H_2 (and O_2) particles that return to the surface without escaping from or reacting in the atmosphere thermalize to T_0 and immediately re-emit according to Equation 2 (Figure 2). Thus, even our "nonthermal" simulations include a recycled thermal component, with the relative contributions of thermal and nonthermal H_2 to the total abundances modulated by the prescribed $E_{b,\mathrm{H_2}}$.

3.2.2. Numerical Setup and Parameters

We employ a 1D, spherically symmetric simulation domain extending from Europa's surface ($r_0 = R_E$) to its Hill sphere $r_{\mathrm{Hs}} = \left(\frac{M_E}{3M_J}\right)^{1/3} d_{\mathrm{JE}} \sim 8.7 R_E$ ($\sim 1.2 \times 10^4$ km above r_0). Here, $M_J = 1.898 \times 10^{27}$ kg and $R_J = 71,492$ km are Jupiter's mass and radius, respectively, and $d_{\mathrm{JE}} \sim 26.3 R_J$ is the orbital distance between Europa and its host planet. A radial grid partitions this region into concentric cells, within which particles are binned to compute local macroscopic properties (e.g., number density) and to facilitate collisions; see Carberry Mogan et al. (2020, 2022, 2024, 2025), Carberry Mogan, Tucker, and Johnson (2021), and Carberry Mogan, Tucker, Johnson, Vorburger, et al. (2021) for more details.

We note that this 1D formulation neglects spatial variability in surface temperature and the resulting transport (Carberry Mogan, Tucker, Johnson, Vorburger, et al., 2021; Carberry Mogan et al., 2022). For example, Carberry Mogan, Tucker, Johnson, Vorburger, et al. (2021) explicitly demonstrated that such effects introduce regional variability: 2D models produce cooler and warmer subsolar and anti-solar regions, respectively, than 1D spherically symmetric models due to day-to-night transport (Figure 4 therein). Moreover, day–night asymmetries are expected to arise from preferential nightside accumulation of non-condensable species (e.g., Hodges & Johnson, 1968). However, the use of a global-and-orbital-averaged T_0 effectively captures the resulting large-scale structure, such that these regional variations are reduced in the context of a global description.

At the lower boundary, H_2 and O_2 particles are injected with energies sampled from either the thermal Maxwellian-flux distribution (H_2; Equation 2) or the nonthermal Sigmund–Thompson formula (H_2, O_2; Equation 3), with velocity vectors drawn from the corresponding angular distributions such that the radial velocity component reflects the ejection angle relative to the surface normal. Once aloft, they follow Keplerian orbits under Europa's gravity—integrated via a fourth-order Runge-Kutta scheme—until one of three events occurs: (a) a binary elastic collision alters their velocity, (b) they undergo an electron-impact reaction, or (c) they cross a radial boundary. H_2 or O_2 undergoing ionization are removed from the simulation, while dissociation or dissociative ionization spawn one to two H and O in their place. All particles that reach r_{Hs} escape and are removed. Whereas H_2 and O_2 returning to r_0 thermalize to T_0 and are immediately re-injected via the Maxwellian-flux distribution (Equation 2), H and O are assumed to stick or react on the ice and are removed.

First, we perform collisionless simulations of Europa's H_2 atmosphere using a prescribed source rate of $\Phi_0 = 1.5$ kg/s (4.48×10^{26} H_2/s) from Szalay et al. (2024). Each run employs either a purely thermal H_2 component (desorbed and recycled) or a combination of nonthermal (sputtered) and recycled thermal sources. As detailed in Section 3.3, each neutral H_2 density profile is used to calculate H_2^+ densities along *Juno*'s PJ45 trajectory, which are directly compared to the JADE measurements. These initial comparisons yield two fitting parameters: (a) a scaling factor to adjust Φ_0 up or down, and (b) an H_2^+ background density. The H_2^+ background density is treated as a free parameter and independently constrained for the inbound and outbound segments of the trajectory. Within each segment, it is assumed to be constant, as variations are expected to occur on spatial scales much larger than those sampled during the flyby (e.g., Szalay et al., 2022). In these collisionless simulations, the slope of the total H_2 density profile is fixed by the chosen energy distribution(s) and surface temperature and the resulting loss processes (escape and reactions), while only its amplitude scales with Φ_0—a behavior that can break down once collisions are introduced—allowing us to adjust this value together with an optimal H_2^+ background density in post-processing to match the observed H_2^+ signature. In this way, allowing H_2 source rates to vary between the inbound and outbound legs provides an effective means of capturing local variability in the atmospheric structure within the otherwise spherically symmetric framework.

With these best-fit Φ_0, we then conduct multispecies (H_2+O_2+H+O) DSMC simulations to derive density profiles and escape rates for all species and to assess to what extent interspecies collisions reshape the H_2—and thus the H_2^+—distributions, necessitating revised H_2 source rates and H_2^+ background densities. In these runs, H_2 is injected at r_0 according to the best-fit Φ_0, O_2 at a 1:2 stoichiometric ratio relative to this value, and H and O are generated probabilistically according to the electron-impact dissociation and dissociative-ionization rates of their parent molecules (Table 1).

3.3. Guiding-Center Model

To compute the model-predicted H_2^+ densities along *Juno*'s flyby trajectory for comparison to the JADE measurements, it is necessary to define the drift paths of the newly born ions as they are picked up into the Jovian magnetospheric flow. In their study, Szalay et al. (2024) employed a model that returns PUI streamlines as a function of three variables (see Extended Figure 6 in Szalay et al., 2024): assumed values for the (a) unperturbed speed of the Jovian magnetospheric plasma past Europa v_0, (b) scale height of Europa's ionosphere H_I, and (c) interaction strength $\overline{\alpha}$. Here, we adopt an alternative and simpler approach that focuses on the more distant portions of the *Juno* flyby ($2R_E \lesssim |Y_{\mathrm{EPhiO}}| \lesssim 5R_E$), where the dynamics of PUIs are expected to be less affected by Europa's local plasma interaction with the Jovian magnetosphere. At these extended altitudes, the effects associated with the moon–magnetosphere interaction—such as the plasma pileup at the ram apex and field-line draping around the flanks (e.g., Addison et al., 2022, 2024; Cervantes et al., 2025; Rubin et al., 2015)—are reduced compared to regions closer to Europa. Thus, we neglect any field-line curvature or $\nabla\mathbf{B}$ drifts associated with Europa's local interaction. We also neglect curvature or $\nabla\mathbf{B}$ drifts associated with the background Jovian magnetosphere, as the spatial region over which H_2^+ production is accumulated is small compared to the characteristic magnetospheric length scales. Under these assumptions, the dominant transport mechanism for newly created H_2^+ is the $\mathbf{E} \times \mathbf{B}$ convective drift.

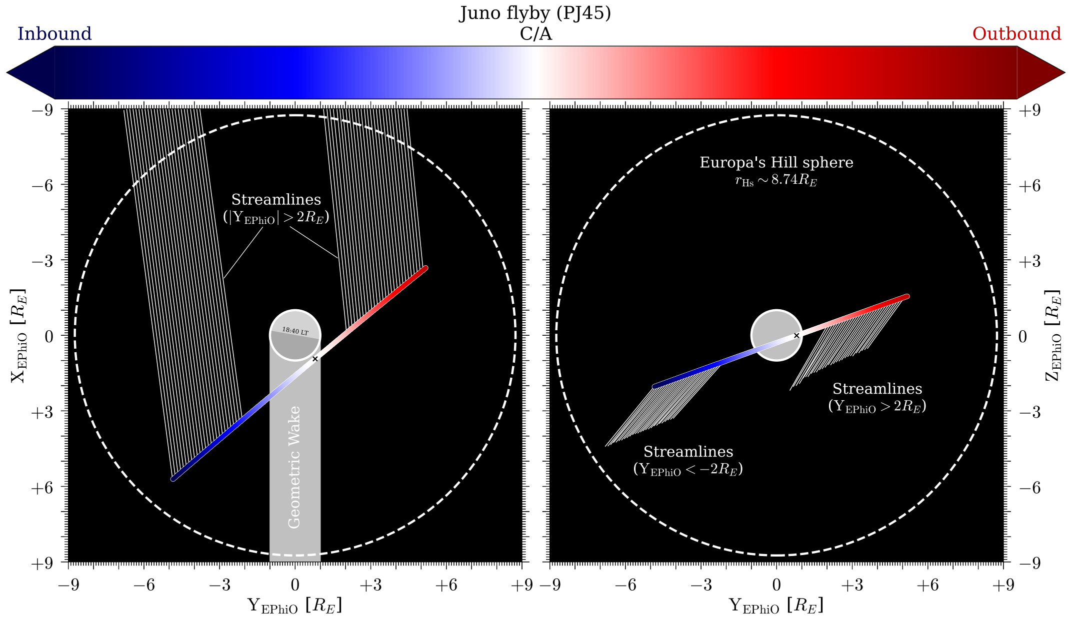

Figure 3. Plasma streamlines in $(X, Y, Z)_{\text{EPhiO}}$ coordinates (units of Europa radii, $R_E = 1{,}560.8$ km) computed for *Juno*'s PJ45 flyby (colorbar).

At each point along the *Juno* trajectory beyond $|Y_{\text{EPhiO}}| \sim 2R_E$, we use guiding-center equations of motion to trace H_2^+ ions forward in time from their source regions toward the spacecraft. The rapid cyclotron motion of each H_2^+ ion is averaged out, and only the drift of the guiding center is followed, rather than resolving individual gyrations (e.g., Beth, Galand, Jia, & Leblanc, 2025; Beth, Galand, Modolo, et al., 2025), consistent with the small H_2^+ gyroradii (~5 km; Szalay et al., 2024, Extended Table 1 therein) relative to the spatial scales considered here. To compute this drift and the associated H_2^+ PUI streamlines, we construct the convection electric field for the inbound and outbound legs of the PJ45 flyby using the local magnetic field vectors measured by *Juno*'s magnetometer (Connerney et al., 2017) together with the local plasma velocities reported by Ebert et al. (2025) (Table 1 therein). The plasma velocity is taken to be the measured proton bulk velocity, which we adopt as representative of the ambient magnetospheric flow. Newly created H_2^+ ions are therefore assumed to convect with the same average guiding-center speed as the protons, denoted here as v. The proton speeds are provided separately for the inbound and outbound legs of the Europa flyby—96 ± 12 km/s and 100 ± 12 km/s, respectively—and for each segment we consider three cases spanning the minimum, mean, and maximum values. Figure 3 shows the resulting guiding-center streamlines computed using mean magnetic-field and plasma-velocity measurements.

Along each streamline s_i, the local H_2^+ production rate $P_{H_2^+} = n_{H_2}\kappa_{\text{ion}}$ is computed, where n_{H_2} is the DSMC-derived neutral H_2 density and κ_{ion} is the prescribed ionization rate (Table 1). As was done by Szalay et al. (2024), the nascent H_2^+ ions are then advected along s_i by summing over discrete segments $\Delta s_j \sim 0.03R_E$:

$$n_{H_2^+}(s_i) = v^{-1}\sum_j P_{H_2^+}(\mathbf{r_j})\Delta s_j, \tag{4}$$

where $n_{H_2^+}$ is the cumulative H_2^+ density at the endpoint of s_i (i.e., *Juno*'s location along the PJ45 trajectory); and $\mathbf{r_j}$ is a discrete point in $(X, Y, Z)_{\text{EPhiO}}$ along s_i. The resulting H_2^+ density profile is then directly compared to the in-situ JADE measurements over the interval $2R_E \lesssim |Y_{\text{EPhiO}}| \lesssim 5R_E$, where the H_2^+ signal can be robustly extracted (Figure 1).

In this formulation, the streamlines s_i are approximated as straight flow vectors, neglecting any deflection associated with Europa's interaction with the Jovian magnetosphere. While plasma flow deflection can persist out to $\sim 2R_E$ (e.g., Szalay et al., 2024) and is generally accompanied by spatial variations in plasma speed, its impact is reduced at the altitudes considered here. We therefore assess this approximation a posteriori (Section 4.1.1,

Appendix E, Figure E1) by performing a direct comparison with the deflected streamlines of Szalay et al. (2024) (using $v_0 = 100$ km/s, $H_I = 30$ km, and $\overline{\alpha} = 0.55$), in which the local plasma speed $v(\mathbf{r}_j)$ varies along each streamline and enters Equation 4 within the summation, rather than as a constant prefactor. We find that this does not significantly affect the inferred H_2^+ background densities or H_2 source rates. Although the deflected-streamline model provides a more detailed description of the plasma interaction, it introduces additional free parameters ($\overline{\alpha}$, H_I, and v_0) that are not uniquely constrained for the PJ45 flyby (e.g., Szalay et al., 2024, Extended Data Figure 6 therein). To minimize degeneracy and isolate the dependence on the neutral atmosphere, we therefore adopt the simplified straight-flow-vector approximation throughout this study.

4. Results and Discussion

Section 4.1 presents 1D simulations of collisionless, purely thermal (Section 4.1.1) and nonthermal + thermal (Section 4.1.2) H_2 atmospheres to determine the best-fit H_2 source rates and H_2^+ background densities through direct comparison to the *Juno*/JADE measurements during PJ45. Section 4.2 then extends the analysis to include the O_2 produced via radiolysis alongside H_2, as well as their dissociation products H and O, to assess how interspecies collisions influence the structure of Europa's atmosphere and the resulting H_2^+ PUI signatures. We note that although *Juno*/JADE measurements at radial distances beyond $2R_E$ provide the direct constraints, these regions are physically coupled to the atmosphere at lower altitudes governed by the DSMC model.

4.1. Collisionless H_2 Atmosphere

Here we simulated Europa's H_2 atmosphere in 1D, assuming an initial source rate of $\Phi_0 = 4.48 \times 10^{26}$ s^{-1} (Szalay et al., 2024) and that molecules returning to the icy surface immediately thermally desorb back into the atmosphere, while using prescribed inputs for electron-impact reaction rates (Table 1), energy distributions (Equations 2 and 3 and Figure 2), and a uniform surface temperature ($T_0 = 98$ K, Figure C1 in Appendix C). The resulting H_2 density profile is then converted into H_2^+ pick up ion densities along the *Juno* flyby (Section 3.3) for direct comparison with the JADE measurements (Figure 1). For this initial source rate—regardless of whether the H_2 atmosphere is modeled as purely thermal or thermal + nonthermal—the comparison does not adequately reproduce the data unless two independent parameters are adjusted: (a) Φ_0 is scaled up or down, which linearly adjusts the amplitude of the H_2 density profile while preserving its shape; and (b) an H_2^+ background density is introduced, which is added to the densities of the H_2^+ PUIs produced by atmospheric H_2. Sections 4.1.1 and 4.1.2 present these analyses for purely thermal and thermal + nonthermal H_2 atmospheres, respectively, to determine the best-fit H_2 source rates and H_2^+ background densities.

4.1.1. Purely Thermal H_2

Figure 4 shows the resulting χ^2 distributions and 1σ confidence intervals for the H_2 source rate and H_2^+ background density derived separately for the inbound and outbound legs of PJ45. The best fits correspond to H_2 source rates of 3.63×10^{26} s^{-1} and 4.93×10^{26} s^{-1}, with H_2^+ background densities of 1.09 cm^{-3} and 0.91 cm^{-3}, respectively. The confidence intervals indicate that both parameters are well constrained by the data: $\sim(1.2\text{–}6.0) \times 10^{26}$ H_2/s and $\sim$0.75–1.45 H_2^+/cm^3 on the inbound leg, and $\sim(3.2\text{–}6.6) \times 10^{26}$ H_2/s and $\sim$0.7–1.1 H_2^+/cm^3 on the outbound leg. These narrow ranges of acceptable values overlap, demonstrating that the retrieved H_2 source rates and H_2^+ background densities are consistent within uncertainty.

Figure 5 compares the total simulated H_2^+ densities with the JADE measurements along the PJ45 trajectory. The in-situ detections are reproduced within ±5% over a distance of $\sim 4R_E$ across both the inbound and outbound legs of the flyby (corresponding to $2R_E \lesssim |Y_{\text{EPhiO}}| \lesssim 5R_E$), demonstrating excellent agreement between our model and the data. The slight differences between the inbound and outbound best-fit values reflect the combined influence of varying plasma and ionization conditions measured along the PJ45 trajectory. Electron-impact ionization rates were lower on the inbound leg (Table 1 and Figure B1 in Appendix B), whereas the plasma flow speeds were higher on the outbound leg—each effect requiring a larger H_2 source rate to reproduce the observed H_2^+ densities. Because the relative change in plasma speed between the outbound and inbound legs exceeds that of the ionization rate, the net effect is a slightly larger best-fit H_2 source rate for the outbound case. Meanwhile, since

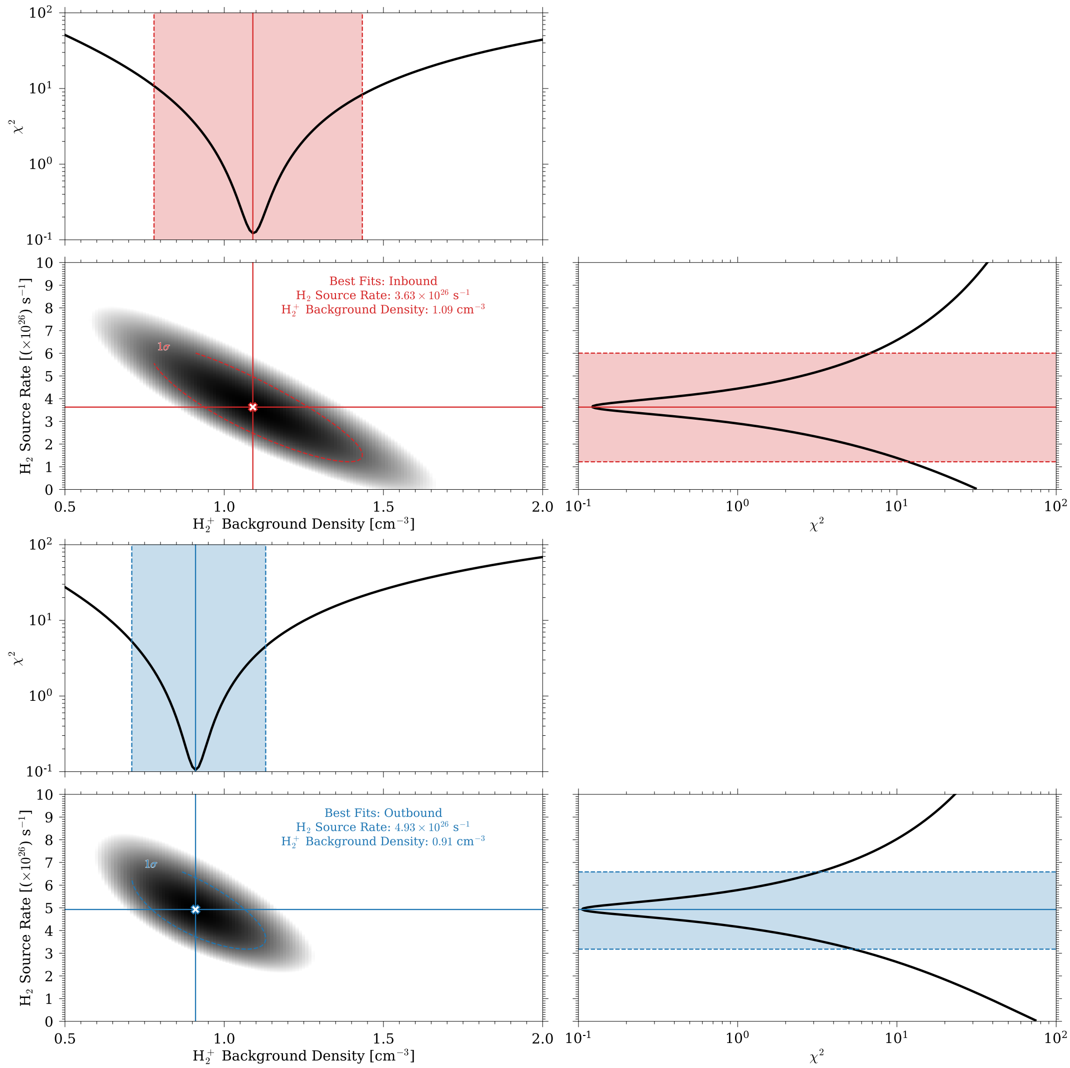

Figure 4. Corner plots showing the χ^2 distributions used to determine the best-fit H_2 source rate and H_2^+ background density for the inbound (top, red) and outbound (bottom, blue) legs of the *Juno* PJ45 flyby. The central panels show χ^2 heat maps as a function of H_2^+ background density (*x*-axis) and H_2 source rate (*y*-axis), with 1σ contours (dashed) and best-fit values (crosses). The top panels display χ^2 variations with H_2^+ background density at the best-fit H_2 source rate, while the right panels show χ^2 variations with H_2 source rate at the best-fit H_2^+ background density. In all panels, solid vertical and horizontal lines mark the best-fit values, and the shaded regions bounded by dashed lines denote the 1σ ranges.

the retrieved H_2 density profiles are nearly identical across both segments (Figure 6), the slightly enhanced H_2^+ densities observed at extended altitudes on the inbound leg imply a higher H_2^+ background density. This interpretation also agrees with model predictions that reproduce the H_2^+ PUIs observed between ~13–18 R_J (Szalay et al., 2022): their densities peak just beyond Europa's orbit due to radial advection in Jupiter's magnetosphere, consistent with the slightly larger value inferred on the anti-Jovian side, indicating that this "background" component represents an H_2^+ torus.

Having established excellent agreement between the simulated and observed H_2^+ densities, we now examine the corresponding neutral H_2 density profiles resulting from the best-fit source rates shown in Figure 6. At Europa's surface, the resulting H_2 densities range from ~(2.9–11) × 10^5 cm^{-3} for the inbound leg and ~(4.4–13) × 10^5 cm^{-3} for the outbound leg, with best-fit values of ~6.4 × 10^5 cm^{-3} and ~8.7 × 10^5 cm^{-3}, respectively. The shaded regions denote the range of densities obtained by varying the ionization rates and magnetospheric plasma speeds within their respective limits. Table 2 summarizes how the retrieved H_2 source rates depend on these

ADVANCING EARTH AND SPACE SCIENCES
Journal of Geophysical Research: Planets
10.1029/2026JE009724

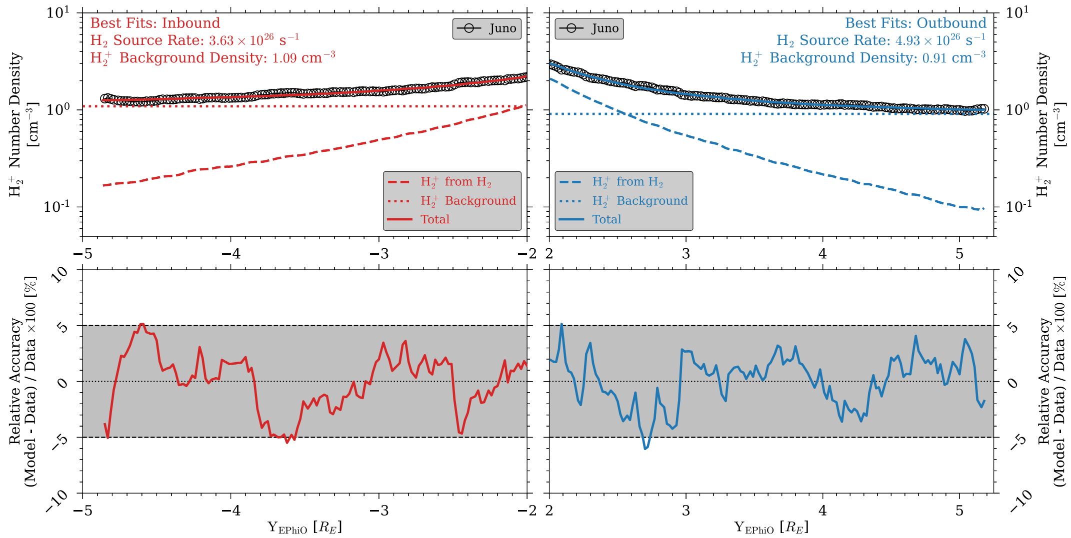

Figure 5. Comparison between observed and simulated H_2^+ pickup ion densities along *Juno*'s PJ45 flyby. The top panels show *Juno*/JADE measurements (solid black lines and circles) for the inbound (left) and outbound (right) segments, compared with results from simulated collisionless, purely thermal H_2 atmospheres. Dashed lines represent H_2^+ produced from the atmospheres resulting from the best-fit H_2 source rates, dotted lines indicate the best-fit H_2^+ background densities, and solid lines show their combined total for the inbound (red) and outbound (blue) cases. The bottom panels display the relative difference between the observed and simulated total H_2^+ densities with the shaded regions marking ±5%.

parameters: for both flyby segments, the best-fit H_2 source rate increases with increasing magnetospheric plasma speed and decreases with increasing ionization rate, reflecting the competing effects of pickup efficiency and ion production, while the best-fit H_2^+ background densities remain unchanged. Although photoionization is negligible (Table D1 in Appendix D), charge exchange with ambient magnetospheric ions (Table D2) further reduces the required best-fit source rates. The range of best-fit H_2 source rates obtained by varying these parameters (Table 2) aligns closely with the 1σ confidence intervals derived from the χ^2 fits in Figure 4, indicating that the retrieved source rates are robust across both statistical and environmental uncertainties.

To assess the impact of the straight-flow-vector approximation in our guiding-center model (Section 3.3), we repeated the outbound analysis using the deflected plasma streamlines and flow speeds of Szalay et al. (2024) with $v_0 = 100$ km/s, $H_I = 30$ km, and $\overline{\alpha} = 0.55$ (see Figure E1 in Appendix E). We find that the inferred H_2^+ background density is effectively unchanged (0.90 vs. 0.91 cm^{-3}), and that the corresponding H_2 source rate (5.69×10^{26} s^{-1}) lies slightly above the nominal range ((4.93–$5.51) \times 10^{26}$ s^{-1}; Table 2) obtained for comparable plasma flow speeds (100–112 km/s), but remains within the 1σ confidence intervals (Figures E2 and 5). This modest increase in H_2 source rate reflects the higher local plasma speeds along the deflected streamlines, as well as the slightly different locations at which they sample the neutral atmosphere (Figure E1). These results demonstrate that the straight-flow-vector approximation at the extended altitudes considered in this study does not introduce a significant bias in the inferred atmospheric properties. Moreover, they show that once a background H_2^+ component is included, a purely thermal H_2 atmosphere is sufficient to reproduce the *Juno*/JADE observations, even within the more detailed plasma interaction framework of Szalay et al. (2024).

Of course, there are notable caveats to this simplified approach. These 1D simulations neglect diurnal surface temperature gradients (e.g., Figure C1 in Appendix C), which are expected to produce local atmospheric asymmetries (e.g., Oza et al., 2019). Similarly, because these simulations are spherically symmetric, they neglect asymmetric effects arising from Coriolis and centrifugal forces. Such phenomena could naturally account for the slight difference in density profiles between the inbound and outbound legs (Figure 6), which are instead represented here by separate simulations with different source rates, effectively capturing this variability within the simplified framework. Nevertheless, the strong correspondence between the simulated and observed H_2^+ densities indicates that a purely thermal H_2 atmosphere, combined with a background contribution from an H_2^+ torus, can fully account for the magnitude and spatial variation of the H_2^+ PUIs measured by *Juno*.

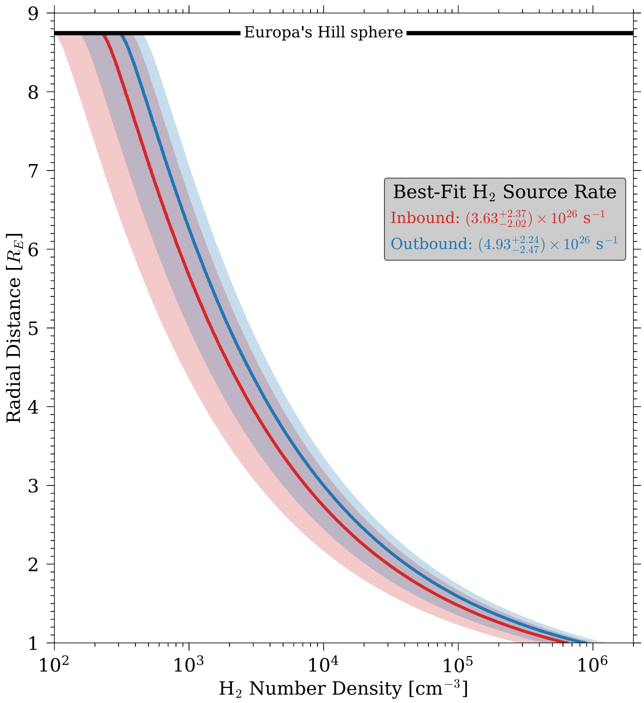

Figure 6. Radial H_2 number density profiles corresponding to the best-fit source rates derived from the inbound (red) and outbound (blue) legs of the *Juno* PJ45 flyby. Solid lines indicate the nominal best-fit solutions (mean electron-impact ionization rate and magnetospheric plasma speed), while shaded regions represent the range of density profiles obtained by varying the source rates according to the ionization rates and magnetospheric plasma speeds listed in Table 2. The black horizontal line marks the location of Europa's Hill sphere.

4.1.2. Nonthermal + Thermal H_2

Figure 7 shows the χ^2 distributions across the considered range of H_2 effective binding energies, E_b. A clear systematic trend is evident: as E_b increases, the inferred H_2 source rates increase while the H_2^+ background densities decrease. Increasing E_b from 0.01 to 0.06 eV requires larger H_2 source rates by roughly a factor of three, and by ~4–5 relative to the purely thermal atmosphere (Table E1 in Appendix E). In contrast, the inferred H_2^+ background densities decrease by only ~5%–7% with increasing E_b. The inbound-to-outbound ratios remain approximately constant at ~1.4 for the H_2 source rates and ~1.2 for the H_2^+ background densities across both the purely thermal and nonthermal + thermal solutions.

Figure 8 compares the observed and simulated H_2^+ densities along the PJ45 trajectory across the considered range of E_b. As with the purely thermal simulations (Figure 5), all cases reproduce the *Juno*/JADE H_2^+ PUI measurements within ±5% along both the inbound and outbound legs, indicating that the fits are statistically indistinguishable across the simulated purely thermal and nonthermal + thermal H_2 atmospheres. Unlike in Section 4.1.1, no additional variations in ionization rate or magnetospheric plasma speed were explored further; only their mean values were adopted (Table 1, Figure 3), as the uncertainty introduced by E_b spans a much larger range of possible outcomes.

The total H_2 density profiles resulting from the best-fit source rates and the relative contributions from the thermal and nonthermal components are shown in Figure 9. Across the considered range of E_b, the overall density structure remains qualitatively similar. Quantitatively, increasing E_b leads to larger scale heights and more gradual density gradients: densities near the surface decrease, while those near Europa's Hill sphere increase. Despite these subtle changes, the atmosphere remains predominantly thermal throughout most of the domain. For $E_b \leq 0.04$ eV, the nonthermal component never exceeds the thermal component below Europa's Hill sphere; even for $E_b = 0.05$ and 0.06 eV, this occurs only beyond ~7 R_E and ~6 R_E, respectively. Thus, even when a nonthermal source is included, the atmosphere sampled by *Juno* remains predominantly thermal, sustained by the continual return and re-emission of H_2 molecules from Europa's icy surface. A distinct background component is required to reproduce the observations and dominates the H_2^+ signal beyond $|Y_{EPhiO}| \sim 2 - 3R_E$ (Figures 5 and 8). Because Szalay et al. (2024) did not account for this background contribution, they inferred that Europa's neutral H_2 must be highly nonthermal to reproduce the measured H_2^+ densities. However, as discussed in Section 4.1.1 and shown in Appendix E (Figure E2 therein), when this background component is included within the same modeling framework, the *Juno*/JADE observations can be reproduced without invoking a strongly nonthermal H_2 atmosphere. Thus, we conclude that the apparent nonthermal signature in the *Juno*/JADE data reflects the presence of Europa's H_2^+ torus.

4.2. Collisional H_2+O_2+H+O Atmosphere

4.2.1. Purely Thermal H_2

Including interspecies collisions in an H_2+O_2+H+O atmosphere with a purely thermal H_2 component—using the best-fit H_2 source rates inferred from the collisionless H_2 atmosphere—leads to a slight reduction in H_2 escape rates and a corresponding enhancement of H_2 densities (Figure F1 in Appendix F). As a result, agreement with the *Juno*/JADE data worsens from within ±5% to within ±10% while requiring lower best-fit H_2^+ background densities (Figure F2 in Appendix F). The impact of collisions on the fit is most evident between $2R_E \lesssim |Y_{EPhiO}| \lesssim 3R_E$, where Europa's atmospheric H_2 still contributes significantly to the observed PUI signal. At larger distances, the *Juno*-detected H_2^+ becomes dominated by the H_2^+ torus (e.g., Figures 5 and 8), reducing the apparent collisional enhancement of H_2 densities, despite this effect persisting to the Hill sphere.

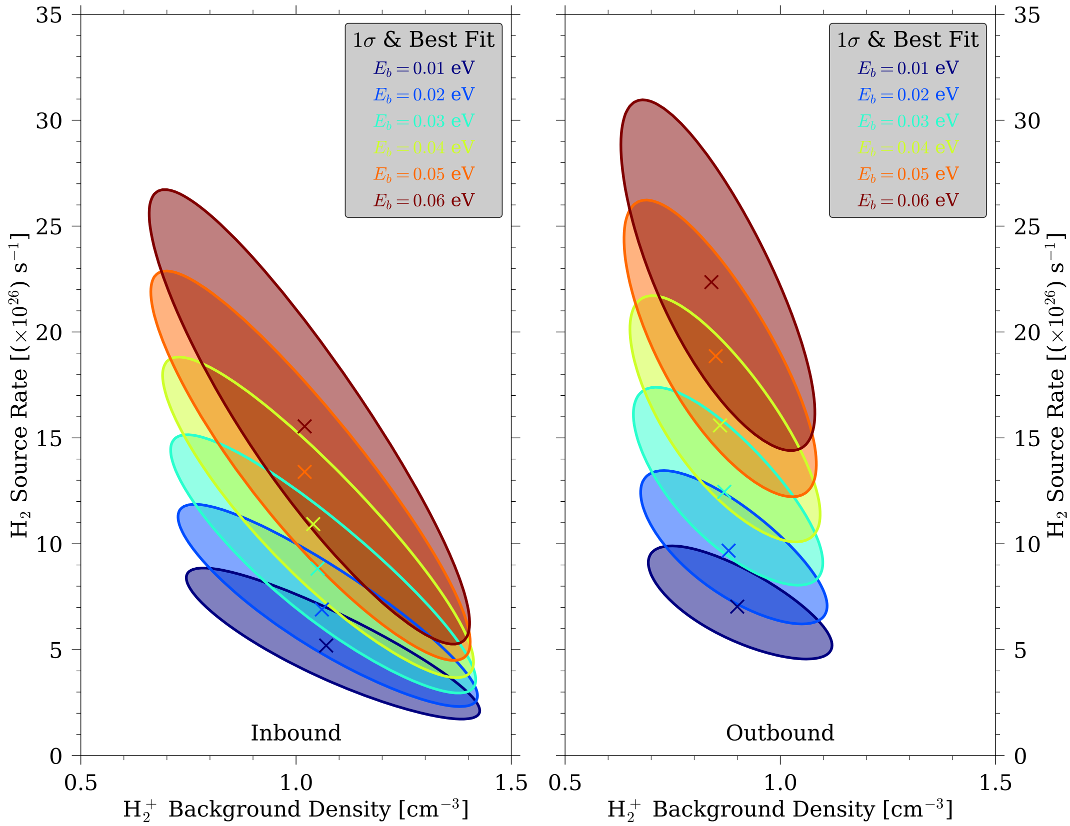

Figure 7. Best-fit H_2^+ background densities (x-axis) and H_2 source rates (y-axis) for the simulated collisionless, nonthermal + thermal H_2 atmospheres along the inbound (left) and outbound (right) legs of the PJ45 flyby. Each color corresponds to a different assumed effective binding energy (E_b) for sputtered H_2 (see Equation 3 and Figure 2): 0.01 eV (dark blue), 0.02 eV (blue), 0.03 eV (cyan), 0.04 eV (yellow), 0.05 eV (orange), and 0.06 eV (dark red), with crosses marking the best fits and shaded ellipses representing their 1σ confidence intervals. For reference, Table E1 in Appendix E lists the corresponding best-fit values and compares them with those obtained for the purely thermal simulations.

Allowing both the H_2 source rates and H_2^+ background densities to vary identifies revised best-fit parameters (Figure F3 in Appendix F), with $\Phi_{0,H_2} = (3.05–4.29) \times 10^{26}$ s^{-1} and $n_{0,H_2^+} = 0.91–1.11$ cm^{-3}. Figure 10 shows that subsequent DSMC simulations using these updated H_2 source rates restore agreement with the *Juno*/JADE data to within ±5%. Repeating the joint optimization of the H_2 source rates and H_2^+ background densities results in only minor adjustments to the inbound solution, with $\Phi_{0,H_2} = 3.17 \times 10^{26}$ s^{-1} and $n_{0,H_2^+} = 1.10$ cm^{-3} (Figure F4 in Appendix F), while the outbound best-fit values remain unchanged at $\Phi_{0,H_2} = 4.29 \times 10^{26}$ s^{-1} and $n_{0,H_2^+} = 0.91$ cm^{-3}. Thus, the outbound solution is optimal, and the small adjustment to the inbound values indicates that the inferred parameters are close to convergence. Accordingly, although a marginally improved solution for the inbound leg of the flyby exists, the ∼4% difference is negligible for the results presented below; we therefore adopt $\Phi_{0,H_2} = 3.05 \times 10^{26}$ s^{-1} as the fiducial H_2 source rate, while the outbound leg uses the optimal value of $\Phi_{0,H_2} = 4.29 \times 10^{26}$ s^{-1}. These values differ by only ∼15% from those inferred in the collisionless cases, while the required H_2^+ background densities remain effectively unchanged, and both parameters lie well within their respective 1σ confidence intervals (Figures F3 and F4 in Appendix F). Thus, including interspecies collisions does not alter the principal conclusion of this study: a purely thermal H_2 atmosphere, combined with a background H_2^+ torus with local densities of ∼0.9–1.1 cm^{-3}, reproduces the H_2^+ pickup ions detected by *Juno* during the PJ45 flyby.

Figure 11 presents the simulated number density and line-of-sight (LOS) column density profiles for H_2, O_2, H, and O in Europa's atmosphere for the inbound and outbound legs of the PJ45 flyby. As expected, the atmosphere is O_2-dominated below ∼100 km and across Europa's disk, with surface densities of $n_0 \sim (4–5) \times 10^7$ cm^{-3} and

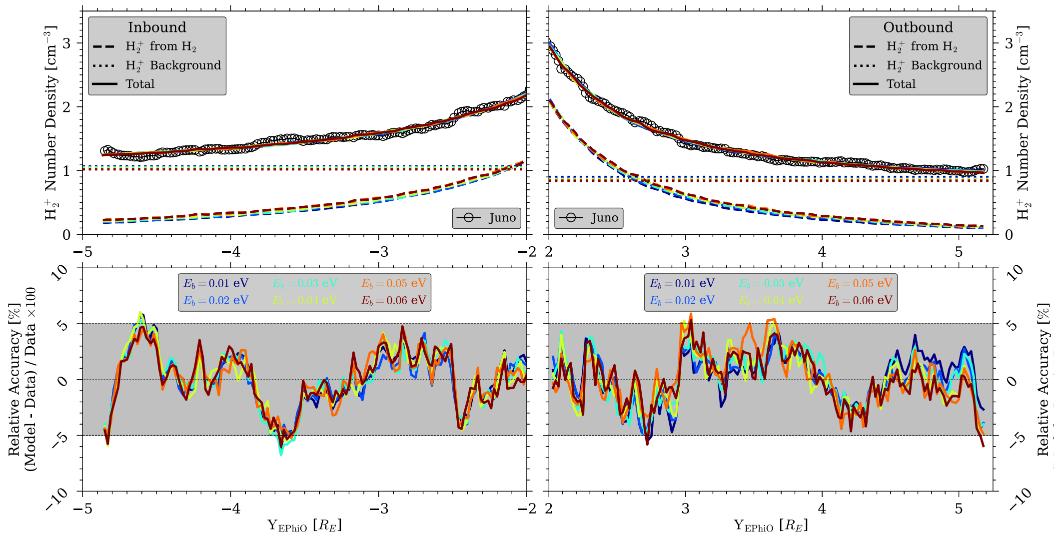

Figure 8. Comparison between observed and simulated H_2^+ pickup ion densities along *Juno*'s PJ45 flyby. The top panels show JADE measurements (solid black lines and circles) for the inbound (left) and outbound (right) segments, compared with results from simulated collisionless, nonthermal + thermal H_2 atmospheres. Dashed lines represent H_2^+ produced from the H_2 atmospheres resulting from the best-fit source rates, dotted lines indicate the best-fit H_2^+ background densities, and solid lines show their combined total. Each color corresponds to a different assumed effective binding energy (E_b) for sputtered H_2 (see Equation 3 and Figure 2): 0.01 eV (dark blue), 0.02 eV (blue), 0.03 eV (cyan), 0.04 eV (yellow), 0.05 eV (orange), and 0.06 eV (dark red). The bottom panels display the relative difference between the observed and simulated total H_2^+ densities with the shaded regions marking ±5%. The model–data comparisons and χ^2 distributions for each E_b are provided in Appendix E: Figures E3–E8.

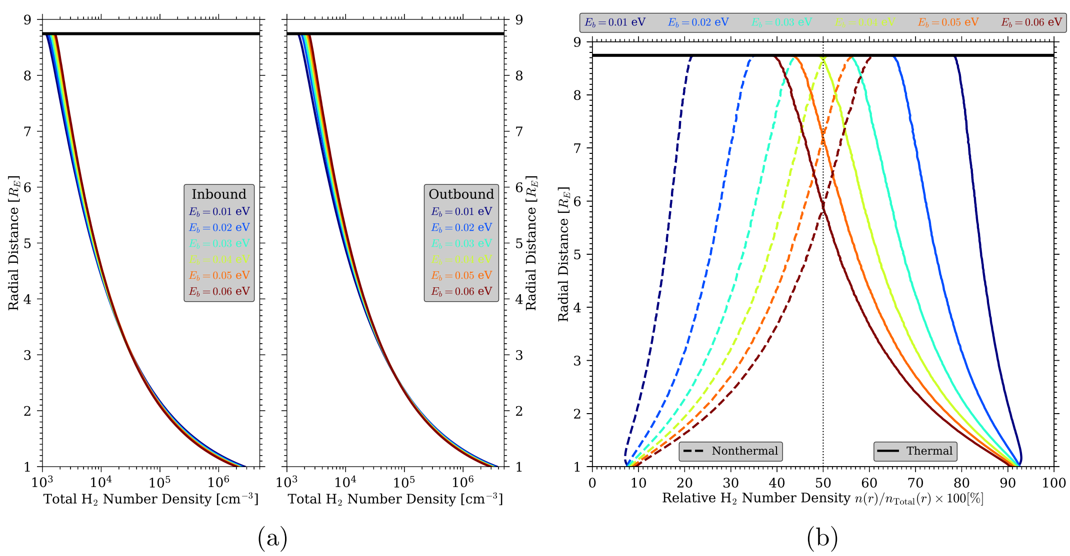

Figure 9. (a) Simulated total density profiles for the collisionless, nonthermal + thermal H_2 atmospheres corresponding to the best-fit H_2 source rates derived for the inbound (left) and outbound (right) legs of the *Juno* PJ45 flyby. (b) Relative contributions of the nonthermal (dashed lines) and thermal (solid lines) components, expressed as fractions of the total H_2 density as a function of radial altitude. Colors indicate the assumed effective binding energies (E_b) for sputtered H_2: 0.01 (dark blue), 0.02 (blue), 0.03 (cyan), 0.04 (yellow), 0.05 (orange), and 0.06 eV (dark red). Black horizontal lines denote Europa's Hill sphere.

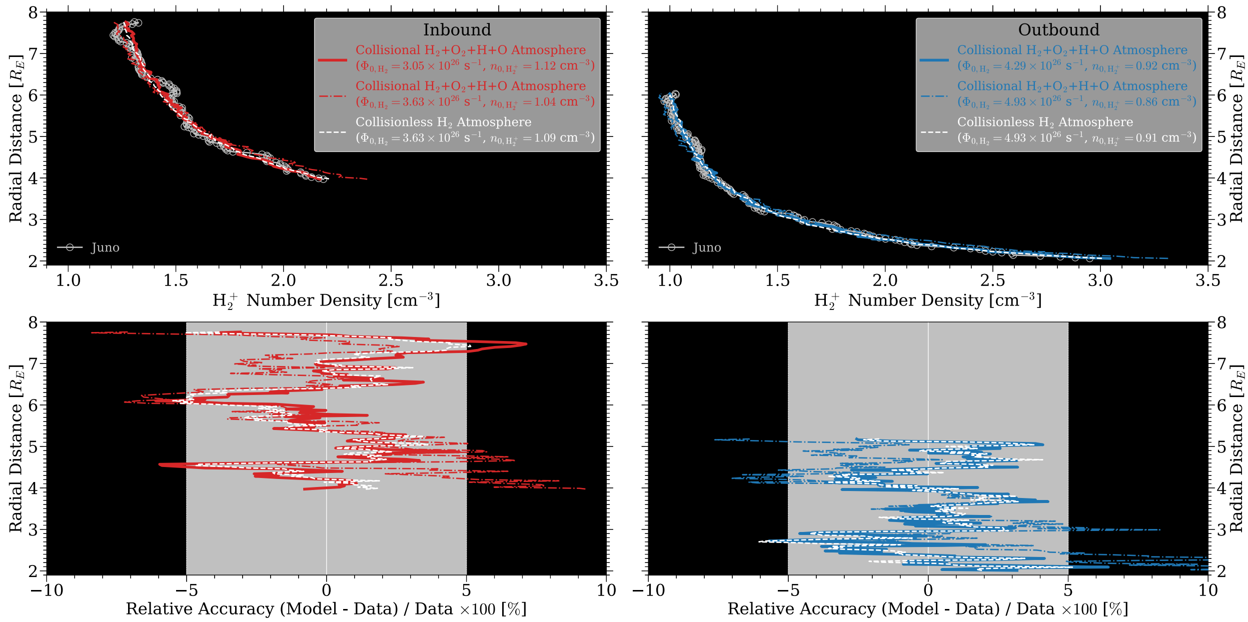

Figure 10. Comparison between modeled and observed H_2^+ pickup ion densities for the inbound (left) and outbound (right) legs of the PJ45 flyby. Top panels: Total H_2^+ densities (H_2^+ from atmospheric H_2+H_2^+ torus) from the collisionless H_2 (dashed white lines) and collisional H_2+O_2+H+O (thin dash-dotted and thick solid red and blue lines) atmospheres compared with *Juno*/JADE observations (solid silver lines and circles). The dashed black lines show the best-fit collisionless results; thin dash-dotted red and blue lines correspond to collisional simulations using these same H_2 source rates but with updated H_2^+ background densities; and thick solid red and blue lines show the final best-fit collisional solutions in which both the H_2 source rate and H_2^+ background density are adjusted. Bottom panels: Relative accuracy between modeled and observed H_2^+ pickup ion densities, comparing the best-fit collisional and collisionless models shown in the top panels. The solutions closely overlap in all panels, reflecting the consistency between the initial collisionless fits and the corresponding collisional simulations.

peak LOS column densities at the limb of $\sim$(5–7) × 10^{14} cm^{-2}. In contrast, due to its larger scale height, H_2—with $n_0 \sim$ (6–8) × 10^5 cm^{-3} and peak LOS column densities of $\sim 10^{14}$ cm^{-2}—becomes the dominant constituent above $\sim$100 km and beyond the limb. The H and O components produced by electron-impact dissociation and dissociative ionization of their parent molecules remain minor near the surface and across the disk. Off disk, their densities exceed those of the nonthermal O_2 beyond $\sim$2–4R_E (Figure 11b); the corresponding crossover in radial altitude likewise occurs at $\sim$2–4R_E ($\sim$3,000–6,000 km), above the range shown in Figure 11a.

Table 3 lists the corresponding radial column densities ($\int n(r)dr$) and escape rates, where the former is equivalent to the"vertical column densities" often reported from remote-sensing observations. Indeed, these values are represented in the LOS profiles at the center of the disk in Figure 11b, while subsequent values are calculated within LOS bins extending outward in 0.05 R_E increments. Despite H_2 having surface densities ~60 times smaller than O_2, its column densities are only $\sim$3.5× smaller. As expected, H_2 is the dominant escaping species, followed by H, O, and finally O_2. Overall, the simulations imply that $\sim$(5.1–7.3) × 10^{26} H/s and $\sim$(3.6–4.9) × 10^{25} O/s escape Europa's atmosphere, supplying the Jovian magnetosphere with comparable mass loss rates for hydrogen ($\sim$0.86–1.2 kg/s) and oxygen ($\sim$0.96–1.3 kg/s).

4.2.2. Nonthermal + Thermal H_2

We next assess whether including a nonthermal H_2 component in collisional H_2+O_2+H+O atmospheres alters the conclusions of Section 4.1.2. When the H_2 source rates inferred from the collisionless nonthermal + thermal simulations are applied to collisional atmospheres (Figure G1 in Appendix G), the resulting χ^2 curves become significantly shallower (Figure G2 in Appendix G). Accordingly, the collisional models no longer reproduce the *Juno*/JADE H_2^+ observations; model–data discrepancies increase systematically with H_2 effective binding energy (see also Figure G2 in Appendix G). This behavior reflects the sensitivity of nonthermal H_2 to collisions with O_2: larger E_{b,H_2} requires higher H_2 and O_2 source rates, which increase the resulting O_2 density and, in turn, the $H_2 + O_2$ collision frequency. These collisions suppress the escape of nonthermal H_2 and redirect a larger fraction of molecules back toward the surface, where they thermalize, enhancing the total H_2 density. Consequently, the

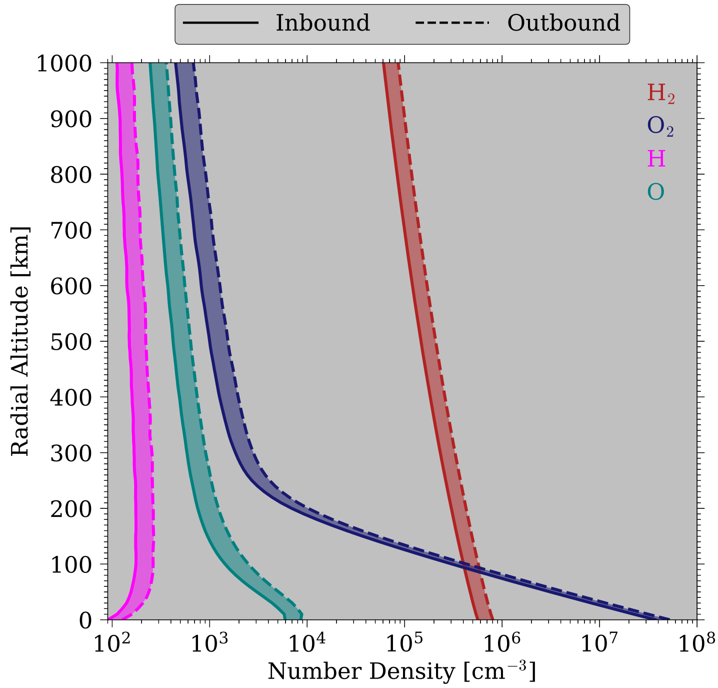

(a)

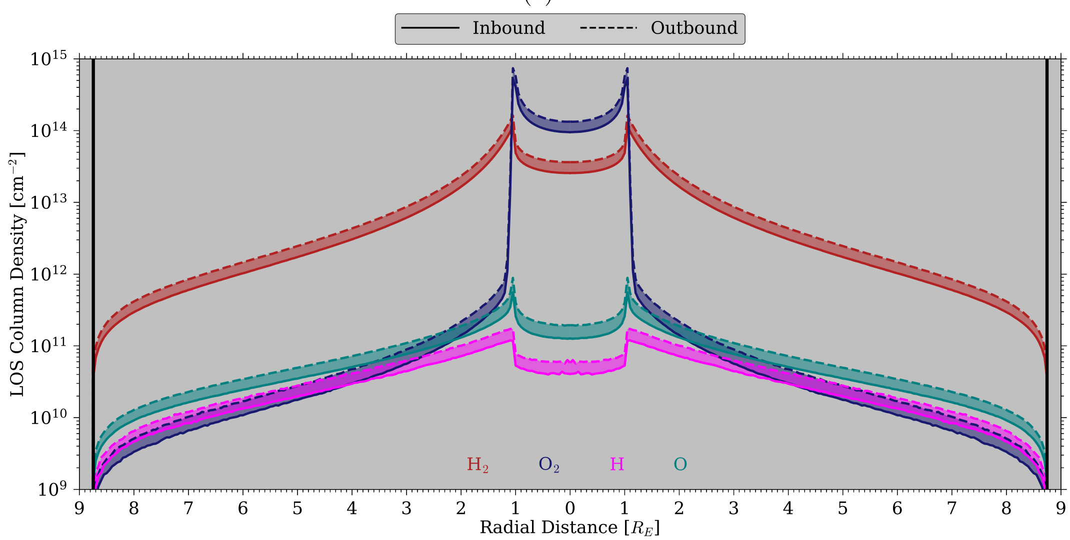

(b)

Figure 11. (a) Best-fit number density and (b) line-of-sight (LOS) column density profiles for the simulated H_2 (red) + O_2 (blue) + H (pink) + O (teal) atmosphere corresponding to the inbound (solid lines) and outbound (dashed lines) legs of the PJ45 flyby. The solid black vertical lines in (b) indicate Europa's Hill sphere.

nonthermal component never exceeds $\sim$20% of the total H_2 density (Figures G3–G8 in Appendix G), and the enhanced thermal population leads to a substantial overprediction of H_2^+ and a marked degradation in model–data agreement.

In principle, as with the purely thermal simulations (e.g., Figures F3 and F4 in Appendix F), one could attempt to recover agreement by iteratively re-optimizing the H_2 source rate and H_2^+ background density for each assumed E_{b,H_2}. In practice, however, this approach is neither tractable nor physically informative. Each iteration would require a multispecies DSMC simulation and would need to be repeated for every value of E_{b,H_2}—itself a free parameter that cannot be constrained by the available data—rendering a comprehensive exploration

Table 3
Model Calculations for Europa's H_2+O_2+H+O *Atmosphere for the Inbound and Outbound Legs of the PJ45 Flyby*

	Species	Radial column density[a] [cm^{-2}]	Escape rate [s^{-1} (kg/s)]
Inbound	H_2	2.6×10^{13}	2.4×10^{26} (0.80)
	O_2	9.5×10^{13}	4.1×10^{24} (0.22)
	H	4.1×10^{10}	3.8×10^{25} (0.064)
	O	1.2×10^{11}	2.8×10^{25} (0.74)
Outbound	H_2	3.6×10^{13}	3.4×10^{26} (1.1)
	O_2	1.3×10^{14}	6.0×10^{24} (0.32)
	H	5.8×10^{10}	5.4×10^{25} (0.090)
	O	1.9×10^{11}	3.7×10^{25} (0.98)

[a]Radial column densities are computed by integrating the best-fit DSMC number-density profiles; the statistical uncertainty in the simulated profiles is negligible relative to the fitting uncertainty in the source rates and is therefore not listed.

computationally prohibitive. Moreover, the *Juno*/JADE observations of H_2^+ do not provide sensitivity to atmospheric contributions in the altitude range where the nonthermal population becomes significant. Because interspecies collisions with O_2 reduce the nonthermal H_2 population relative to the collisionless case, the collisionless models that initially provided the optimal fit represent upper limits on the nonthermal H_2 contribution. Even under these most favorable assumptions, the nonthermal component exceeds the thermal population below Europa's Hill sphere only for $E_b > 0.04$ eV, with the lowest crossover altitude occurring at $\sim 6\ R_E$ (Figure 9b). Above these altitudes, however, the H_2^+ signal detected by *Juno* is already dominated by the background H_2^+ torus (e.g., Figures 5 and 8), such that any atmospheric contribution—thermal or nonthermal—would not be discernible.

Taken together, these constraints imply that any H_2^+ produced from atmospheric H_2 within the altitude range sampled by *Juno*—where the atmospheric contribution to the observed signal is detectable above the background—must originate predominantly from the thermal component. Accordingly, while nonthermal H_2 production mechanisms undoubtedly operate at Europa (e.g., surface sputtering, dissociation of H_2O, and interactions with ambient plasma and energetic neutrals), their net contribution to the atmosphere sampled by *Juno* must be small. For these reasons, the collisional H_2+O_2+H+O simulations with a purely thermal H_2 component are adopted as the fiducial models.

4.3. Comparisons With Previous Studies

The results presented above are derived specifically from simulations designed to reproduce the atmospheric and plasma conditions sampled by *Juno* during the PJ45 flyby of Europa. As such, the inferred source rates, influence of collisions, and relative importance of thermal and nonthermal H_2 components are necessarily conditioned on the local environment probed during that encounter, including the ambient plasma environment, viewing geometry, and the contemporaneous state of Europa's atmosphere. They should therefore not be interpreted as universally representative of Europa's atmosphere under all circumstances. Nevertheless, comparisons with earlier studies provide useful context for interpreting these results.

4.3.1. Comparison With Previous Models

With similar O_2 and H_2 surface densities as those considered by Carberry Mogan et al. (2024)—$n_0 = 10^{7-8}$ O_2/cm^3 and $n_0 = 10^6$ H_2/cm^3—and adopting electron-impact dissociation rates for O_2 roughly twice those used in that study, our simulated O density profiles are comparable, implying an enhancement due to collisions with O_2 and a suppression of O escape relative to a collisionless atmosphere (cf. Figures 2 and 4 therein). Whereas Carberry Mogan et al. (2024) treated nonthermal O+O_2 collisions as the sole mechanism for O_2 escape, here we additionally include surface sputtering as well as collisions between thermal (recycled) and nonthermal (sputtered) O_2. As a result, the escaping O_2 population comprises both molecules sputtered directly from the surface (∼57–63% of the total) and recycled molecules that re-emit thermally and subsequently undergo nonthermal escape-triggering collisions (∼37–43%). Notably, the recycled fraction of total O_2 escape increases with higher O_2 surface densities—from 37% to 43% for the inbound and outbound legs—while the sputtered fraction correspondingly decreases, from 63% to 57%. This mixed escaping population not only contrasts with Carberry Mogan et al. (2024) and S&M06, where O_2 escape arises exclusively from nonthermal collisions, but also with collisionless models such as V&W18, where it is produced entirely by surface sputtering. Despite these differences, we obtain an O/O_2 escape ratio of ∼6–7, well within the range reported by Carberry Mogan et al. (2024), ∼2–10, though notably distinct from the values of S&M06 (∼0.8) and V&W18 (∼0.3).

S&M06 assumed source rates of $\sim 2 \times 10^{27}$ H_2 s^{-1} and $\sim 1 \times 10^{27}$ O_2 s^{-1}, yielding escape rates of $\sim 1.9 \times 10^{27}$ H_2 s^{-1} and $\sim 2.7 \times 10^{26}$ O_2 s^{-1}. Their simulations also included H and O produced by direct surface sputtering and by photo- and electron-impact dissociation, with corresponding escape rates of 9.7×10^{25} H s^{-1} and 2.2×10^{26} O s^{-1}. These escape rates and the resulting column densities (Table 2 therein) are larger than those derived here. Further, their model produced considerably higher escape fractions (defined as the ratio of escape rate to source rate) for H_2 (∼95%) and O_2 (∼27%) than those obtained in this study (∼79% for H_2 and ∼2.7% for O_2). These discrepancies likely arise from their inclusion of ion–neutral collisions, but because S&M06 do not specify the energy distributions or cross-section assumptions used in their ion–neutral coupling, a quantitative comparison is not possible. Nevertheless, the nonthermal tail in the H_2 upward flux velocity distribution at 1,000 km that they attribute to these collisions (Figure 3 therein) represents only a small fraction of the overall distribution. Thus, consistent with our findings, even when nonthermal production mechanisms are considered, the H_2 component in Europa's atmosphere remains predominantly thermal at the altitudes relevant to the *Juno* flyby.

S&M06 obtained total escape rates—in both atomic and molecular form—for hydrogen (∼6.5 kg/s) and oxygen (∼20.1 kg/s) that are several times larger than the values derived here (Table 3). This discrepancy implies that the atmosphere sourcing the neutral torus required to reproduce the *Juno*/JADE observations of H_2^+ is less dense than that predicted by S&M06 and by subsequent models that adopted their atmospheric escape rates as inputs (Smith et al., 2019). Thus, future work will test whether the reduced escape rates derived here produce a neutral torus whose associated ion population can quantitatively reproduce both the H_2^+ densities inferred during the PJ45 flyby and the more extended toroidal structure observed by *Juno* at larger radial distances from Europa (Szalay et al., 2022).

V&W18 adopted stoichiometric H_2:O_2 source rates intermediate between those derived here and those assumed by S&M06; while their O_2 densities fall within the same range, they obtained lower H_2 densities than in both studies. Their simulated H_2 and O_2 escape rates exceed those derived here, yielding higher mass loss rates of hydrogen (∼1.8 kg/s) and oxygen (∼4.8 kg/s); when including escaping H and O, these increase to ∼1.9 kg/s and ∼5.6 kg/s, respectively. V&W18 employed a Sigmund–Thompson–type distribution—similar to Equation 3, but with a cut-off energy E_c corresponding to the maximum energy transferable in a binary collision with an impinging charged particle—to describe surface sputtering, but did not specify the values used for E_b or E_c. Nevertheless, their comparatively large escape fraction for O_2 (27%) suggests either the adoption of a higher effective binding energy than is typically assumed (e.g., $E_b > 0.015$ eV) and/or the influence of integrating over a truncated energy distribution, leading to values exceeding those obtained here and in previous collisionless models (Plainaki et al., 2012, 2013). Interestingly, the O_2 escape fraction is the same in S&M06 and V&W18, despite the two studies invoking fundamentally different mechanisms. At the same time, their lower adopted O_2 reaction rate ($\sim 1.6 \times 10^{-6}$ s^{-1}, compared to $(4.84–5.07) \times 10^{-6}$ s^{-1} here) allows thermally recycled O_2 to persist longer in the atmosphere and accumulate to larger densities. For H_2, the enhanced escape and reduced density relative to those derived here arise from a combination of two factors: a warmer uniform surface temperature (125 K vs. 98 K here) and a nonthermal sputtered component.

4.3.2. Comparison With Remote-Sensing Observations

We next compare the atmospheric densities derived here from in-situ measurements with those inferred from remote-sensing observations. The O_2 radial column densities obtained here ($\sim(0.95–1.3) \times 10^{14}$ cm^{-2}) are a factor of ∼3–6 lower than those inferred from the most recent HST UV auroral observations, $(3–6) \times 10^{14}$ cm^{-2} (Roth et al., 2016), and from Keck optical auroral emissions, $\sim 4 \times 10^{14}$ cm^{-2} (de Kleer et al., 2023). However, significant uncertainties in the magnetospheric electron densities and temperatures used to infer these values from auroral emissions imply that this discrepancy does not necessarily indicate an inconsistency. Indeed, inferred O_2 column densities have systematically decreased as progressively improved in-situ constraints on the ambient electron environment became available. For example, Hall et al. (1995) inferred column densities of $(1–2) \times 10^{15}$

Table 4
Water-Equivalent Loss (L) and Replenishment (R) Rates From the Simulated H_2+O_2+H+O *Atmospheres Presented in This Study (Figure 11)*

	L:Escape[a] [kg/s]	L: Ionization[b] [kg/s]	R: Return[c] [kg/s]
Inbound	−7.8	-8.0×10^{-3}	$+8.6 \times 10^{-2}$
Outbound	−11	-1.2×10^{-2}	$+1.2 \times 10^{-1}$

[a]Escape of one H_2 molecule or two H atoms is equivalent to the loss of one H_2O molecule by removing its hydrogen content. [b]Ionization of one H_2 molecule or dissociative ionization of two H_2 molecules removes the hydrogen content of one H_2O molecule (direct ionization of H is negligible). [c]Every two H atoms returning to the surface are equivalent to restoring the hydrogen content of one H_2O molecule to the ice (H_2 molecules are assumed to not condense on return).

O_2 cm^{-2} from the earliest HST observations of Europa's UV aurora assuming total electron densities of 40 cm^{-3} based on *Voyager* data (Bagenal, 1994). Subsequent studies that incorporated higher electron densities inferred from *Galileo* data (63–290 cm^{-3}; Bagenal et al., 2015) demonstrated that lower O_2 column densities can produce comparable auroral emissions (e.g., Roth et al., 2016). Thus, a reanalysis of existing HST and Keck data sets using updated electron distributions from *Juno*/JADE (e.g., Ellis et al., 2026; Sarkango et al., 2025) would provide a critical test of whether the lower O_2 column densities derived here are consistent with the observed auroral morphology. If such analyses were to confirm that these values remain lower, this would suggest that the commonly assumed 2:1 stoichiometric coupling between H_2 and O_2 source rates may be overly restrictive at Europa. Increasing O_2 production under this assumption would necessarily overproduce H_2^+ compared to the *Juno*/JADE measurements, whereas a lower H_2:O_2 ratio could reconcile the in-situ and remote-sensing constraints.

A further apparent discrepancy concerns longitudinal asymmetries. HST observations by Roth et al. (2016) revealed brighter auroral emissions on the dusk hemisphere compared to the dawn hemisphere. This was interpreted as evidence for a denser O_2 atmosphere on the dusk side (Roth et al., 2016), which was later explained by diurnal atmospheric variations (Oza et al., 2019) and supported by trends in the oxygen line ratio from dawn to dusk (Roth, 2021). In our simulations, however, the modest differences between the inbound (dusk) and outbound (dawn) profiles (Figure 11) suggest the opposite. This is not necessarily a contradiction: in a 1D model such as those employed here, the inbound/outbound differences simply reflect the different source rates inferred from the two fits, whereas the 3D model of Oza et al. (2019), which assumed a globally uniform source rate, explicitly incorporated diurnal surface temperature variations. If a dusk-over-dawn O_2 asymmetry is indeed present, the fact that our best-fit H_2 densities are larger at dawn (outbound) than at dusk (inbound) may indicate that H_2 and O_2 exhibit distinct longitudinal responses. Such a phase offset would be physically plausible, since H_2 migrates more efficiently across the surface and has a longer lifetime (Table 1) than O_2, and is more susceptible to Coriolis and centrifugal forces at extended altitudes. A full 3D treatment will be required to assess whether these dynamical differences naturally produce the opposing asymmetries implied by remote-sensing observations and by the best-fit solutions derived here for in-situ measurements.

Recent analyses of HST Ly-α observations of Europa's hydrogen corona suggest H source rates on the order of $\sim 10^{27}$ H/s (Roth et al., 2026), exceeding the H production expected from H_2 dissociation. The inferred hydrogen temperatures ($\sim$1,000 K–5,100 K) are also lower than expected from dissociative processes. Although the steady-state H_2 outgassing rates derived here ($\sim$(4–6) $\times 10^{27}$ s^{-1}) exceed the H source rates inferred from HST observations, H_2 loss is dominated by escape rather than reactions, implying that only a small fraction of H_2 is converted into H. Indeed, the radial column densities derived here for H produced via electron-impact dissociation of H_2 ($\sim$(4–6) $\times 10^{10}$ cm^{-2}) are $\sim$20–35 times lower than those inferred from the HST observations ($\sim 1.4 \times 10^{12}$ cm^{-2}). Thus, reconciling the large H source rates therefore requires the presence of an additional source of atomic hydrogen, consistent with the interpretation of Roth et al. (2026), who suggest that direct release of H from the surface may constitute the dominant source.

4.3.3. Surface Erosion

Finally, following Szalay et al. (2024), we express the hydrogen-bearing loss processes in terms of an H_2O-equivalent budget to assess the implications for Europa's surface erosion. Specifically, loss rates calculated for H_2 and H are converted into mass loss rates by attributing to each loss the mass of an H_2O molecule (18.02 AMU), thereby tracking the removal of water through its hydrogen content; as in Szalay et al. (2024), oxygen-bearing losses are not considered here. Table 4 summarizes the resulting water-equivalent loss and replenishment rates obtained from the H_2+O_2+H+O simulations (Figure 11). Atmospheric escape of H_2 and H corresponds to a mass loss rate of $\sim$7.8–11 kg s^{-1}, electron-impact ionization and dissociative ionization of H_2 removes $\sim(0.80-1.2) \times 10^{-2}$ kg s^{-1}, and H returning to the surface replenishes $\sim(0.86-1.2) \times 10^{-1}$ kg s^{-1}. In these simulations, all ionization is treated as a net loss from the neutral atmosphere, with nascent H_2^+ or H^+ assumed to be picked up by the Jovian magnetosphere. Accordingly, the ionization losses represent upper limits, while the

H-return values are lower limits, as they exclude any contribution from PUIs that subsequently re-impact the ice. However, even if all such ionized atoms and molecules returned to the surface and replenished the ice, neutral escape would still overwhelmingly dominate the water-equivalent loss budget. These results therefore reinforce the conclusion of Szalay et al. (2024) that radiolysis-driven neutral escape is a major driver of Europa's surface erosion, while refining that picture by showing that (a) only $\sim 0.1\%$ of the water-equivalent loss proceeds via ionization, and (b) dissociated H returning to the surface offsets that channel by roughly an order of magnitude, yet has a negligible impact on the overall erosion rate.

5. Conclusion

In this study we applied a series of single-species (H_2) and multispecies ($H_2 + O_2 + H + O$) DSMC models of Europa's atmosphere to interpret the H_2^+ pickup ions measured by *Juno*/JADE during the PJ45 flyby. To reproduce both the magnitude and spatial structure of the observed H_2^+ signatures, the measurements require the presence of both a local contribution from atmospheric H_2 and a background H_2^+ torus. The simulated escape rates demonstrate that comparable amounts of hydrogen ($\sim$0.86–1.2 kg/s) and oxygen ($\sim$0.96–1.3 kg/s) are supplied to the Jovian magnetosphere and confirm that atmospheric escape is a leading driver of surface erosion at Europa. Below we summarize the key findings from this work:

- Reproducing the *Juno*/JADE H_2^+ measurements requires both an atmospheric contribution and a Europa-sourced H_2^+ torus. When an H_2^+ torus with local densities of $\sim 0.9–1.1\ \mathrm{cm^{-3}}$ is included, DSMC and guiding-center models reproduce the data to within $\pm 5\%$ across $\sim 4\ R_E$ along both the inbound and outbound legs of the PJ45 flyby at distances beyond $\sim 2\ R_E$.
- In Europa's H_2+O_2+H+O atmosphere, best-fit H_2 source rates of $\sim(3.05–4.29) \times 10^{26}\ \mathrm{s^{-1}}$ yield surface densities of $\sim(6–8) \times 10^5\ \mathrm{cm^{-3}}$, radial column densities of $\sim(3–4) \times 10^{13}\ \mathrm{cm^{-2}}$, and LOS limb abundances of $\sim 10^{14}\ \mathrm{cm^{-2}}$, resulting in escape rates of $\sim(2–3) \times 10^{26}\ \mathrm{s^{-1}}$. Assuming a 2:1 stoichiometric ratio for H_2:O_2 source rates yields O_2 surface densities of $\sim(4–5) \times 10^7\ \mathrm{cm^{-3}}$, radial column densities of $\sim 10^{14}\ \mathrm{cm^{-2}}$, limb abundances of $\sim(5–7) \times 10^{14}\ \mathrm{cm^{-2}}$, and escape rates of $\sim(4–6) \times 10^{24}\ \mathrm{s^{-1}}$. Lifetimes for H_2 and O_2, as well as the production rates of their dissociation products (H and O) and H_2^+ PUIs, are computed using updated electron fluxes from the most recent JADE data set.
- Although nonthermal H_2 production mechanisms are physically expected at Europa, they are not required to reproduce the *Juno*/JADE observations. In collisionless simulations, purely thermal and nonthermal + thermal H_2 atmospheres fit the data equally well by trading off the relative contributions from atmospheric H_2 and the H_2^+ torus, highlighting an inherent degeneracy in the interpretation. Once collisions with O_2 are included, however, this degeneracy is broken, as nonthermal H_2 is scattered, with a substantial fraction redirected back toward the surface where it thermalizes and enhances the thermal population. Applying nonthermal H_2 source rates inferred from collisionless simulations to collisional atmospheres therefore leads to systematic overproduction of H_2^+ and a degradation of the fit. Restoring agreement would require iterative multispecies simulations to identify new best-fit H_2 source rates and H_2^+ background densities; however, regardless of such adjustments, the conclusion remains that the H_2 component in Europa's atmosphere is predominantly thermal.

Together, these results demonstrate that Europa's H_2 atmosphere during the PJ45 flyby is predominantly thermal—supplied by radiolysis but whose structure and escape are shaped by surface temperature, recycling within the regolith, and collisions with the concomitantly produced O_2. This study naturally motivates future investigations of how such an H_2 atmosphere maintains Europa's neutral H_2 torus and, in turn, the H_2^+ torus inferred here.

More broadly, this work demonstrates the utility of H_2 as a tracer species for surface-atmosphere-plasma coupling at icy moons in the outer Solar System. Unlike the bulk O_2 atmosphere—whose production, loss, and spatial structure are tightly coupled to, and in turn strongly influence, the local plasma environment—H_2 and H_2^+ pickup ions do not significantly perturb the large-scale plasma flow. This distinction enables self-consistent modeling of the extended neutral atmosphere within an ambient, effectively steady plasma background without requiring fully coupled plasma–neutral feedback, thereby avoiding the circular dependence that complicates hybrid plasma and magnetohydrodynamic simulations. Consequently, this approach facilitates robust constraints on atmospheric structure and escape using in-situ pickup-ion measurements and provides a complementary framework for interpreting the *Juno* flyby of Ganymede, as well as future observations of the icy Galilean satellites by *Europa Clipper* and *Juice*.

Appendix A: Radial Profiles

As discussed in Section 2, the formula of Summers et al. (1989), Equation 1, adopted by Szalay et al. (2024) to model Europa's neutral H_2 density profile assumes a constant radial speed, $v_{\parallel}$, throughout the atmosphere. Here we test the validity of this assumption by performing four simulations of H_2 atmospheres with *Harrah*, each using the same source rate ($\Phi_0 = 1.5$ kg/s) and Maxwellian energy distribution (Equation 2), but with different total reaction rates κ: (a) $\kappa = 0$ (i.e., no reactions), (b) 10^{-6} s^{-1}, (c) 10^{-5} s^{-1}, and (d) 10^{-4} s^{-1}. The resulting radial profiles are shown in Figures A1–A3, illustrating the normalized number density $n(r)/n_0$, the local atmospheric scale height $H(r)$ and depletion length scale $D(r)$, and the radial outflow speed $v_{\parallel}(r)$, respectively. In all runs, no

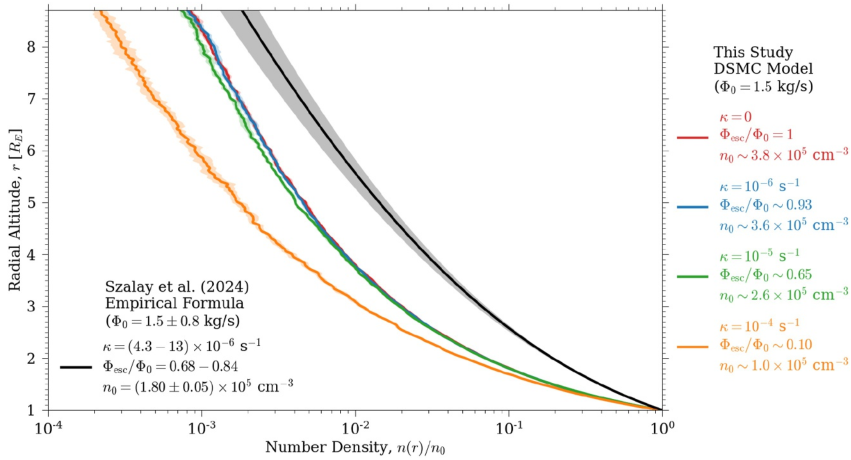

Figure A1. Comparison of normalized H_2 number density profiles $n(r)/n_0$ from simulations of H_2 atmospheres with reaction rates $\kappa = 0$ (red), 10^{-6} s^{-1} (blue), 10^{-5} s^{-1} (green), and 10^{-4} s^{-1} (orange). These results are compared to those inferred by Szalay et al. (2024) by solving Equation 1 (solid black lines). The shaded colored regions represent $\pm 1\sigma$ for the *Harrah* simulations and the uncertainties in the inference by Szalay et al. (2024). The red and blue curves closely overlap, reflecting the small differences between these cases.

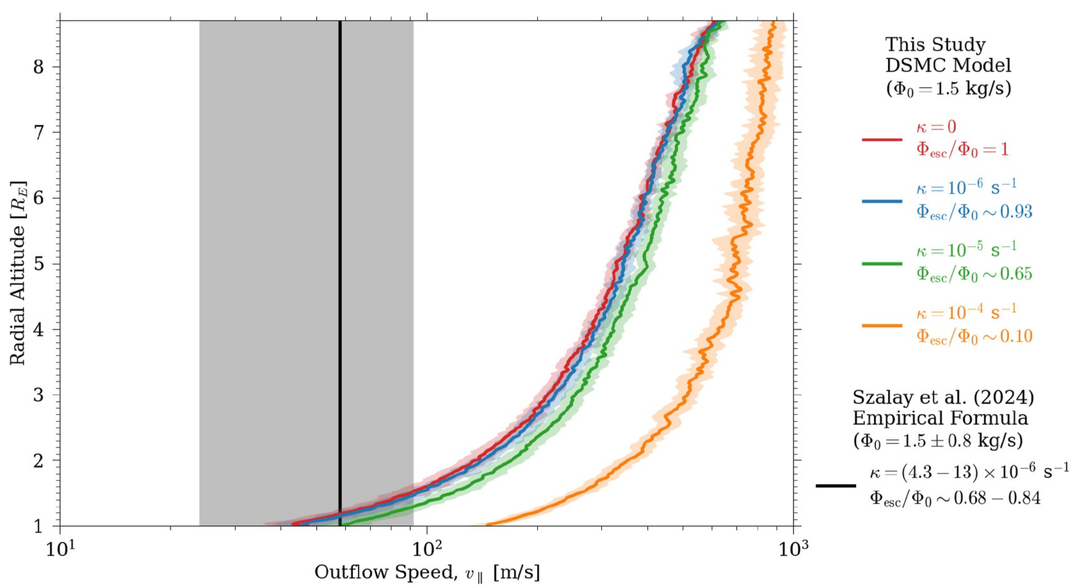

Figure A2. Comparison of mean radial outflow speeds $v_{\parallel}$ from simulations of H_2 atmospheres with reaction rates $\kappa = 0$ (red), 10^{-6} s^{-1} (blue), 10^{-5} s^{-1} (green), and 10^{-4} s^{-1} (orange). These results are compared to those inferred from Szalay et al. (2024) by solving Equation 1 in solid black lines. The shaded colored regions represent $\pm 1\sigma$ for the *Harrah* simulations and the error bars in the inference by Szalay et al. (2024).

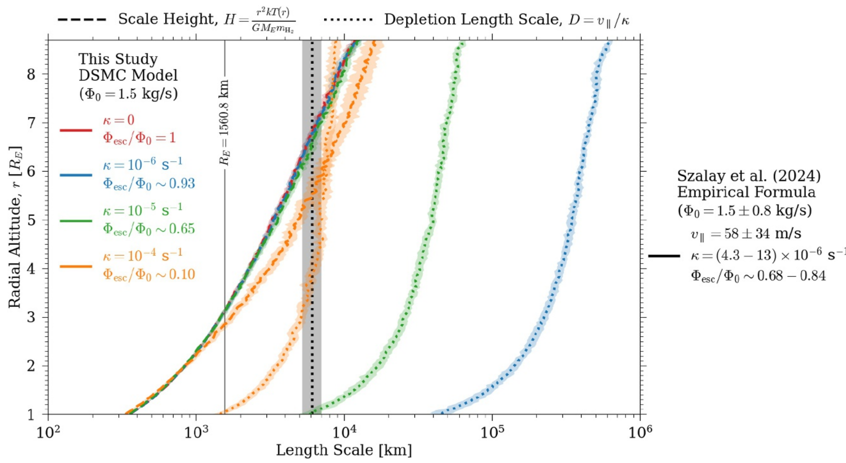

Figure A3. Comparison of local atmospheric scale heights H (dashed lines) and depletion length scales D (dotted lines) from simulations of H_2 atmospheres with reaction rates $\kappa = 0$ (red), 10^{-6} s^{-1} (blue), 10^{-5} s^{-1} (green), and 10^{-4} s^{-1} (orange). These results are compared to those inferred from Szalay et al. (2024) by solving Equation 1 in solid black lines. The shaded colored regions represent $\pm 1\sigma$ for the *Harrah* simulations and the error bars in the inference by Szalay et al. (2024).

prescription for $v_\parallel$ is imposed: it emerges naturally from the particle kinetics—in contrast to Equation 1, which requires a constant value, $D\kappa$, after fitting D and calculating κ. Atmospheric losses arise only from escape when $\kappa = 0$—hence escape rate $\Phi_{esc} = \Phi_0$—and both escape and reactions when $\kappa > 0$.

For $\kappa = 0$, 10^{-6}, and 10^{-5} s^{-1}, the resulting radial profiles of n, H, and $v_\parallel$ are virtually indistinguishable. Although D decreases as κ increases, D remains much larger than H for $\kappa \leq 10^{-5}$ s^{-1} (and is undefined when $\kappa = 0$), so atmospheric escape governs the radial decay of density. Only when $\kappa = 10^{-4}$ s^{-1} does D drop below H (at $\sim 6R_E$), producing a noticeably steeper decline in $n(r)$ and a substantially higher $v_\parallel(r)$ than in the lower-κ cases. Because the total reaction rates inferred by Szalay et al. (2024) from *Juno*/JADE measurements ($\kappa = (4.3–13) \times 10^{-6}$ s^{-1}) and the updated values presented in this study ($\kappa = (2.62–2.72) \times 10^{-6}$ s^{-1}) lie firmly in the regime where $D \gg H$, Europa's H_2 density profile is shaped by escape rather than by reactions.

As κ increases, Φ_{esc}/Φ_0 decreases: more particles are lost to reactions before they can escape, so only the high-velocity tail contributes to Φ_{esc}, thereby raising $v_\parallel$ with altitude. While the near-surface $v_\parallel$ for $\kappa \leq 10^{-5}$ remains within the uncertainties of the constant $v_\parallel$ inferred by Szalay et al. (2024), in all cases $v_\parallel$ increases by more than an order of magnitude by Europa's Hill sphere, reflecting that only the fastest H_2 reach such heights (corresponding to particles with initial speeds $\gtrsim 1.9$ km/s at the surface required to reach the Hill sphere).

Finally, because the DSMC-derived H increases with altitude, it surpasses the fixed D from Equation 1 at $\sim 5–7R_E$. Beyond these heights, $n(r)$ from a purely thermal atmosphere falls off more gradually than Equation 1 would predict for a "nonthermal" atmosphere.

These tests demonstrate that solving Equation 1 assuming a constant $v_\parallel$ in Europa's atmosphere where $D > H$ produces a misleading H_2 density profile. A self-consistent description of this rarefied atmosphere therefore requires a molecular-kinetics model such as *Harrah*.

Appendix B: Electron-Impact Reaction Rates

Figure B1 shows the electron-impact dissociation, ionization, dissociative-ionization, and total reaction rates for H_2 and O_2 used as inputs for the DSMC models (Section 3.2) and to convert neutral H_2 to H_2^+ PUIs (Section 3.3). These rates are derived by convolving the electron fluxes measured by *Juno*/JADE-E during the PJ45 flyby (Section 3.1) with electron-impact cross section distributions from the literature (Carberry Mogan et al., 2023; Cosby, 1993; Scarlett et al., 2018; Straub et al., 1996).

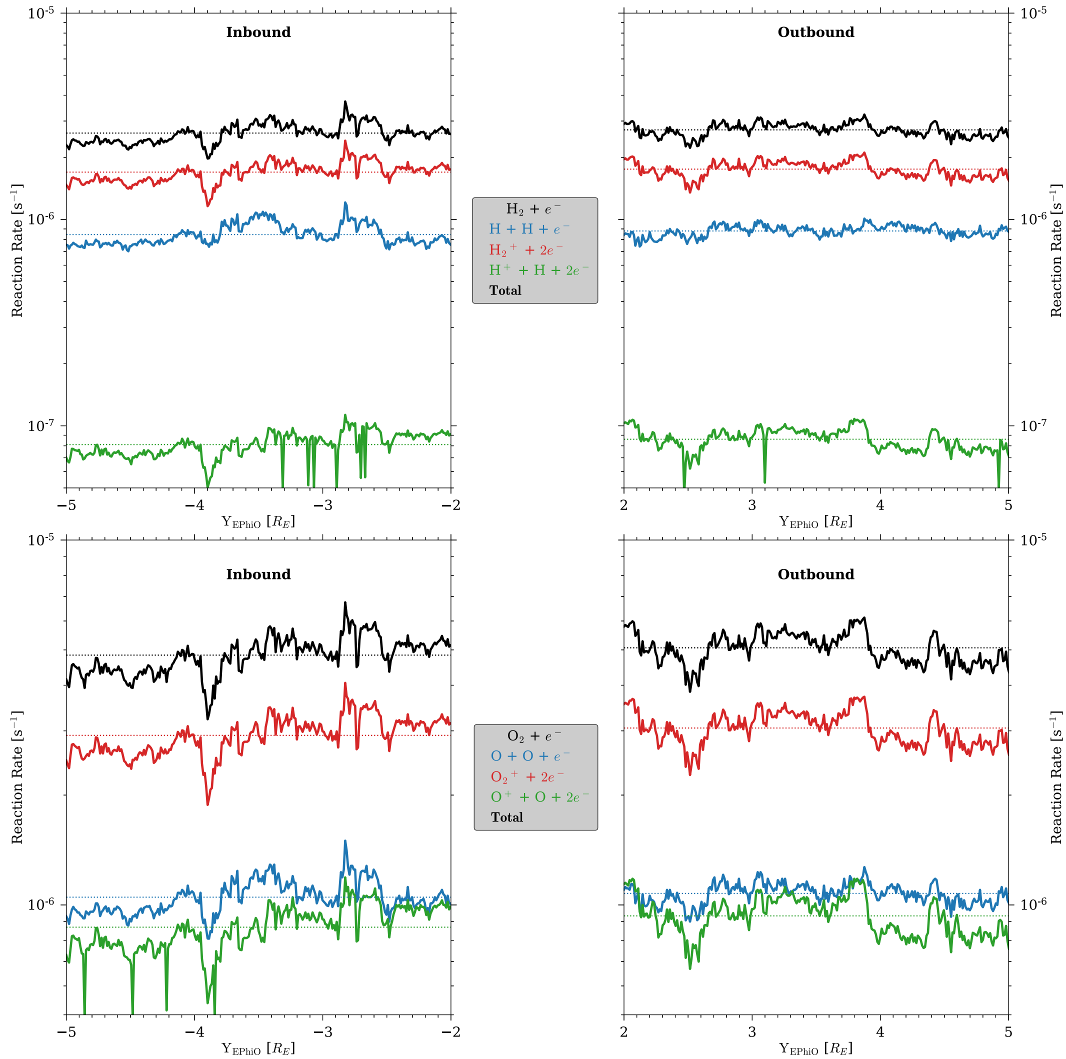

Figure B1. Electron-impact reaction rates for H_2 (top) and O_2 (bottom) along *Juno*'s PJ45 trajectory within $-5R_E \leq Y_{EPhiO} \leq -2R_E$ (left) and $2R_E \leq Y_{EPhiO} \leq 5R_E$ (right). Rates are computed by convolving in-situ electron fluxes from JADE-E (Ellis et al., 2026) with electron-impact collision cross sections (Carberry Mogan et al., 2023; Cosby, 1993; Scarlett et al., 2018; Straub et al., 1996). Blue, red, and green lines denote local dissociation, ionization, and dissociative-ionization rates, respectively, and the solid black lines are their sums. The colored dotted lines represent the average values, which are listed in Table 1.

Appendix C: Europa's Surface Temperature

Here we summarize the surface temperature distributions used to derive the globally averaged value ($T_0 \sim 98$ K) applied in the thermal H_2 source function (Equation 2 and Figure 2), as well as for the recycled H_2 and O_2 components. The temperatures were computed using the thermophysical model of Spencer et al. (1989), which accounts for variations in solar illumination, surface albedo, and thermal inertia across latitude, longitude, and orbital position. For each orbital longitude, the model outputs local temperature maps that were then area-weighted over the surface to obtain global means, which were subsequently averaged over Europa's orbital period to yield a uniform T_0. The results are shown in Figure C1: the top panel illustrates the evolution of Europa's minimum, global-average, and maximum surface temperatures as a function of orbital longitude, while the bottom panel presents the corresponding spatial temperature distribution at the time of Juno's PJ45 flyby (~1840 orbital local time). Implementing the minimum and maximum surface temperatures (~80 K–140 K) instead of 98 K would primarily affect the high-energy tail of the thermal H_2 distribution and thus the initial fraction capable of escaping. For example, the fraction of thermal H_2 with sufficient energy to reach Europa's Hill sphere increases

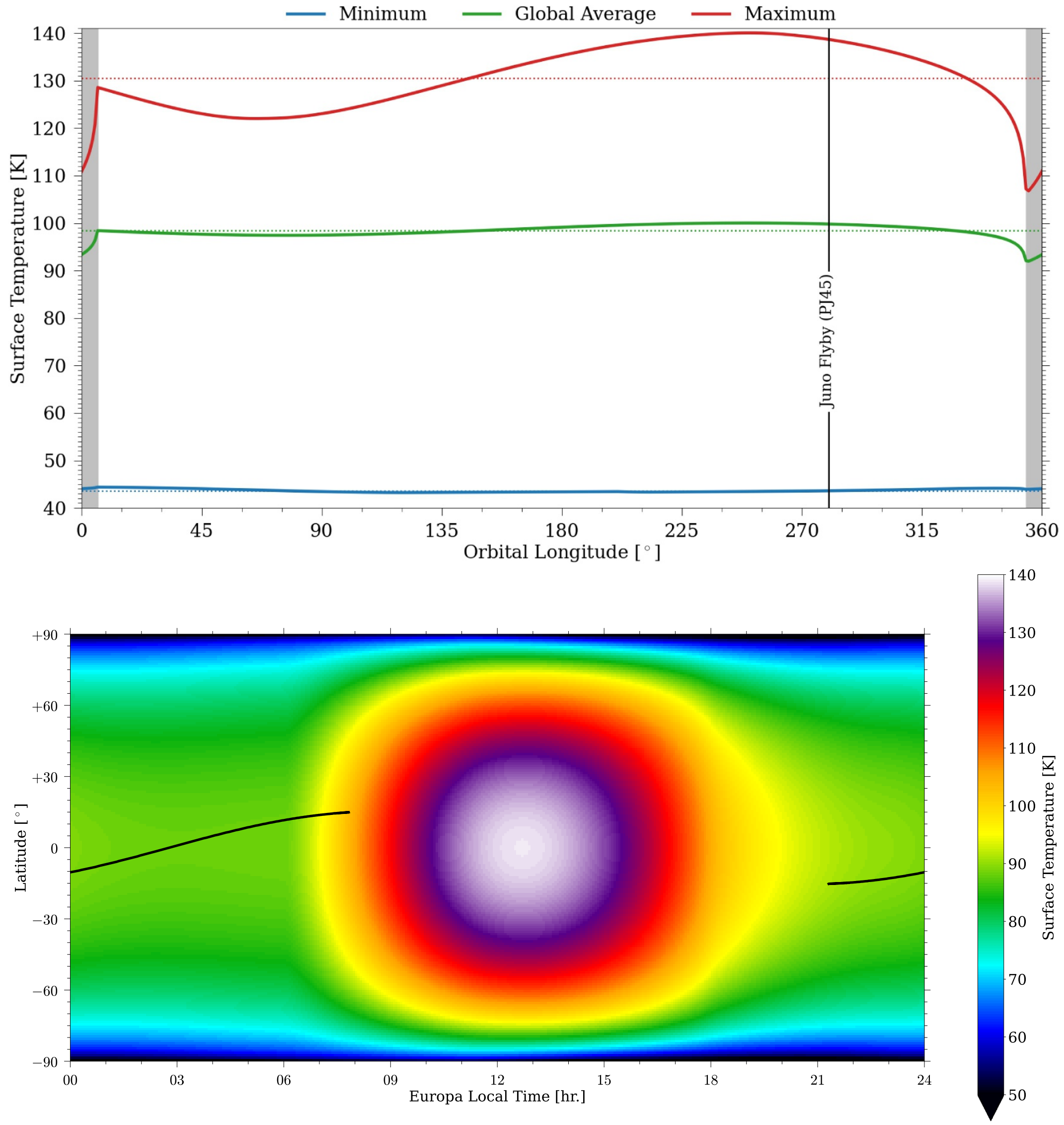

Figure C1. Top panel: Minimum (blue), global-average (green), and maximum (red) surface temperatures calculated as a function of Europa's orbital longitude. The horizontal dotted lines of the same colors represent the orbital-averaged values, the vertical black line represents the *Juno* PJ45 flyby, and the shaded regions indicate when Europa traverses Jupiter's shadow. Bottom panel: Europa's surface temperature as a function of local time (*x*-axis) and latitude (*y*-axis) during the *Juno* PJ45 flyby, with the black line representing the spacecraft's trajectory projected onto the surface over the interval considered (e.g., Figure 1).

from ∼3% at 80 K to ∼6% at 98 K and ∼18% at 140 K. The lowest temperatures are representative of the nightside surface, while the highest temperatures are confined to a limited subsolar region, thereby reducing their overall contribution to the globally averaged behavior.

Table D1
Photolytic Reaction Rates for H_2 in Europa's Atmosphere

Reactants	Products	Rate[a] [($\times10^{-9}$) s^{-1}]
H_2 + hν	$H_2^+ + e$	2.00–4.25
	H + H	1.77–4.03
	$H + H^*$	1.27–3.04
	$H + H^+ + e$	0.35–1.03
Total		**5.39–12.4**

Appendix D: Photolytic and Charge-Exchange Reaction Rates

Table D1 presents photolytic reaction rates for H_2 in Europa's atmosphere. These values are taken from Huebner and Mukherjee (2015), from solar minimum to maximum with the rates scaled to Europa's average distance from the Sun, 5.2 AU.

Table D2
Charge-Exchange Rates for H_2 *in Europa's Atmosphere*

Reactants	Products	Rate[a] [($\times 10^{-7}$) s^{-1}]
$H_2 + H^+$	$H_2^+ + H$	0.80–2.70
$H_2 + O^+$	$H_2^+ + O$	1.00–5.10
$H_2 + S^{++}$	$H_2^+ + S^+$	0.38–2.10
Total		**2.18–9.90**

Table D2 presents charge-exchange reaction rates for Europa's H_2 component with Jovian magnetospheric H^+, O^+, and S^{++} derived by Smith et al. (2019) according to a range of ion densities and temperatures inferred from *Galileo* data (Bagenal et al., 2015).

Appendix E: H_2^+ From Collisionless H_2 Atmospheres

Table E1 summarizes the best-fit H_2 source rates and H_2^+ background densities for both the purely thermal and nonthermal + thermal simulations of collisionless H_2 atmospheres according to the mean ionization rates and magnetospheric plasma speeds.

Figure E1 shows the plasma streamlines computed using the deflected-streamline model of Szalay et al. (2024) for the outbound leg of the PJ45 flyby.

Figure E2 presents the corresponding χ^2 analysis and comparison with the *Juno*/JADE measurements, as discussed in Section 4.1.1.

Figures E3–E8 illustrate the individual model–data comparisons for each assumed H_2 effective binding energy, E_b, considered in Section 4.1.2.

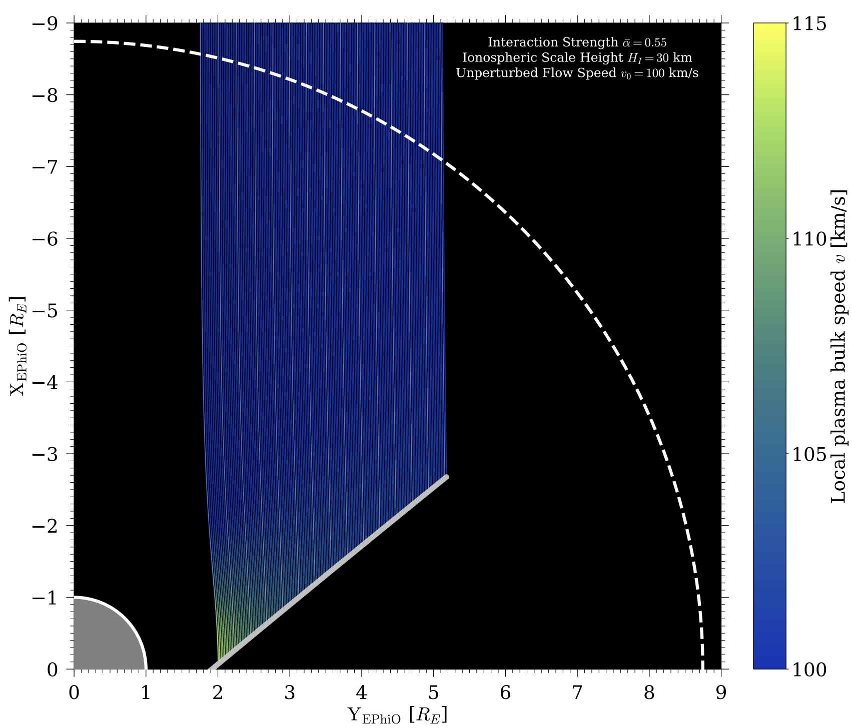

Figure E1. Plasma streamlines in $(X, Y)_{EPhiO}$ coordinates computed for *Juno*'s PJ45 flyby using the deflected-streamline model of Szalay et al. (2024).

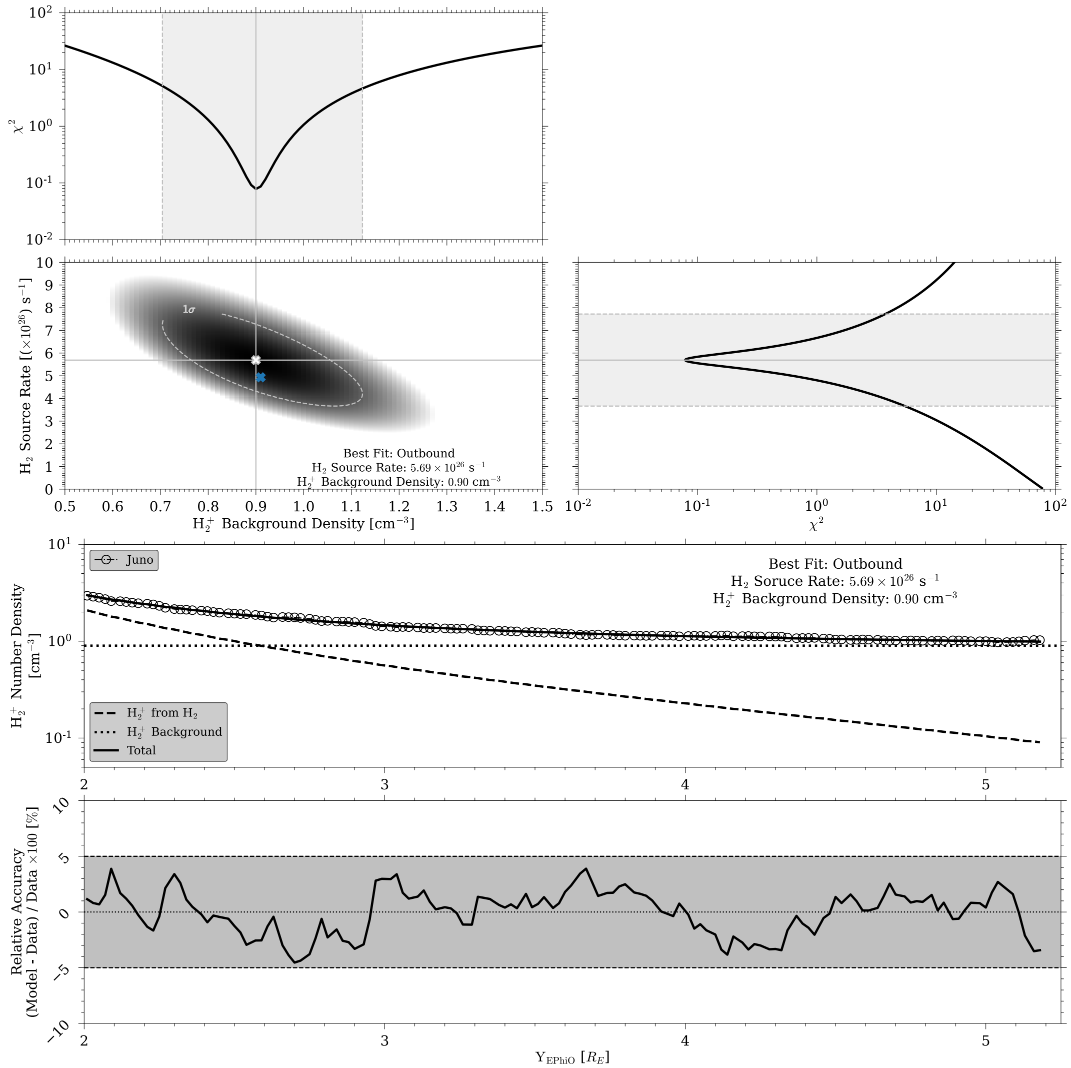

Figure E2. (Top panel) Same format as Figure 4: corner plot showing the χ^2 distribution used to determine the best-fit H_2 source rate and H_2^+ background density for the outbound leg of the PJ45 flyby using the deflected-streamline model. The blue cross represents the best-fit values from the straight-flow-vector approximation. (Bottom panel) Same format as Figure 5: comparison between observed and simulated H_2^+ pickup ion densities along the outbound leg of the PJ45 flyby, corresponding to the best-fit parameters shown in the top panel.

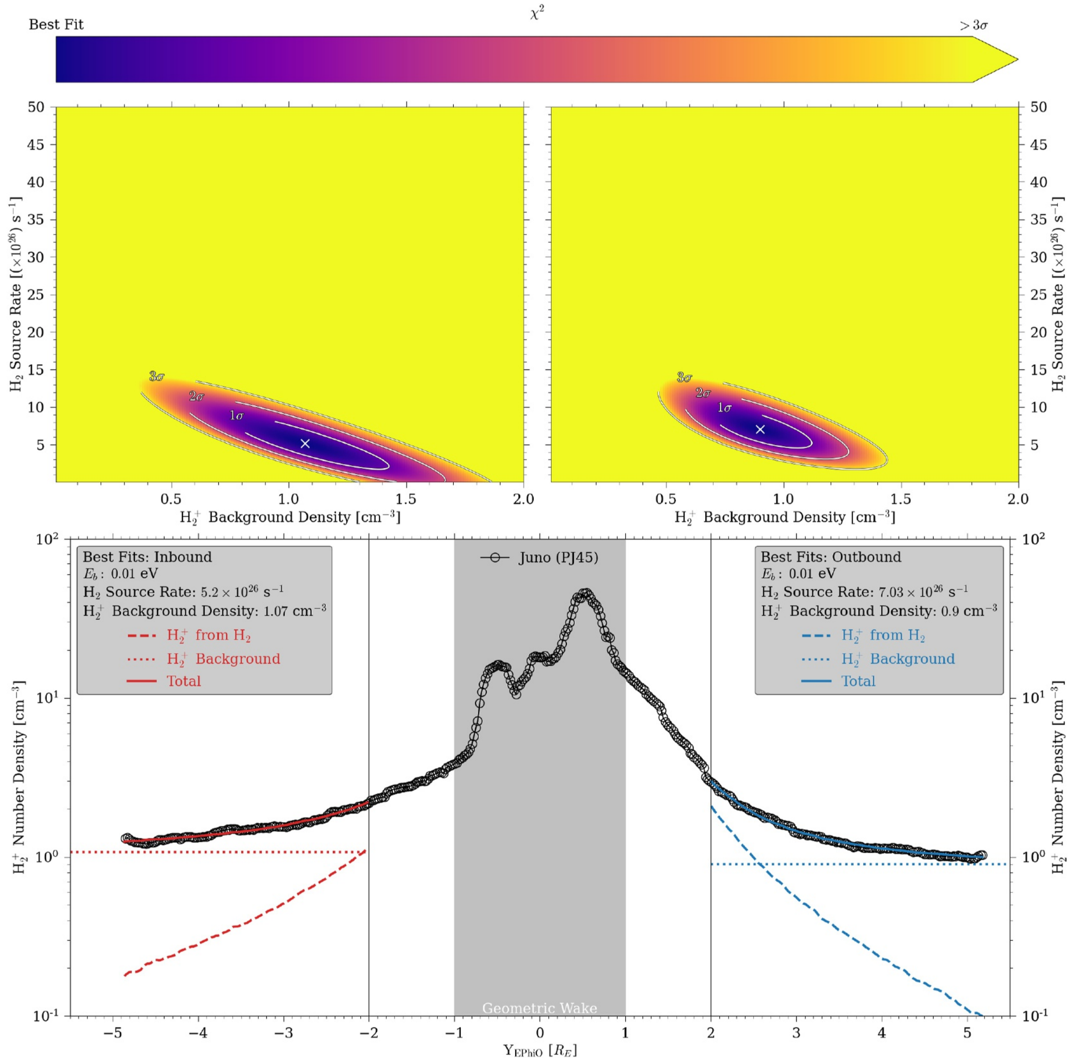

Figure E3. Top panels: χ^2 heatmap as a function of H_2^+ background densities (*x*-axis) and H_2 source rates (*y*-axis) for the inbound (left) and outbound (legs) of the PJ45 flyby. The best-fit values are indicated with a white X, which are surrounded by white contours representing 1σ, 2σ, and 3σ confidence intervals. Bottom panels: H_2^+ densities as a function of Y_{EPhiO}. H_2^+ pickup ions detected by Juno during PJ45 (solid black line and circles) are compared to those produced from simulated collisionless, nonthermal + thermal H_2 atmospheres with $E_b = 0.01$ eV (dashed lines), best-fit H_2^+ background densities (dotted lines), and their sum total (solid lines) for the inbound (red) and outbound (blue) legs of the flyby.

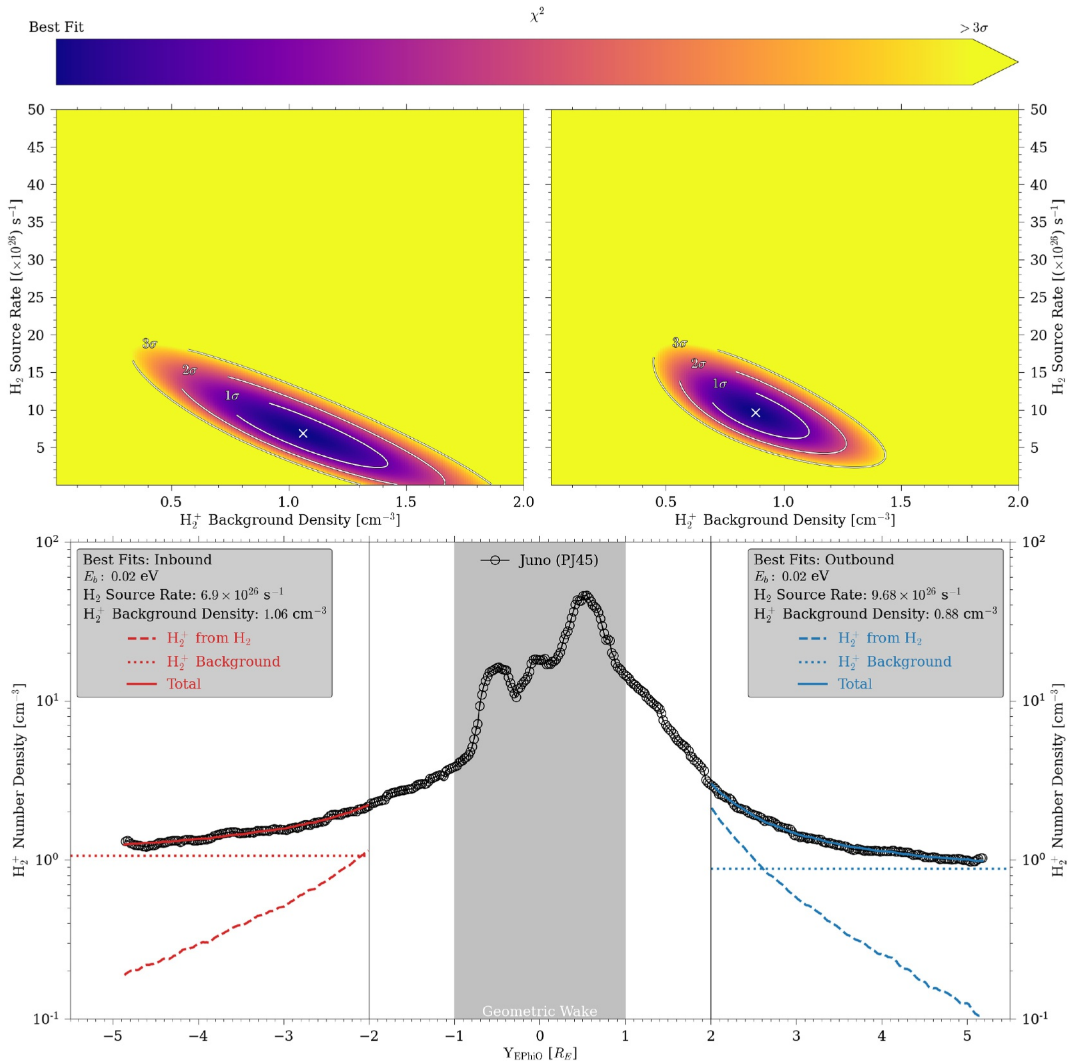

Figure E4. Same as Figure E3 but with $E_b = 0.02$ eV.

10.1029/2026JE009724

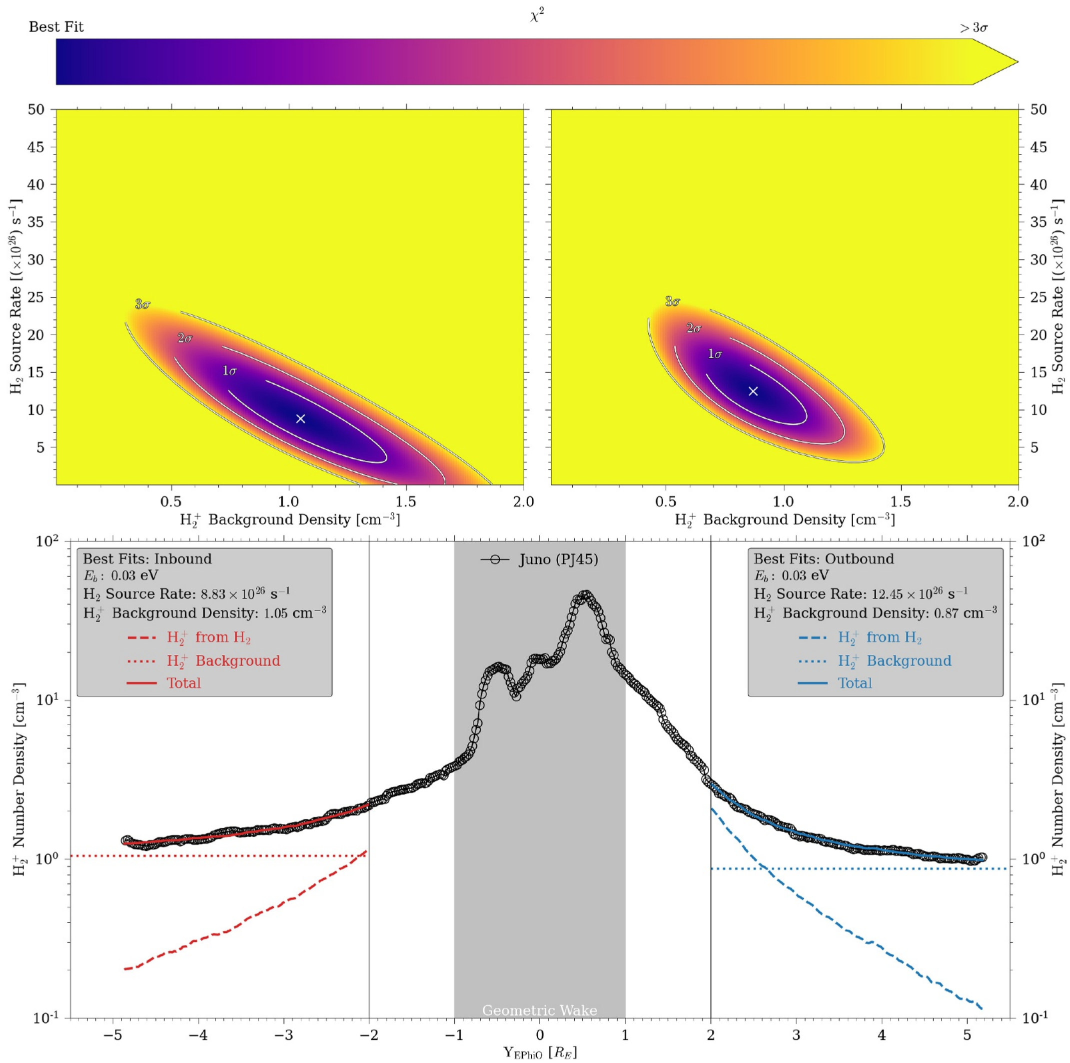

Figure E5. Same as Figures E3 and E4 but with $E_b = 0.03$ eV.

AGU ADVANCING EARTH AND SPACE SCIENCES

Journal of Geophysical Research: Planets

10.1029/2026JE009724

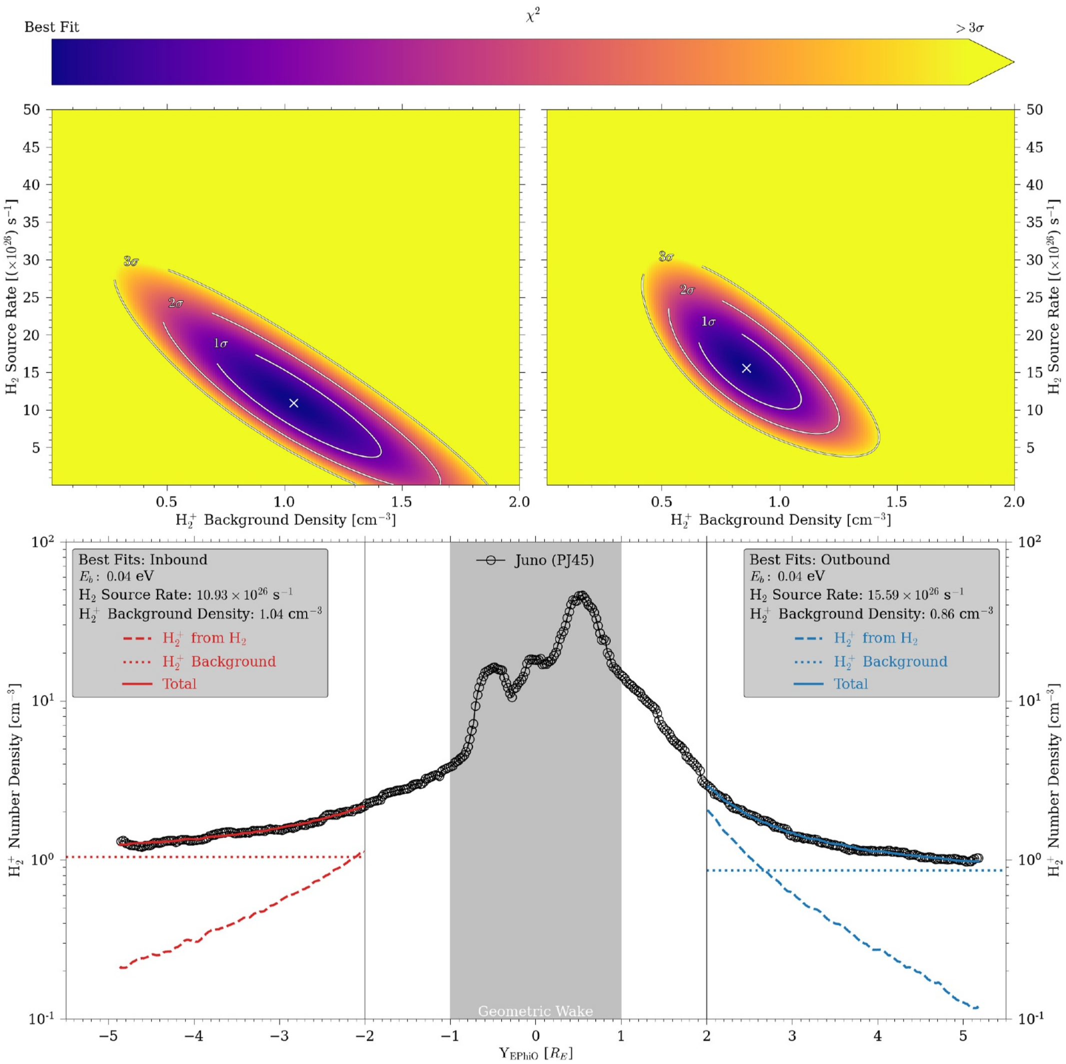

Figure E6. Same as Figures E3–E5 but with $E_b = 0.04$ eV.

Table E1
Best-Fit H_2 Source Rates and H_2^+ Background Densities for Simulations of Collisionless, Purely Thermal (Figures 4 and 5) and Nonthermal + Thermal (Figures 7–9) H_2 Atmospheres

		H_2 source rate [($\times10^{26}$) s^{-1}]		H_2^+ background density [cm^{-3}]	
		Inbound	Outbound	Inbound	Outbound
Purely Thermal H_2		3.63	4.93	1.09	0.91
Nonthermal + Thermal H_2	$E_b = 0.01$ eV	5.20	7.03	1.07	0.90
	$E_b = 0.02$ eV	6.90	9.68	1.06	0.88
	$E_b = 0.03$ eV	8.83	12.4	1.05	0.87
	$E_b = 0.04$ eV	10.9	15.6	1.04	0.86
	$E_b = 0.05$ eV	13.4	18.9	1.02	0.85
	$E_b = 0.06$ eV	15.5	22.4	1.02	0.84

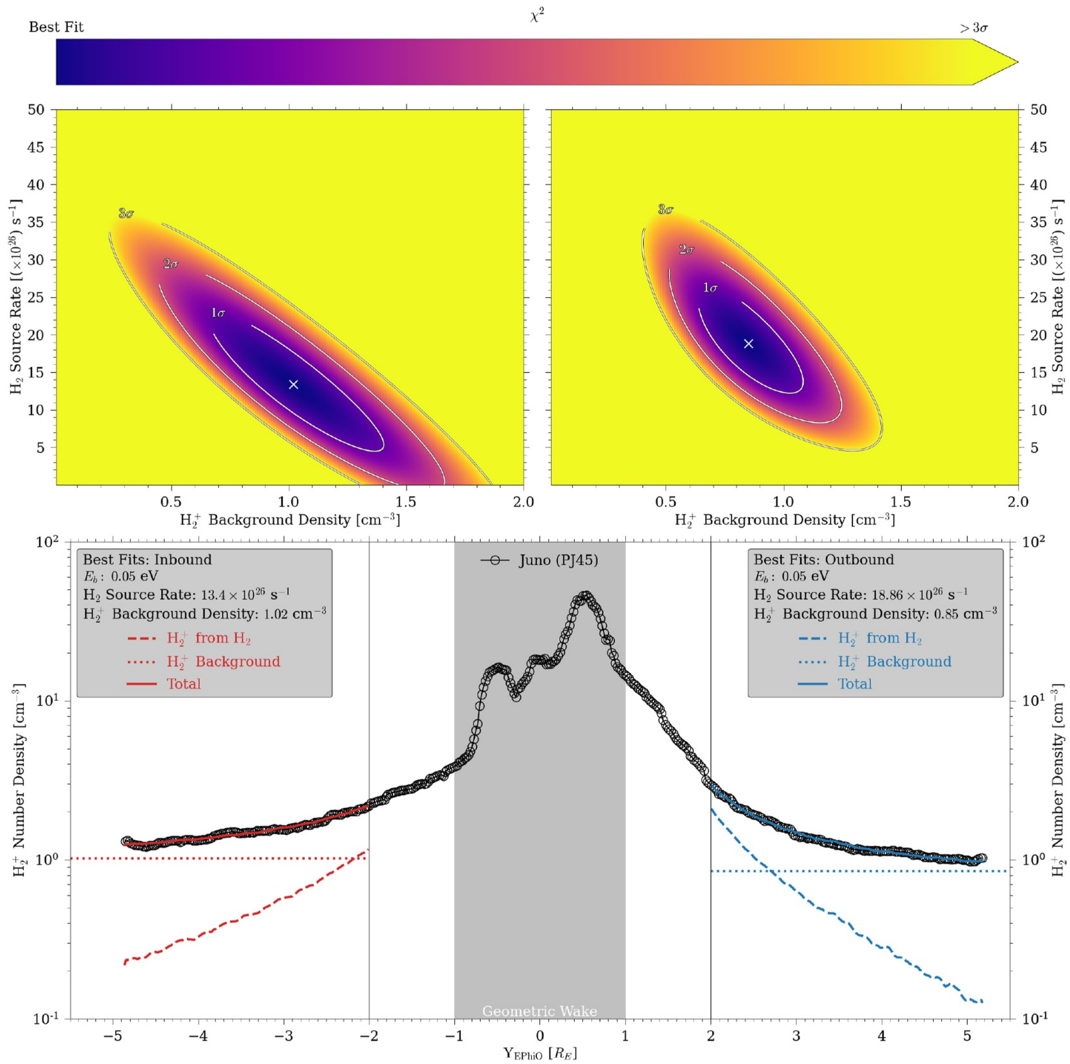

Figure E7. Same as Figures E3–E6 but with $E_b = 0.05$ eV.

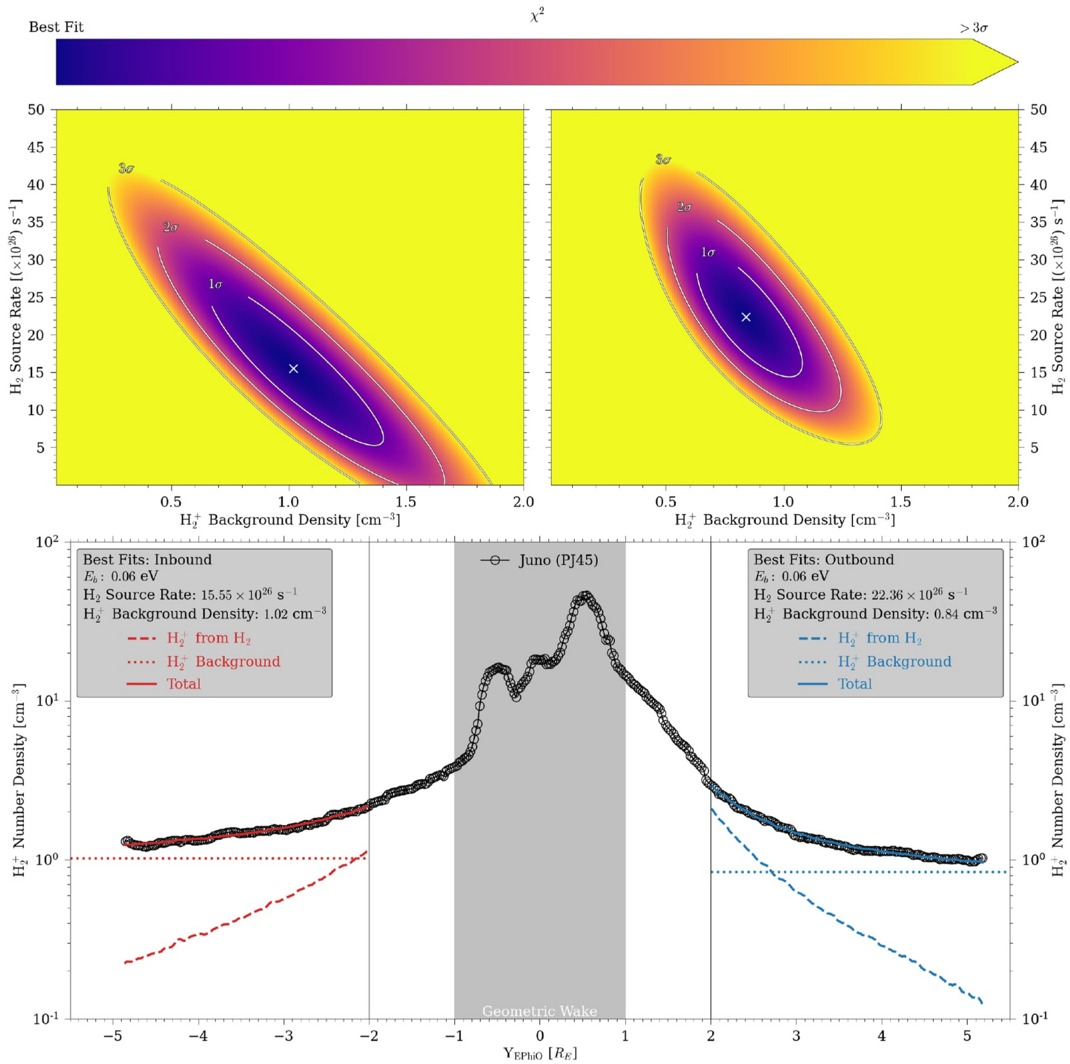

Figure E8. Same as Figures E3–E7 but with $E_b = 0.06$ eV.

Appendix F: H_2^+ From Collisional H_2+O_2+H+O Atmosphere with a Purely Thermal H_2 Component

Figure F1 compares the simulated H_2 number density profiles from collisional H_2+O_2+H+O atmospheres with a purely thermal H_2 component to those from the corresponding collisionless H_2 atmospheres for the inbound and outbound legs of the PJ45 flyby.

Figure F2 illustrates the effect of applying the best-fit H_2 source rates derived from collisionless H_2 atmospheres to collisional H_2+O_2+H+O atmospheres. Under these conditions, the χ^2 distributions used to determine the corresponding best-fit H_2^+ background densities shift toward lower values and become noticeably shallower (cf., Figure 4). This behavior reflects the degradation in fit quality caused by the collisional enhancement of H_2.

Figure F3 shows that allowing both the H_2 source rate and H_2^+ background density to vary yields revised best-fit parameters for collisional H_2+O_2+H+O atmospheres. DSMC simulations performed with these updated H_2 source rates (Figures F1 and 11), together with the corresponding best-fit H_2^+ background densities, restore agreement with the *Juno*/JADE data to within ±5% (Figure 10). Finally, following these simulations, an

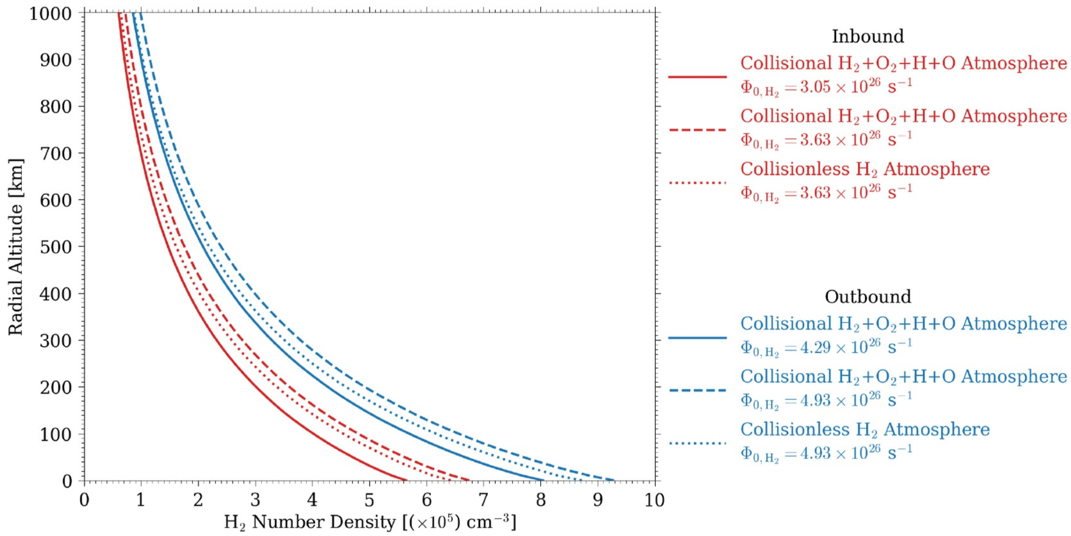

(a) Radial altitude in km, extending to 1000 km.

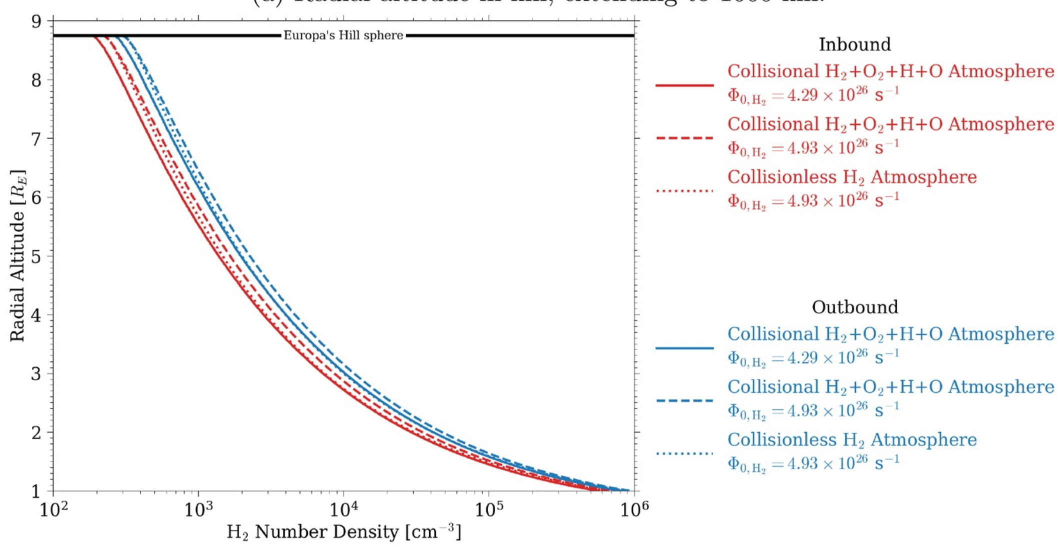

(b) Radial altitude in units of R_E, extending to Europa's Hill sphere.

Figure F1. Simulated H_2 number density profiles resulting from prescribed H_2 source rates (Φ_{0,H_2}) in collisional H_2+O_2+H+O atmospheres (solid, dashed) and collisionless H_2 atmospheres (dotted) for the inbound (red) and outbound (blue) legs of the PJ45 flyby.

additional χ^2 analysis was performed to assess whether further improvement in the best-fit parameters could be achieved. As noted in Section 4, for the outbound leg of the PJ45 flyby this analysis returned the same best-fit H_2 source rate and H_2^+ background density as previously obtained: 4.29×10^{26} s^{-1} and 0.91 cm^{-3}, respectively. Figure F4 illustrates the revised best-fit parameters for the outbound leg: an H_2 source rate of 3.17×10^{26} s^{-1} and an H_2^+ background density of 1.10 cm^{-3}. An additional DSMC simulation was not performed using this revised H_2 source rate, as the improvement relative to the adopted solution is negligible.

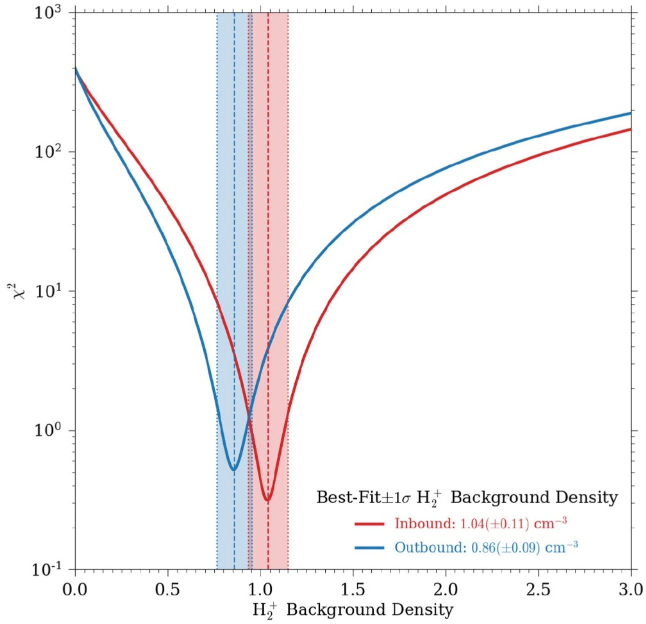

Figure F2. χ^2 distributions (y-axis, solid curves) used to determine the best-fit H_2^+ background densities (x-axis, vertical dashed lines) for the inbound (red) and outbound (blue) legs of the PJ45 flyby in collisional H_2+O_2+H+O atmospheres. The H_2 source rates are set to the best-fit values obtained from the corresponding collisionless simulations (Table E1). Shaded regions bounded by vertical dotted lines indicate the $\pm 1\sigma$ confidence intervals.

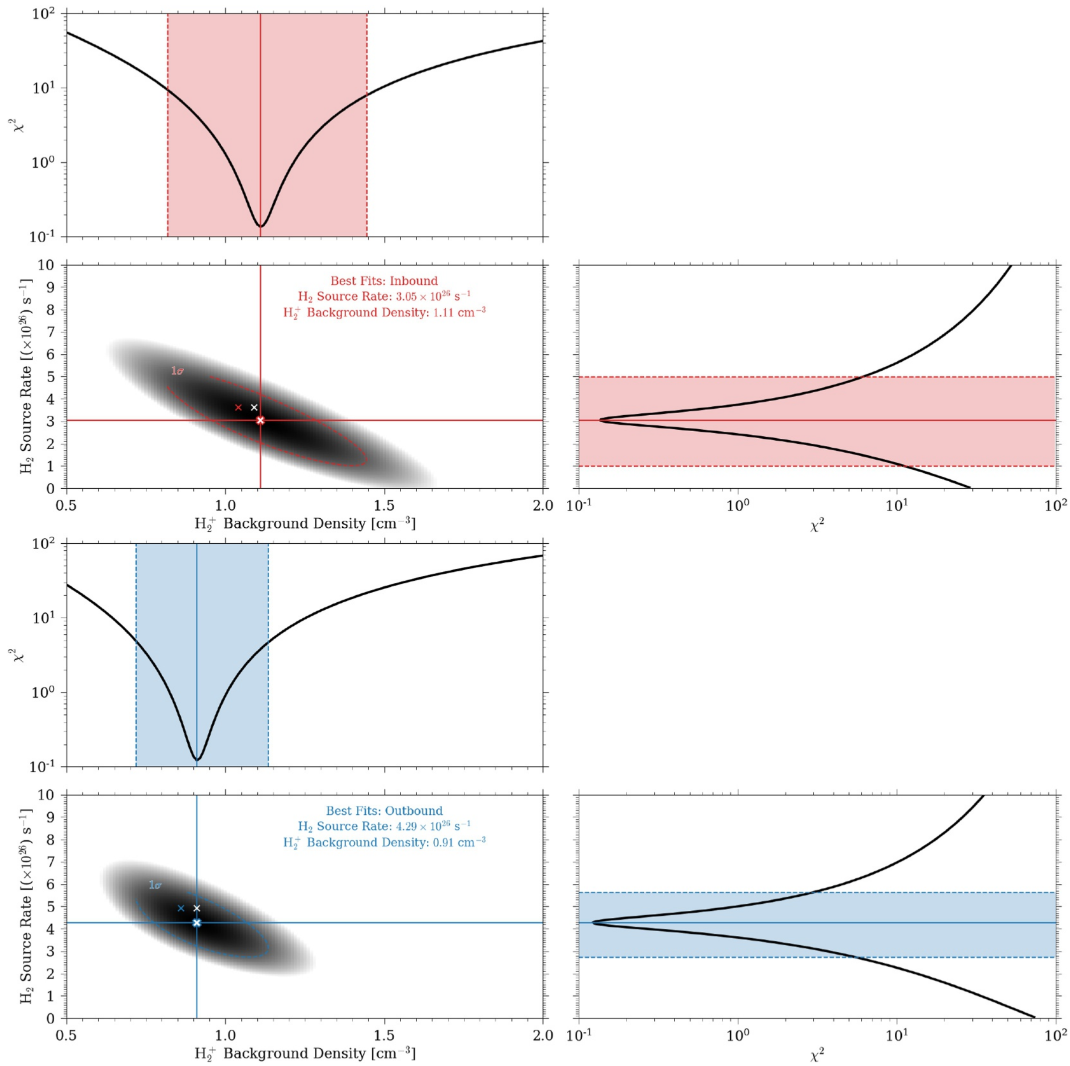

Figure F3. Corner plots showing the χ^2 distributions used to determine the best-fit H_2 source rate and H_2^+ background density for the inbound (top, red) and outbound (bottom, blue) legs of the *Juno* PJ45 flyby. Same format as Figure 4 but for collisional H_2+O_2+H+O atmospheres. In the central panels, the original best-fit values from the collisionless H_2 simulation are illustrated by white crosses, while red or blue crosses denote the best-fit H_2^+ background densities obtained for the collisional H_2+O_2+H+O atmospheres when the H_2 source rate is held fixed.

Journal of Geophysical Research: Planets 10.1029/2026JE009724

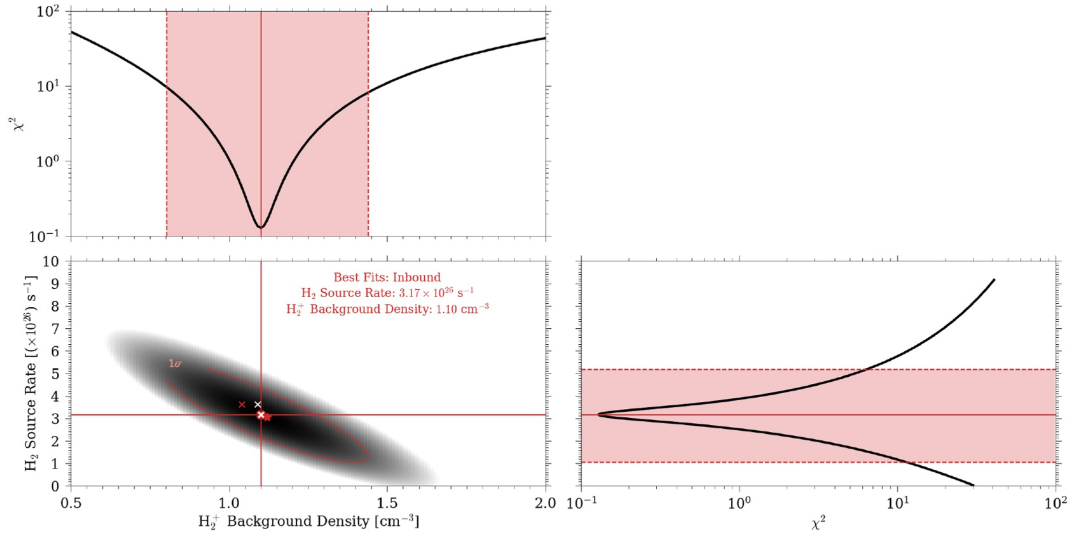

Figure F4. Corner plot showing the χ^2 distribution used to determine the best-fit H_2 source rate and H_2^+ background density for the inbound leg of the *Juno* PJ45 flyby. In the central panel, the white cross marks the best-fit parameters obtained from the collisionless H_2 simulation; the red cross denotes the best-fit H_2^+ background densities obtained for the collisional H_2+O_2+H+O atmospheres when the H_2 source rate is held fixed; the red star is the best-fit parameter combination corresponding to the subsequent DSMC simulation when both the H_2 source rate and H_2^+ background densities were allowed to vary; and the white cross overlaid with a red cross indicates the best-fit parameters that would be obtained from a subsequent iteration of the χ^2 analysis.

Appendix G: H_2^+ From Collisional H_2+O_2+H+O Atmosphere With a Nonthermal + Thermal H_2 Component

Figure G1 compares the total number density profiles for H_2 in collisionless H_2 and collisional H_2+O_2+H+O atmospheres across the explored range of H_2 effective binding energies, E_b. In contrast to the collisionless simulations, where increasing E_b produces lower near-surface densities and larger scale heights (Figure 9a), the inclusion of interspecies collisions leads to a net increase in the total H_2 density and more gradual profiles with increasing E_b. This behavior reflects the collisional coupling introduced by the accompanying increase in O_2

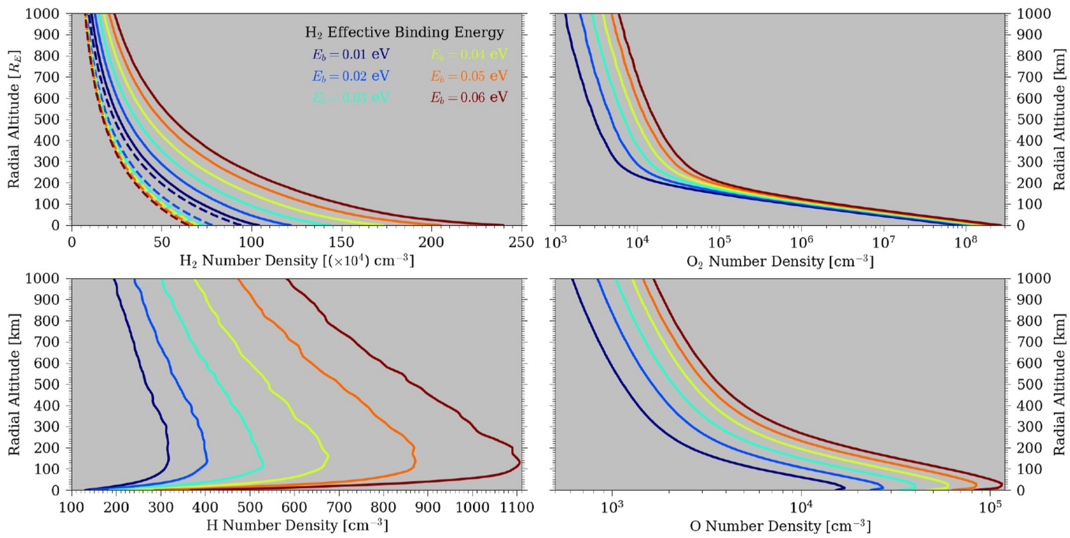

Figure G1. Density profiles within collisional H_2+O_2+H+O atmospheres for different assumed H_2 effective binding energies, E_b. Colors correspond to increasing E_b from 0.01 to 0.06 eV for H_2 (top left), O_2 (top right), H (bottom left), O (bottom right). In the top left panel, H_2 density profiles from the corresponding collisionless simulations are shown for comparison (dashed lines).

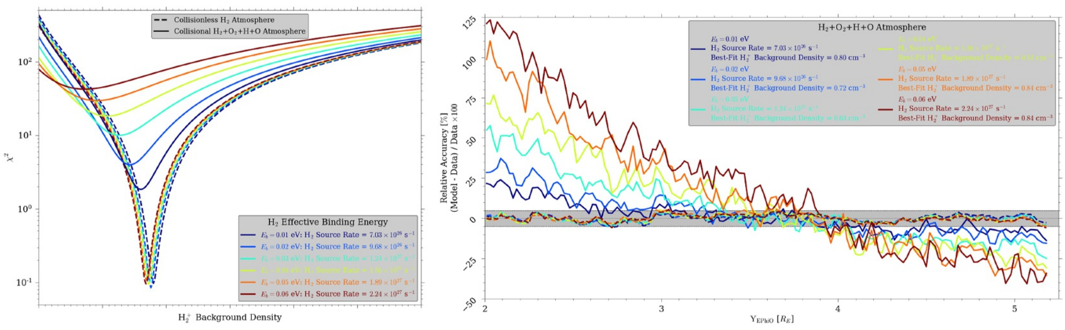

Figure G2. Left panel: χ^2 distributions for the H_2^+ background density for the collisional H_2+O_2+H+O atmospheres when the best-fit H_2 source rates from the collisionless simulations (Table E1) are held fixed for the outbound leg of the PJ45 flyby. Right panel: Relative accuracy between modeled and observed H_2^+ densities for collisional H_2+O_2+H+O atmospheres that include a nonthermal H_2 component on the outbound leg, for different assumed H_2 surface binding energies E_b (colors). In both panels, the results from the collisionless simulations are also shown (from Figures 7 and 8; dashed lines).

production: assuming a 2:1 stoichiometric ratio, higher H_2 source rates imply proportionally larger O_2 source rates, which enhance O_2 densities (also shown in Figure G1) and increase H_2+O_2 collision frequencies. As a result, a larger fraction of initially nonthermal H_2 molecules is redirected back to the surface, where they thermalize, increasing the overall H_2 population. The associated increases in the densities of dissociation products (H and O; see also Figure G1) are nonlinear, reflecting the coupled effects of enhanced parent-molecule densities and collision-driven enhancement of their own densities.

Figure G2 illustrates the effect of including interspecies collisions in atmospheres that contain both thermal and nonthermal H_2. When the H_2 source rates derived from the collisionless simulations are held fixed (Table E1), the

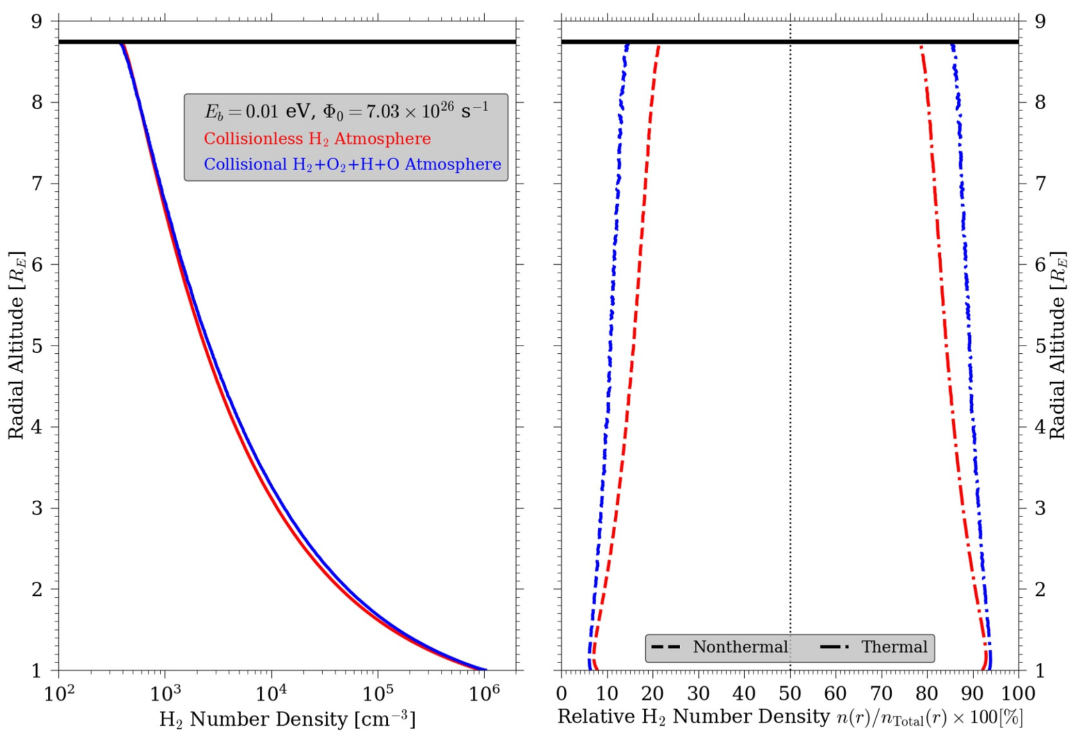

Figure G3. Left panel: A comparison between H_2 density profiles from simulated collisionless H_2 (red) and collisional H_2+O_2+H+O (blue) atmospheres with an H_2 effective binding energy $E_b = 0.01$ eV and source rate $\Phi_0 = 7.03 \times 10^{26}$ s^{-1}. Right panel: The nonthermal (dashed) and thermal (dash-dotted) components of the total H_2 densities presented in the left panel.

10.1029/2026JE009724

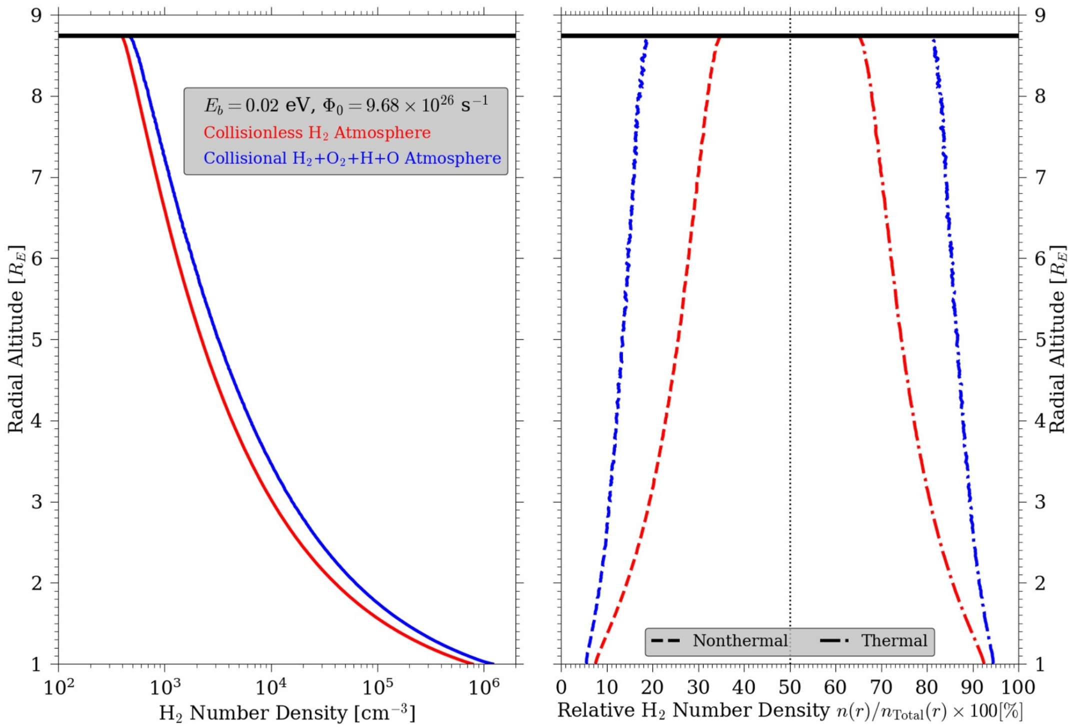

Figure G4. Same as Figure G3 but with $E_b = 0.02$ eV and $\Phi_0 = 9.68 \times 10^{26}$ s^{-1}.

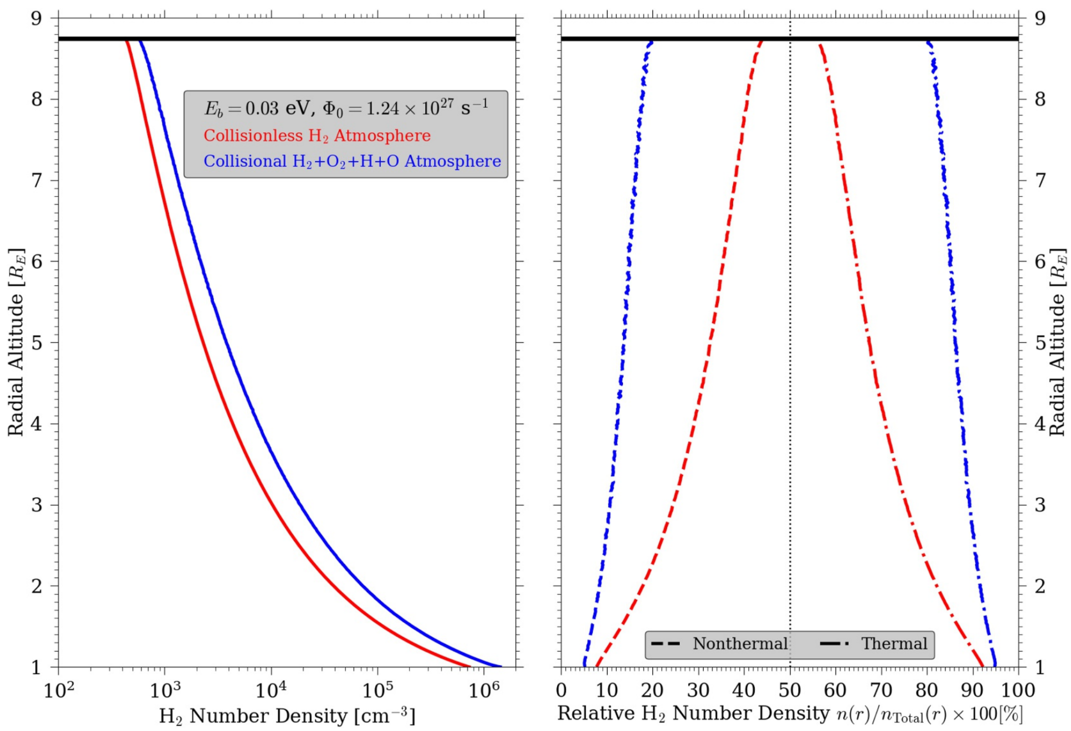

Figure G5. Same as Figures G3 and G4 but with $E_b = 0.03$ eV and $\Phi_0 = 1.24 \times 10^{27}$ s^{-1}.

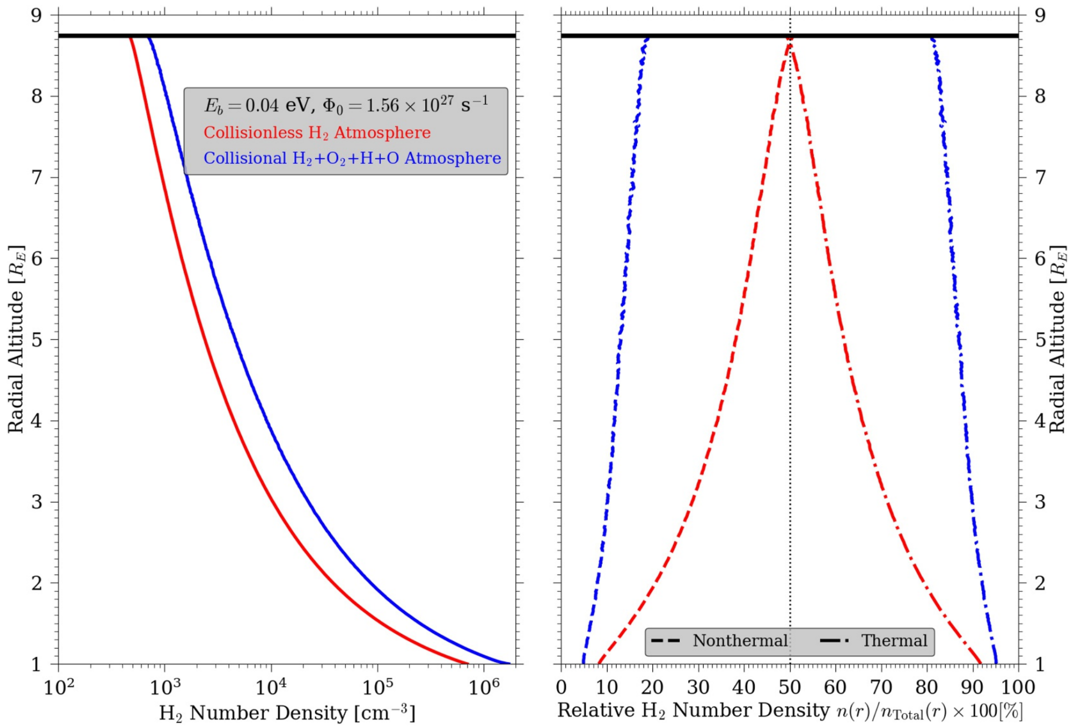

Figure G6. Same as Figures G3–G5 but with $E_b = 0.04$ eV and $\Phi_0 = 1.56 \times 10^{27}$ s^{-1}.

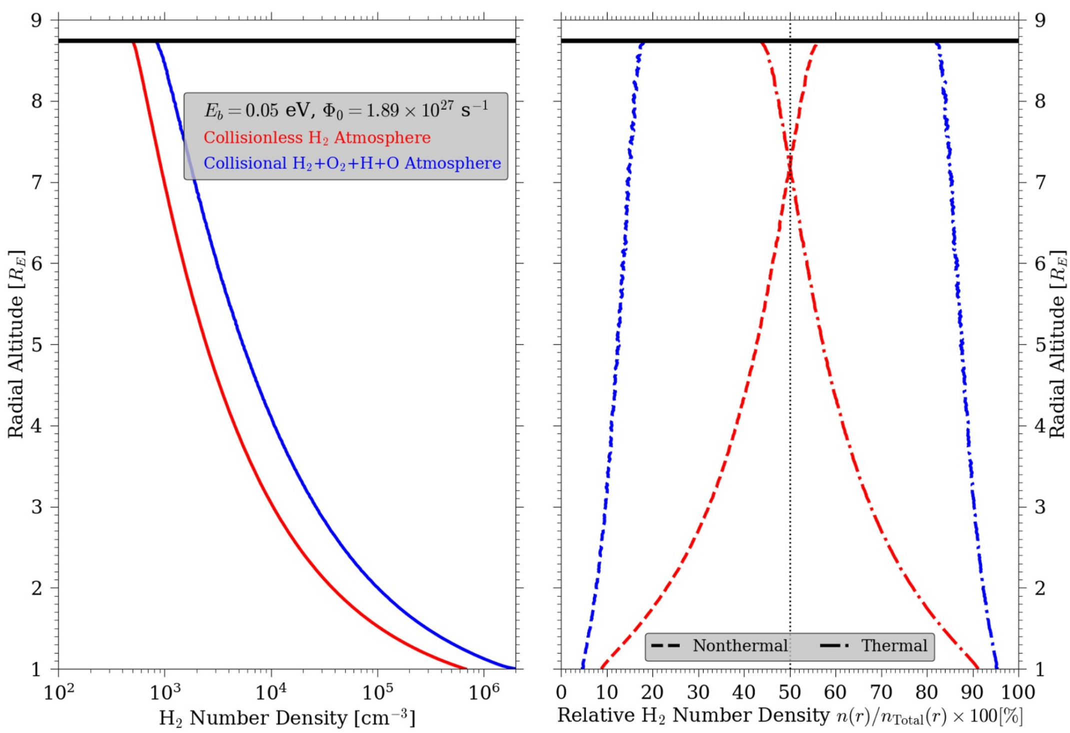

Figure G7. Same as Figures G3–G6 but with $E_b = 0.05$ eV and $\Phi_0 = 1.89 \times 10^{27}$ s^{-1}.

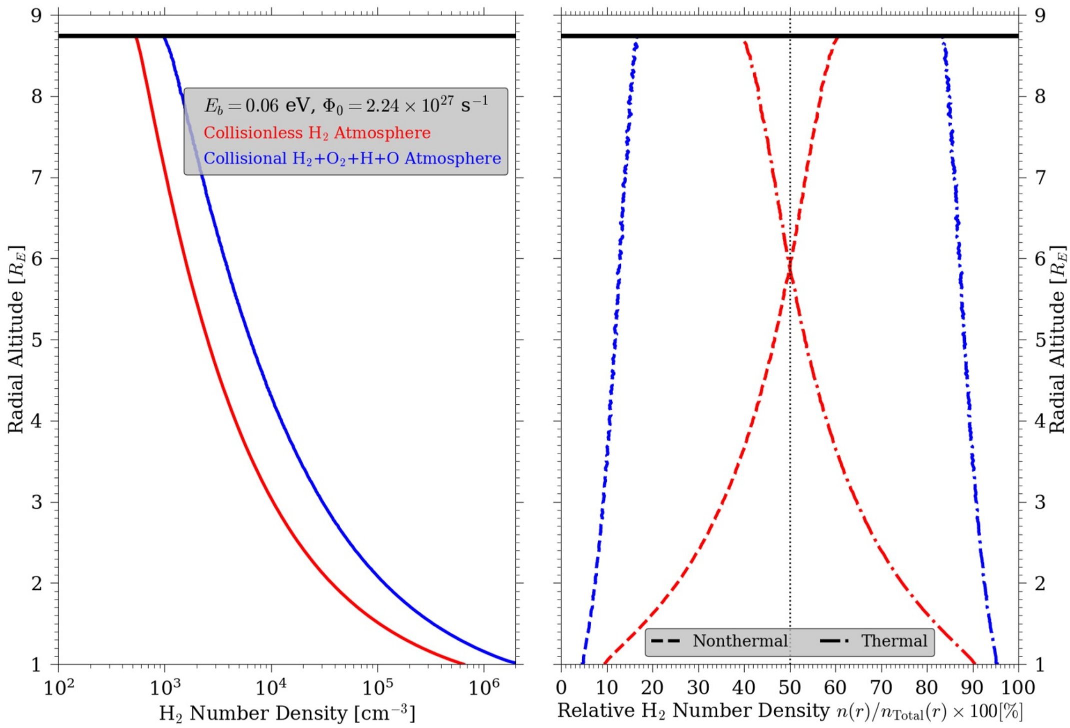

Figure G8. Same as Figures G3–G7 but with $E_b = 0.06$ eV and $\Phi_0 = 2.24 \times 10^{27}$ s^{-1}.

resulting χ^2 distributions become significantly shallower (left panel) and the agreement with the *Juno*/JADE H_2^+ measurements degrades substantially (right panel), particularly for larger E_b. Although formally lower best-fit H_2^+ background densities can be identified (left panel), these solutions correspond to poor agreement with the data across the outbound leg of the flyby (right panel). This behavior again reflects the nonlinear feedback introduced by collisions: as nonthermal H_2 molecules are increasingly redirected back to the surface via collisions with O_2, the resulting enhancement of the total H_2 density leads to an overprediction of H_2^+ along the *Juno* trajectory. Achieving a new self-consistent optimum (e.g., F.3) would therefore require reducing the H_2 source rate and re-adjusting the H_2^+ background density for each assumed value of E_b. However, a reduced H_2 source rate implies a lower O_2 density, which weakens the collisional coupling; as a result, the next iteration would likely underpredict the observed H_2^+, requiring a subsequent iteration with a larger H_2 source rate. This back-and-forth adjustment would necessitate multiple successive iterations, each involving a full multispecies DSMC simulation. Such an exploration is computationally prohibitive and, given the excellent agreement obtained with purely thermal H_2 atmospheres, not warranted by the data.

Figures G3–G8 compare the total H_2 number density profiles (left panels) and the relative contributions of the thermal and nonthermal components (right panels) for collisional H_2+O_2+H+O atmospheres with effective binding energies E_b ranging from 0.01 to 0.06 eV. For all E_b values, the inclusion of interspecies collisions increases the total H_2 density relative to the corresponding collisionless case, with the enhancement becoming more pronounced as E_b increases. This increase reflects the progressive thermalization of initially nonthermal H_2 through collisions with O_2, which redirects a growing fraction of H_2 molecules back toward the surface. As a result, although nonthermal sources are present in all cases, the total H_2 population remains dominated by the thermal component out to the Hill sphere, with the nonthermal fraction generally remaining below $\sim 20\%$.

Conflict of Interest

The authors declare no conflicts of interest relevant to this study.

Acknowledgments

S.R.C.M. acknowledges support from the Vetenskapsrådet Starting Grant (2025-04693); S.R.C.M., A.R.P., and L.L. acknowledge support from NASA Solar System Workings Grants 80NSSC21K0152 and 80NSSC22K0097, as well as from Precursor Science Investigations for Europa Grant 80NSSC25K7626; and S.R.C.M., L.L., and J.R.S acknowledge support from NASA New Frontiers Data Analysis Program Grant 80NSSC26K0186. Finally, the simulations presented in this study were enabled by resources provided by the National Academic Infrastructure for Supercomputing in Sweden (NAISS) through project NAISS 2025/22-1355.

Availability Statement

The data sets, simulation outputs, and Python scripts required to generate the figures presented in this study are publicly available through Carberry Mogan (2026).

References

Acharyya, K. (2014). Laboratory study of sticking and desorption of H_2 and its significance in the chemical evolution of dense interstellar medium. *Monthly Notices of the Royal Astronomical Society*, *443*(2), 1301–1309. https://doi.org/10.1093/mnras/stu1219

Addison, P., Haynes, C. M., Stahl, A. M., Liuzzo, L., & Simon, S. (2024). Magnetic signatures of the interaction between Europa and Jupiter's magnetosphere during the Juno flyby. *Geophysical Research Letters*, *51*(2), e2023GL106810. https://doi.org/10.1029/2023gl106810

Addison, P., Liuzzo, L., & Simon, S. (2022). Effect of the magnetospheric plasma interaction and solar illumination on ion sputtering of Europa's surface ice. *Journal of Geophysical Research: Space Physics*, *127*(2), e2021JA030136. https://doi.org/10.1029/2021ja030136

Bagenal, F. (1994). Empirical model of the Io plasma torus: Voyager measurements. *Journal of Geophysical Research*, *99*(A6), 11043–11062. https://doi.org/10.1029/93ja02908

Bagenal, F., Sidrow, E., Wilson, R. J., Cassidy, T. A., Dols, V., Crary, F. J., et al. (2015). Plasma conditions at Europa's orbit. *Icarus*, *261*, 1–13. https://doi.org/10.1016/j.icarus.2015.07.036

Beth, A., Galand, M., Jia, X., & Leblanc, F. (2025). Ion-neutral chemistry at icy moons: The case of Ganymede. *Monthly Notices of the Royal Astronomical Society*, *544*(1), 95–112. https://doi.org/10.1093/mnras/staf1668

Beth, A., Galand, M., Modolo, R., Jia, X., Leblanc, F., & Huybrighs, H. L. F. (2025). Ionosphere of Ganymede: Galileo observations versus test particle simulation. *Monthly Notices of the Royal Astronomical Society*, *538*(4), 2483–2507. https://doi.org/10.1093/mnras/staf313

Bird, G. A. (1994). *Molecular gas dynamics and the direct simulation of gas flows*. Oxford University Press.

Bolton, S. J., Lunine, J., Stevenson, D., Connerney, J. E. P., Levin, S., Owen, T. C., et al. (2017). The Juno mission. *Space Science Reviews*, *213*, 5–37.

Boring, J. W., Johnson, R. E., Reimann, C. T., Garret, J. W., Brown, W. L., & Marcantonio, K. J. (1983). Ion-induced chemistry in condensed gas solids. *Nuclear Instruments and Methods in Physics Research*, *218*(1–3), 707–711. https://doi.org/10.1016/0167-5087(83)91070-0

Carberry Mogan, S. R. (2026). Data supporting: Reconstructing Europa's atmosphere from H_2 pickup ions detected during the Juno PJ45 flyby. https://doi.org/10.5281/zenodo.20506426

Carberry Mogan, S. R., Johnson, R. E., Vorburger, A., & Roth, L. (2023). Electron impact ionization in the icy Galilean satellites' atmospheres. *The European Physical Journal D*, *77*(2), 1–9. https://doi.org/10.1140/epjd/s10053-023-00606-8

Carberry Mogan, S. R., Liuzzo, L. L., & Poppe, A. R. (2024). The influence of non-thermal collisions in Europa's atmosphere. *Geophysical Research Letters*, *51*(20), e2024GL109534. https://doi.org/10.1029/2024GL109534

Carberry Mogan, S. R., Moore, L. E., Liuzzo, L., & Poppe, A. R. (2025). A direct simulation Monte Carlo–driven photochemical model of Callisto's ionosphere. *The Planetary Science Journal*, *6*(5), 106. https://doi.org/10.3847/psj/adc5eb

Carberry Mogan, S. R., Tucker, O. J., & Johnson, R. E. (2021). The influence of upper boundary conditions on molecular kinetic atmospheric escape simulations. *Planetary and Space Science*, *205*, 105302. https://doi.org/10.1016/j.pss.2021.105302

Carberry Mogan, S. R., Tucker, O. J., Johnson, R. E., Roth, L., Alday, J., Vorburger, V., et al. (2022). Callisto's atmosphere: First evidence for H_2 and constrains on H_2O. *Journal of Geophysical Research: Planets*, *127*(11), e2022JE007294. https://doi.org/10.1029/2022JE007294

Carberry Mogan, S. R., Tucker, O. J., Johnson, R. E., Sreenivasan, K. R., & Kumar, S. (2020). The influence of collisions and thermal escape in Callisto's atmosphere. *Icarus*.

Carberry Mogan, S. R., Tucker, O. J., Johnson, R. E., Vorburger, A., Galli, A., Marchand, B., et al. (2021). A tenuous, collisional atmosphere on Callisto. *Icarus*, *368*, 114597. https://doi.org/10.1016/j.icarus.2021.114597

Cervantes, S., Saur, J., Duling, S., Szalay, J. R., Schlegel, S., Connerney, J. E. P., et al. (2025). MHD simulations of Europa's interaction with Jupiter's magnetosphere during the Juno flyby: Electron beams in the plasma wake. *Journal of Geophysical Research: Space Physics*, *130*(6), e2025JA033825. https://doi.org/10.1029/2025JA033825

Chavez, J. A. P., Tucker, O. J., Carberry Mogan, S. R., Johnson, R. E., & Blaszczak-Boxe, C. (2026). Impact of geometry on 1D molecular-kinetics simulations of acoustic-gravity wave propagation into the exosphere. *Icarus*, *447*, 116900. https://doi.org/10.1016/j.icarus.2025.116900

Connerney, J. E. P., Benn, M., Bjarno, J. B., Denver, T., Espley, J., Jorgensen, J. L., et al. (2017). The Juno magnetic field investigation. *Space Science Reviews*, *213*(1), 39–138.

Cosby, P. C. (1993). Electron-impact dissociation of oxygen. *The Journal of Chemical Physics*, *98*(12), 9560–9569. https://doi.org/10.1063/1.464387

de Kleer, K., Milby, Z., Schmidt, C., Camarca, M., & Brown, M. E. (2023). The optical aurorae of Europa, Ganymede, and Callisto. *The Planetary Science Journal*, *4*(2), 37. https://doi.org/10.3847/psj/acb53c

Ebert, R. W., Allegrini, F., Szalay, J. R., Pontoni, A., Saur, J., Bagenal, F., et al. (2025). Plasma and magnetic field properties in Europa's wake from Juno. *Journal of Geophysical Research: Space Physics*, *130*(5), e2024JA032520. https://doi.org/10.1029/2024ja032520

Ellis, S. P., Szalay, J. R., Livadiotis, G., Carberry Mogan, S. R., Allegrini, F., Ebert, R. W., et al. (2026). Europa is embedded in non-Maxwellian, anisotropic electron distributions. *Geophysical Research Letters*, *53*(6), e2025GL120837. https://doi.org/10.1029/2025GL120837

Evans, J. C., Carberry Mogan, S. R., Johnson, R. E., & Tucker, O. J. (2025). Thermally driven atmospheric escape: Transition from diffusion-limited to drag-off escape. *The Planetary Science Journal*, *6*(2), 39. https://doi.org/10.3847/psj/ada369

Hall, D. T., Strobel, D. F., Feldman, P. D., McGrath, M. A., & Weaver, H. A. (1995). Detection of an oxygen atmosphere on Jupiter's moon Europa. *Nature*, *373*(6516), 677–679. https://doi.org/10.1038/373677a0

Hodges, R. R., Jr., & Johnson, F. S. (1968). Lateral transport in planetary exospheres. *Journal of Geophysical Research*, *73*(23), 7307–7317. https://doi.org/10.1029/ja073i023p07307

Huebner, W. F., & Mukherjee, J. (2015). Photoionization and photodissociation rates in solar and blackbody radiation fields. *Planetary and Space Science*, *106*, 11–45. https://doi.org/10.1016/j.pss.2014.11.022

Johnson, R. E. (1990). *Energetic charged-particle interactions with atmospheres and surfaces*. Springer Science and Business Media.

Johnson, R. E., Boring, J. W., Reimann, C. T., Barton, L. A., Sieveka, E. M., Garrett, J. W., et al. (1983). Plasma ion-induced molecular ejection on the Galilean satellites: Energies of ejected molecules. *Geophysical Research Letters*, *10*(9), 892–895. https://doi.org/10.1029/gl010i009p00892

Johnson, R. E., Burger, M. H., Cassidy, T. A., Leblanc, F., Marconi, M., & Smyth, W. H. (2009). *Composition and detection of Europa's sputter-induced atmosphere* (pp. 507–527). Europa, University of Arizona Press.

Johnson, R. E., Oza, A. V., Leblanc, F., Schmidt, C., Nordheim, T. A., & Cassidy, T. A. (2019). The origin and fate of O_2 in Europa's ice: An atmospheric perspective. *Space Science Reviews*, *215*(1), 20. https://doi.org/10.1007/s11214-019-0582-1

Johnson, R. E., & Quickenden, T. I. (1997). Photolysis and radiolysis of water ice on outer solar system bodies. *Journal of Geophysical Research*, *102*(E5), 10985–10996. https://doi.org/10.1029/97je00068

Kim, T. K., Ebert, R. W., Valek, P. W., Allegrini, F., McComas, D. J., Bagenal, F., et al. (2020). Survey of ion properties in Jupiter's plasma sheet: Juno JADE-I observations. *Journal of Geophysical Research: Space Physics*, *125*(4), e2019JA027696. https://doi.org/10.1029/2019ja027696

Kollmann, P., Paranicas, C., Clark, G., Roussos, E., Lagg, A., & Krupp, N. (2016). The vertical thickness of Jupiter's Europa gas torus from charged particle measurements. *Geophysical Research Letters*, *43*(18), 9425–9433. https://doi.org/10.1002/2016gl070326

Lagg, A., Krupp, N., Woch, J., & Williams, D. J. (2003). In-situ observations of a neutral gas torus at Europa. *Geophysical Research Letters*, *30*(11). https://doi.org/10.1029/2003gl017214

Mauk, B. H., Mitchell, D. G., Krimigis, S. M., Roelof, E. C., & Paranicas, C. P. (2003). Energetic neutral atoms from a trans-Europa gas torus at Jupiter. *Nature*, *421*(6926), 920–922. https://doi.org/10.1038/nature01431

McComas, D. J., Alexander, N., Allegrini, F., Bagenal, F., Beebe, C., Clark, G., et al. (2017). The Jovian auroral distributions experiment (JADE) on the juno mission to Jupiter. *Space Science Reviews*, *213*(1–4), 547–643. https://doi.org/10.1007/s11214-013-9990-9

Nénon, Q., & André, N. (2019). Evidence of Europa neutral gas torii from energetic sulfur ion measurements. *Geophysical Research Letters*, *46*(7), 3599–3606. https://doi.org/10.1029/2019gl082200

Oza, A. V., Leblanc, F., Johnson, R. E., Schmidt, C., Leclercq, L., Cassidy, T. A., & Chaufray, J.-Y. (2019). Dusk over dawn O_2 asymmetry in Europa's near-surface atmosphere. *Planetary and Space Science*, *167*, 23–32. https://doi.org/10.1016/j.pss.2019.01.006

Plainaki, C., Milillo, A., Mura, A., Orsini, S., Massetti, S., & Cassidy, T. (2012). The role of sputtering and radiolysis in the generation of Europa exosphere. *Icarus*, *218*(2), 956–966. https://doi.org/10.1016/j.icarus.2012.01.023

Plainaki, C., Milillo, A., Mura, A., Saur, J., Orsini, S., & Massetti, S. (2013). Exospheric O_2 densities at Europa during different orbital phases. *Planetary and Space Science*, *88*, 42–52. https://doi.org/10.1016/j.pss.2013.08.011

Reimann, C. T., Boring, J. W., Johnson, R. E., Garrett, J. W., Farmer, K. R., Brown, W. L., et al. (1984). Ion-induced molecular ejection from D_2O ice. *Surface Science*, *147*(1), 227–240. https://doi.org/10.1016/0167-2584(84)90679-0

Roth, L. (2021). A stable H_2O atmosphere on Europa's trailing hemisphere from HST images. *Geophysical Research Letters*, *48*(20), e2021GL094289. https://doi.org/10.1029/2021gl094289

Roth, L., Retherford, K. D., Saur, J., Strobel, D. F., Becker, T., Bergman, S., et al. (2026). Europa's Lyman-α emissions from HST/STIS observations. *Astronomy and Astrophysics*.

Roth, L., Saur, J., Retherford, K. D., Strobel, D. F., Feldman, P. D., McGrath, M. A., et al. (2016). Europa's far ultraviolet oxygen aurora from a comprehensive set of HST observations. *Journal of Geophysical Research: Space Physics*, *121*(3), 2143–2170. https://doi.org/10.1002/2015ja022073

Rubin, M., Jia, X., Altwegg, K., Combi, M. R., Daldorff, L. K. S., Gombosi, T. I., et al. (2015). Self-consistent multifluid MHD simulations of Europa's exospheric interaction with Jupiter's magnetosphere. *Journal of Geophysical Research: Space Physics*, *120*(5), 3503–3524. https://doi.org/10.1002/2015ja021149

Sandford, S. A., & Allamandola, L. J. (1993). H_2 in interstellar and extragalactic ices: Infrared characteristics, ultraviolet production, and implications. *The Astrophysical Journal*, *409*, L65–L68. https://doi.org/10.1086/186861

Sarkango, Y., Szalay, J. R., Poppe, A. R., Nénon, Q., Liu, Z. Y., Allegrini, F., et al. (2025). Cold and hot electron populations observed by Juno-JADE in the Jovian magnetodisc. *Geophysical Research Letters*, *52*(17), e2025GL118209. https://doi.org/10.1029/2025gl118209

Scarlett, L. H., Tapley, J. K., Fursa, D. V., Zammit, M. C., Savage, J. S., & Bray, I. (2018). Electron-impact dissociation of molecular hydrogen into neutral fragments. *The European Physical Journal D*, *72*(2), 1–8. https://doi.org/10.1140/epjd/e2017-80649-8

Shematovich, V. I. (2006). Stochastic models of hot planetary and satellite coronas: Atomic oxygen in Europa's corona. *Solar System Research*, *40*(3), 175–190. https://doi.org/10.1134/s0038094606030014

Shematovich, V. I., & Johnson, R. E. (2001). Near-surface oxygen atmosphere at Europa. *Advances in Space Research*, *27*(11), 1881–1888. https://doi.org/10.1016/s0273-1177(01)00299-x

Shematovich, V. I., Johnson, R. E., Cooper, J. F., & Wong, M. C. (2005). Surface-bounded atmosphere of Europa. *Icarus*, *173*(2), 480–498. https://doi.org/10.1016/j.icarus.2004.08.013

Smith, H. T., Mitchell, D. G., Johnson, R. E., Mauk, B. H., & Smith, J. E. (2019). Europa neutral torus confirmation and characterization based on observations and modeling. *The Astrophysical Journal*, *871*(1), 69. https://doi.org/10.3847/1538-4357/aaed38

Smyth, W. H., & Marconi, M. L. (2006). Europa's atmosphere, gas tori, and magnetospheric implications. *Icarus*, *181*(2), 510–526. https://doi.org/10.1016/j.icarus.2005.10.019

Spencer, J. R., & Calvin, W. M. (2002). Condensed O_2 on europa and callisto. *The Astronomical Journal*, *124*(6), 3400–3403. https://doi.org/10.1086/344307

Spencer, J. R., Lebofsky, L. A., & Sykes, M. V. (1989). Systematic biases in radiometric diameter determinations. *Icarus*, *78*(2), 337–354. https://doi.org/10.1016/0019-1035(89)90182-6

Straub, H. C., Renault, P., Lindsay, B. G., Smith, K. A., & Stebbings, R. F. (1996). Absolute partial cross sections for electron-impact ionization of H_2, N_2, and O_2 from threshold to 1000 eV. *Physical Review A*, *54*(3), 2146.

Summers, M. E., Strobel, D. F., Yung, Y. L., Trauger, J. T., & Mills, F. (1989). The structure of Io's thermal corona and implications for atmospheric escape. Part 1 (ISSN 0004-637X). *Astrophysical Journal*, *343*, 468–480. https://doi.org/10.1086/167720

Szalay, J. R., Allegrini, F., Ebert, R. W., Bagenal, F., Bolton, S. J., Fatemi, S., et al. (2024). Oxygen production from dissociation of Europa's water-ice surface. *Nature Astronomy*, *8*(5), 567–576. https://doi.org/10.1038/s41550-024-02206-x

Szalay, J. R., Smith, H. T., Zirnstein, E. J., McComas, D. J., Begley, L. J., Bagenal, F., et al. (2022). Water-group pickup ions from Europa-genic neutrals orbiting Jupiter. *Geophysical Research Letters*, *49*(9), e2022GL098111. https://doi.org/10.1029/2022gl098111

Teolis, B. D., Plainaki, C., Cassidy, T. A., & Raut, U. (2017). Water ice radiolytic O_2, H_2, and H_2O_2 yields for any projectile species, energy, or temperature: A model for icy astrophysical bodies. *Journal of Geophysical Research: Planets*, *122*(10), 1996–2012. https://doi.org/10.1002/2017je005285

Vorburger, A., & Wurz, P. (2018). Europa's ice-related atmosphere: The sputter contribution. *Icarus*, *311*, 135–145. https://doi.org/10.1016/j.icarus.2018.03.022